修士学位論文

Developments for antiproton catching in a transportable Penning trap (可搬ペニングトラップによる反陽子の捕捉のための開発)

2025 年度

広域科学専攻　相関基礎科学系

31-246906

遠藤知

Abstract

The CPT invariance is the most fundamental symmetry in physical interactions in the Standard Model. Experimental tests of the CPT symmetry will contribute to exploring a beyond-standard model theory that can explain the matter-dominant universe.

The BASE experiment at CERN measures the g-factor and charge-to-mass ratio of protons and antiprotons, and provides the most stringent CPT test for baryons. The measurements in BASE are implemented using a Penning trap, which confines charged particles by static electromagnetic fields. However, the precision of the measurements is limited by the fluctuations in the magnetic field produced by the accelerator facility to supply antiprotons.

To overcome this limitation, a transportable Penning trap system has been developed to relocate the experiment to a calm environment, and demonstrated lossless transportation of a confined proton cloud. Since the protons used for the transportation are prepared inside the trap, the technique for injection and catching of antiprotons needs to be established.

To this end, beam position monitors to estimate the beam position were developed. The beam monitors with a grid made of copper wires were newly designed and installed in the beamline. The electronic circuits, which amplify a small charge signal from the detector to a large and long voltage pulse readable by a microcomputer, were also designed. The beam monitors were tested with antiproton and H^- ion beams, and the successful readout of the beam signal and the beam position estimation were demonstrated. The parameters of the electronics still need to be adjusted to avoid saturation and to obtain a linear response to the input signal.

The antiproton beam has the energy of 100 keV. They need to be decelerated to the energy of a few keV to capture them by an electric potential. The simulations of the deceleration of antiprotons using a thin polymer foil called the degrader foil were done. In the simulation, several options of the degrader foils with different thickness and materials were tried to observe the energy distribution of the penetrating antiprotons. As a consequence, the simulations resulted in the different energy distributions whose mean energies varied from 2 keV to 5 keV, and the distributions of the antiproton current as functions of the axial energy and the transverse energy were obtained. However, the simulation program used for this research was unable to calculate the transportation of particles under 2 keV. Therefore, a different simulation program will be required to obtain more precise energy distributions.

After the beamline was prepared, the team began to try the injection and capturing of antiprotons inside the trap. The optimal parameters for the injection were explored by storing antiprotons for a short time, releasing them, and detecting the annihilation signal of the antiprotons by a scintillator. Various parameters, including the electrodes settings to steer the beam, the timing of a high voltage pulse to block antiprotons inside the trap and the storage time, were scanned and optimized during the measurements.

Subsequently, cooling of antiprotons with trapped electrons to a few eV level was tested. The cooling is achieved by the Coulomb interaction between antiprotons and electrons and synchrotron radiation of electrons. Despite a number of attempts, we could not observe any signal of the cooled antiprotons. More detailed observations revealed that there was significant instability in trapping both antiprotons and electrons for more than a few 100 ms.

An alternative procedure for catching, which used a higher potential well, was used to catch the antiprotons. Consequently, 13 antiprotons were successfully captured inside the trap system, and the storage of antiprotons for over 30 hours, including a few hours with a lower magnetic field for the transport mode, was achieved without any particle loss. Although these antiprotons were lost due to an operational failure, the second cloud, made of 26 antiprotons, was successfully captured. These antiprotons were stored for more than 40 hours this time. The upper limit of the pressure inside the trap was estimated around 10^{-15} mbar using the storage time of the antiproton clouds.

Even though the mechanism of the instability in the normal capturing procedure is not understood yet, the project achieved an important milestone for the transportation of antiprotons.

Contents

List of Figures

1 Introduction

The CPT symmetry, which is the invariance of the physical interactions under an inversion of charge, parity, and time, is one of the cornerstones of modern physics [1]. This symmetry holds in a relativistic local quantum field theory, including the Standard Model, which is the most successful theory of fundamental physics so far. It follows that particles and their conjugate antiparticles have identical properties, including mass , charge, and magnetic moment, except for their polarity [2]. It is expected that this symmetry leads to the equal abundance of matter and antimatter in the universe, however cosmological observations imply that matter is more dominant than theoretical expectation [3], which cannot be explained by the asymmetry between matter and antimatter understood in the Standard Model [4, 5, 6].

Experimental tests of CPT symmetry give useful clues for exploring a new physics theory beyond the Standard Model. CPT test experiments can be done by comparing the properties of a particle and its corresponding antiparticle, and a number of such experiments have been attempted so far.

Such tests have been done for various particle/antiparticle pairs including electron/positron [**?**], hydrogen/antihydrogen [7] [8], and $K_0/\bar{K_0}$ [**?**] with high precision.

The BASE (Baryon Antibaryon Symmetry Experiment) [9] is one of these experiments that aims to measure the charge to mass ratio and the magnetic moment (g-factor) of protons and antiprotons with high precision and to compare them using Penning traps which can confine charged particles using static electromagnetic fields. The experiment has been running since 2014 and reported the measurement of the charge-to-mass ratio and g-factors for several times. As latest records, BASE achieved precisions of 1.5 parts-per-billion (1.5×10^{-9}) [10] for the measurement of the g-factor and 16 parts-per-trillion (1.6×10^{-11}) [11] for the charge-to-mass ratio of antiprotons, which are the highest precisions achieved so far in the baryon sector of the CPT tests.

The current limitation on the precision of measurements in BASE is the fluctuation of the magnetic field around the apparatus which is produced by the accelerator facility [12]. The Penning trap system measures the eigenfrequencies of motions of the particle inside the trap, which depend on the magnetic field. Therefore, the fluctuation of the magnetic field leads to the fluctuation of the measured value, limiting the improvement of the precision, and further improvements of the precision will necessitate the accumulation of the measurement for a duration over several years.

A solution for this limitation is transporting antiprotons to a location with less magnetic field fluctuation. BASE-STEP [12] project launched in 2021 and has developed such a transportable Penning trap system, which has an autonomous operation mode and an open structure. The autonomous operation mode enables the trap system to confine antiprotons during the transportation. This feature is achieved by equipping all of necessary devices to operate the trap within the transported unit. The open vacuum is required to hand over the transported antiprotons to the relocated experiment, unlike the trap system of BASE.

At the beginning of my Master thesis, the STEP trap system successfully demonstrated the transportation of protons across CERN lasting about 4 hours in October 2024 [13]. These protons confined in the trap during the transport were produced by releasing gas molecules from the trap surface and ionizing them using an electron beam.

In contrast, antiprotons are supplied from the two decelerators, Antiproton Decelerator (AD) and ELENA, with the energy of 100 keV, and injected into the apparatus while their position are adjusted by high voltage electrodes. The injected antiprotons are decelerated to a few keV level using a thin polymer foil (degrader foil) and subsequently captured by a constant high voltage potential wall at the downstream end of the trap and a rapidly ramped high voltage potential wall at the upstream end.

To catch the antiprotons, the beam position monitors are needed on the beamline to efficiently adjust the beam. Furthermore, the thickness of the degrader foil, which determines the energy distribution of penetrating antiprotons needs to be optimized to maximize the efficiency of the capturing.

In this thesis, the developments for these features needed for the injection and the catching of antiprotons in the BASE-STEP are described.

In section 3, the development of beam monitors which monitor the position of the antiproton beam is described.

In section 4, simulations of the deceleration of antiprotons using a thin polymer foil from 100 keV to a few keV are described. The results described in the section 3 and 4 are the author's individual contributions to the BASE-STEP project.

In section 5, attempts of the injection and the catching of antiprotons inside the trap in two manners, without cooling the antiprotons using electrons and with it, respectively, are described. The results of the section 5 were obtained by the BASE-STEP team including my own participation.

2 Matter-antimatter symmetry, BASE and BASE-STEP

2.1 CPT symmetry test

In 1928, P.A.M Dirac formulated a relativistic wave equation called the Dirac equation [14]

$$(i\gamma^{\mu}D_{\mu}-m)\psi=0 \tag{2.1}$$

where $D_{\mu}=\partial_{\mu}-ieA_{\mu}$. Also the complex conjugate of 2.1, $(i\gamma^{\mu *}D^{*}_{\mu}-m)\psi=0$, satisfies the definition of the Dirac equation, and it can be rewritten using the charge conjugation transformation $C\gamma^{0}\equiv\gamma^{2}$ and the charge conjugate of the wave function ψ_{C} as [15]

$$(i\gamma^{\mu}D^{*}_{\mu}-m)\psi_{C}=0 \tag{2.2}$$

The wave function ψ_{C} represents a particle which has the same amount of charge but with the opposite sign and the identical mass as those of the particle that ψ represents. Such a particle, called an antiparticle, is predicted to exist in reality on account of the causality [16]. As the first observation of an antiparticle, a positron was observed in a cloud chamber in 1932 [17].

The CPT symmetry is the invariance of physical interactions under the simultaneous reversals of charge (C), parity (P), and time(T). From the CPT theorem, the CPT theorem holds in any local, Lorentz invariant quantum field theory including the Standard Model (SM) in the particle physics[18]. As a consequence of the CPT symmetry, a particle and its conjugating antiparticle have the identical physical properties, such as mass, lifetime, charge, and magnetic field, but with opposite signs for the latter two [2].

Regarding the antimatter, the asymmetry of the abundance between matter and antimatter is one of the largest mysteries in the modern physics. According to the Standard Model, since particles and antiparticles have the same properties, they should have been produced as the same amounts at the beginning of the universe. The particles and antiparticles repeated pair creation and annihilation in a short duration when the temperature of the universe is much higher than the threshold energy for the pair creation. After the annihilation rate fell below the expansion rate of the universe, the antiparticles no longer encountered the particles to annihilate with, and they survived as nucleons or antinucleons [19]. Based on the cosmological theory about the evolution of the universe, the ratio of the number of baryons to that of photons can be solved as[19]

$$\eta_{B}=\frac{N_{B}}{N_{\gamma}}=\frac{N_{\bar{B}}}{N_{\gamma}}\simeq 10^{-18}. \tag{2.3}$$

On the other hand, some cosmological observations have yielded inconsistent results. One observation measured the abundances of the light species after the big bang nucleosynthesis, and the baryon-to-photon ratio η_{BBN} was calculated backwards using time evolutions of the abundances [20]. It resulted in the value $\eta_{\mathrm{BBN}}=6.07\pm 0.33\times 10^{-10}$ after corrections for the measurements. Another measurement, the WMAP7 [21], measured the cosmic microwave background (CMB) spectrum and determined η_{CMB} from the power spectrum of the temperature fluctuation of the CMB. It yielded the value $\eta_{\mathrm{CMB}}=6.160^{+0.153}_{-0.156}\times 10^{-10}$ [22].

	η
Expectation from SM	10^{-18}
BBN measurement	$6.07\pm 0.33\times 10^{-10}$
CMB measurement	$6.160^{+0.153}_{-0.156}\times 10^{-10}$

Table 2.1: The baryon to photon ratio estimated by theory and measurement.

While these two results are consistent to each other, they are significantly different from η expected from the SM. It implies that there is a significant difference in the abundance of matter and antimatter and considerable amount of matter are remained after the annihilation in the earlier universe. It is validated by the measurement of the proton and antiproton flux of primary cosmic rays[3].

Even though the Standard Model include the violation of individual C and P symmetry [4, 5, 6], and the violation of CP symmetry[23], these are insufficient to explain the asymmetry between matter and antimatter. Hence, asymmetry between matter and antimatter which is not understood yet is expected to exist.

The violation of the CPT invariance is considered as a candidate of the source of the baryon-antibaryon asymmetry. The Standard Model Extension (SME) includes the possible CPT- and Lorentz-violating effect by adding CPT-violating terms with several effective coupling constants to the hamiltonian [24, 25]. Since the CPT invariance derives the mirror properties of particles, an experimental test for the CPT-violation can be achieved by measuring such properties of particles and corresponding antiparticles and compare it. If any differences in the particle properties are found, it indicates the existence of the CPT-violating effect. Even Planck-size CPT violation effect could reproduce a significant over-abundance of matter to antimatter, thus the measurements of particle properties in high precision are motivated.

Such CPT tests have been achieved using various particles.

In 1995, a CPT test using the neutral Kaon system was reported [26]. There, the ratio of the amplitudes of neutral Kaon's decay modes and it constrained the relative difference between the masses of K_0 and $\bar{K_0}$ as $|m_{K_0} - m_{\bar{K_0}}|/m_{K_0} < 1.3 \times 10^{-18}$.

A precision measurement of the g-factor of electrons and positrons was reported in 1987 [27]. It utilized an apparatus called Penning trap, which is capable of confining charged particles using static electromagnetic fields and described in the next section. The ratio of g-factor of electrons and positrons was obtained as $g(e^-)/g(e^+) = 1 + (0.5 \pm 2.1) \times 10^{-12}$, so relative precision of 2.1×10^{-12}.

The measurements of the g-factor and charge-to-mass ratio of protons and antiprotons are achieved by the BASE collaboration, which the author is involved. Also BASE experiment uses a Penning trap system to measure the properties. In the latest reports, the charge-to-mass ratio and the g-factor were measured with relative precisions of 1.6×10^{-11} and 1.5×10^{-9} [11, 10]. These measurements achieved the most stringent CPT test among the baryon sector.

2.2 BASE

The Baryon Antibaryon Symmetry Experiment (BASE) is an experiment, which aims to test the CPT symmetry by measuring and comparing the charge-to-mass ratio and the g-factor of protons and antiprotons. To achieve measurements of the properties of protons and antiprotons with the precision of ppb (parts per billion) to ppt (parts per trillion) level, BASE utilizes a Penning trap system that can confine charged particles using static electromagnetic fields. The principle of the Penning trap and the detail of the measurements in BASE are described in this section.

2.2.1 The concept of the Penning trap

The principle of the Penning trap is the confinement of electrons or other charged particles by a combination of a static quadrupole electric field and an axial magnetic field. It was first built as a device to store electrons by H. G. Dehmelt in 1959. Dehmelt was awarded the 1989 Nobel Prize in physics for 'the development of the ion trap technique' together with Wolfgang Paul, who invented a different kind of trap called the Paul trap that confines charged particles by a dynamic electric field[28].

The 3-dimensional confinement of a positively charged particle can be achieved using a harmonic electric potential.

$$U = ax^2 + by^2 + cz^2,\ a,\, b,\, c > 0 \tag{2.4}$$

However, such a potential cannot be realized because of the Poisson equation $\Delta U = 0$, which leads to $a + b + c = 0$. Therefore, the 3-dimensional confinement of a charged particle solely by an electrostatic potential is impossible. This statement is called the Earnshaw's theorem.

Instead, in a Penning trap, a potential of $a = 2$, $b = c = -1$, which means that a particle is confined in the z-axis direction and feels a repulsive potential in the radial direction. A Penning trap provides the radial direction confinement using an axial magnetic field $\mathbf{B} = B_0 \mathbf{e}_z$. Under this magnetic field, a particle escaping in the radial direction and thus moving perpendicularly to the magnetic field is forced to move in a radial orbit described in more detail below.

2.2.2 The hyperbolic Penning trap and the dynamics of a particle

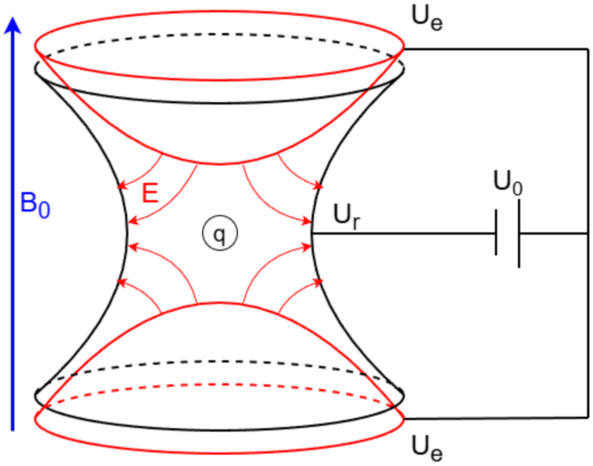

Figure 2.1: The schematic overview of a hyperbolic Penning trap. Red curves represent the boundary of the endcaps and black curves are that of the ring electrode. The red arrows are the electric field and the blue arrow is the magnetic field.

In the original idea of the Penning trap, electrodes with hyperbolic shapes are used to produce a quadrupolar electric field as schematically shown in fig. 2.1 [29]. The hyperbolic Penning trap consists of a ring electrode radially surrounding the center of the trap that has the surface

$$\left(\frac{\rho}{\rho_0}\right)^2 - \left(\frac{z}{\rho_0}\right)^2 = 0 \tag{2.5}$$

and two endcaps that are place at the top and bottom and have the shape of

$$\frac{1}{2}\left(\frac{\rho}{z_0}\right)^2 - 2\left(\frac{z}{z_0}\right)^2 = -1 \tag{2.6}$$

where ρ_0 and z_0 are the lengths that characterize the trap size [30].

When voltages $U_0 = U_e - U_r$ are applied between the endcaps and the ring electrode, a quadrupole electric potential

$$U = \frac{U_0}{2d^2}(2z^2 - x^2 - y^2), \quad d^2 = \frac{1}{2}(z_0^2 + \frac{\rho_0^2}{2}) \tag{2.7}$$

is formed inside the trap. d is called the characteristic trap size representing the size of the trap. An axial magnetic field $\mathbf{B} = (0, 0, B_0)$ is applied to confine particles radially.

When a particle with a charge q is confined in this trap, the equation of motion $m\ddot{\mathbf{r}} = -q\nabla U + q\dot{\mathbf{r}} \cdot \mathbf{B}$ can be written as

$$\ddot{x} = \omega_c \dot{y} + \frac{\omega_z^2}{2} x \tag{2.8}$$

$$\ddot{y} = -\omega_c \dot{x} + \frac{\omega_z^2}{2} y \tag{2.9}$$

$$\ddot{z} = \omega_z^2 z \tag{2.10}$$

$$\omega_z = 2\pi\nu_z = \sqrt{\frac{2qU_0}{md^2}}, \quad \omega_c = 2\pi\nu_c = \frac{qB_0}{m} \tag{2.11}$$

where ω_c is the cyclotron frequency of the confined particle in a magnetic field of B_0, and ω_z is the frequency of the axial oscillation. These equations of motion can be solved as a superposition of three oscillations

$$x(t) = \rho_+ \sin(\omega_+ t + \phi_+) + \rho_- \sin(\omega_- t + \phi_-) \tag{2.12}$$

$$y(t) = \rho_+ \cos(\omega_+ t + \phi_+) + \rho_- \cos(\omega_- t + \phi_-) \tag{2.13}$$

$$z(t) = a_z \sin(\omega_z t + \phi_z) \tag{2.14}$$

where $\rho_\pm, a_z$ are the amplitudes of each oscillation, $\omega_{\pm,z}$ are the frequencies of the oscillations, and $\phi_{\pm,z}$ are the phases. The motion of the particle can be decomposed into three independent oscillatory motions. The oscillatory motion in the axial direction with the frequency ω_z is called the axial motion, the radial motion with the frequency ω_+ is called the modified cyclotron motion, which is often abbreviated as the cyclotron motion, and the other radial motion with the frequency ω_- is called the magnetron motion. An example of the trajectory is shown in fig. 2.2.

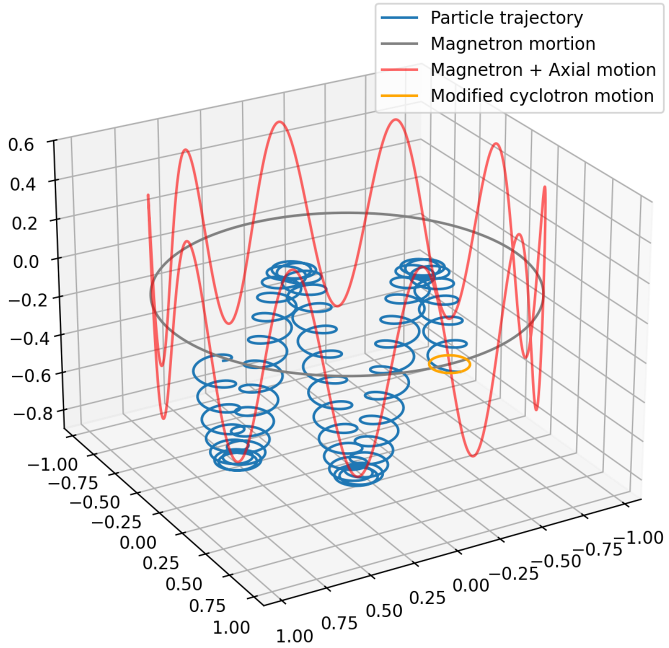

Figure 2.2: An example of a trajectory of a particle in a Penning trap (blue). The magnetron motion (gray), The axial motion combined with the magnetron motion (red), and the cyclotron motion (orange) are also drawn.

The amplitude of each oscillation can be determined independently, thus the total mechanical energy of the particle can be decomposed into that of each oscillation [30].

$$E_z = \frac{qU_0 a_z^2}{d^2} \tag{2.15}$$

$$E_\pm = \frac{m\rho_\pm}{2}\left(\omega_\pm^2 - \frac{\omega_z^2}{2}\right) \tag{2.16}$$

The eigenfrequencies $\omega_{\pm,z}$ are written as

$$\omega_z = 2\pi\nu_z = \sqrt{\frac{2qU_0}{md^2}} \tag{2.17}$$

$$\omega_\pm = 2\pi\nu_\pm = \frac{\omega_c}{2} \pm \left(\frac{\omega_c^2}{4} - \frac{\omega_z^2}{2}\right)^{\frac{1}{2}} \tag{2.18}$$

Typically, precision experiments have a strong magnetic field and a weak electric quadrupole field so that the frequencies frequencies $\omega_{\pm,z}$ differ by an order of magnitude or more from one another, and satisfy the following relations.

$$\nu_c > \nu_+ \gg \nu_z \gg \nu_- \tag{2.19}$$

$\omega_\pm$ is real only when the content of the root in eq. 2.18 is greater or equal to 0:

$$2\omega_z^2 < \omega_c^2\ . \tag{2.20}$$

The motion of a particle inside a Penning trap is stable when eq. 2.20, the stability condition, is satisfied. It can be translated as a condition limiting the electric and magnetic fields [30]

$$U_0 < \frac{1}{2} q d^2 \frac{B_0^2}{m}. \tag{2.21}$$

This condition should be noted since the STEP trap system ramps down the superconducting magnet during a transport operation.

Among these eigenfrequencies the following relation holds by their definition.

$$\nu_+ + \nu_- = \nu_c \tag{2.22}$$

$$\nu_+ \nu_- = \frac{\nu_c^2}{2} \tag{2.23}$$

Therefore, it is possible to obtain the cyclotron frequency, which derives the charge-to-mass ratio, by measuring ν_+ and ν_-. However, this method is vulnerable to errors due to trap imperfections including a tilt of the magnetic field and an axial asymmetry. Instead, the 'invariance theorem' is often used to obtain ν_c. It relates three eigenfrequencies to the cyclotron frequency.

$$\nu_c^2 = \nu_+^2 + \nu_z^2 + \nu_-^2 \tag{2.24}$$

The cyclotron frequency derived from the invariance theorem is affected by errors from trap imperfections much less than that derived using the relations above. Therefore, to achieve a high precision in the charge-to-mass ratio and g-factor measurements, the invariance theorem should be used and all of the three frequencies are required.

2.2.3 The cylindrical Penning trap

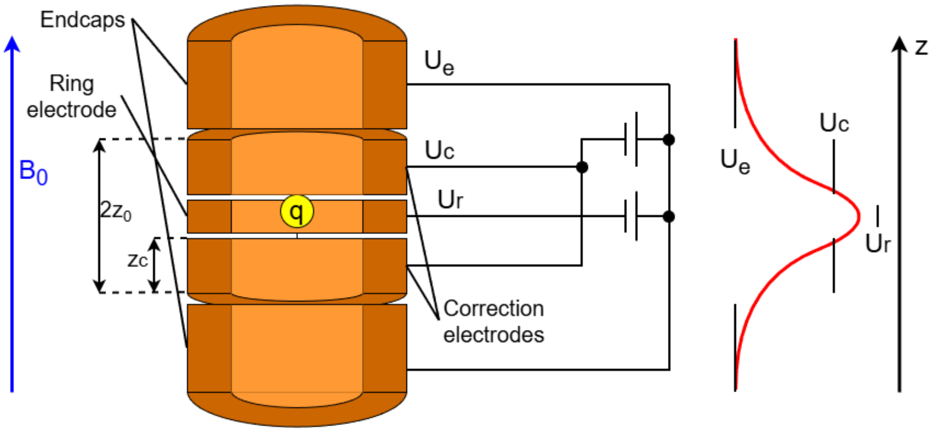

Figure 2.3: An Schematic figure of a cylindrical Penning trap. A potential well formed along the axis and the voltage of each electrode are also shown beside.

The hyperbolic Penning trap has advantage that hyperbolic electrodes can produce a perfect quadrupole potential by its design. However, it has no accessibility to the inside without making an aperture that leads to a distortion of the potential. Since BASE needs access to the inside to inject antiprotons from outside, another design is required.

The cylindrical Penning trap, which consists of multiple cylindrical electrodes (fig. 2.3), is a common solution for such applications. Since the electrodes do not have the hyperbolic shape, the potential produced by them is not completely quadrupole, therefore, it needs to be corrected by additional correction electrodes placed between the ring electrode and endcaps.

When voltage U_0 is applied between the ring electrode and endcaps, and U_r is applied between the correction electrodes and the endcaps, the produced potential can be written in a spherically expanded form [30]

$$U = \frac{1}{2} U_0 \sum_{k=0}^{\infty} C_k \left(\frac{r}{d}\right)^k P_k(\cos\theta), \ \ (k \text{ even}) \tag{2.25}$$

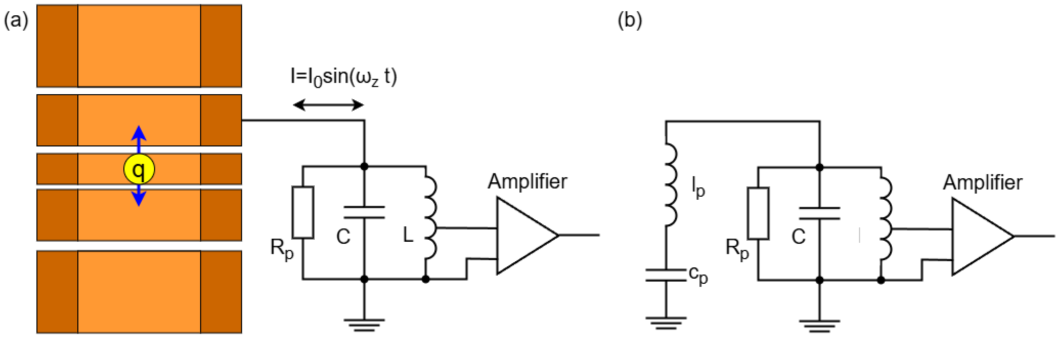

Figure 2.4: (a) The resonator circuit to amplify the image current. When the particle has high axial energy, the induced image current is amplified and observed as a peak in the frequency spectrum. (b) The equivalent circuit when the particle is cooled.

where C_k is the coefficient of each term, r is the distance from the trap center, $d = \frac{1}{2}(z_0^2 + \frac{\rho_0^2}{2})$ is the characteristic trap size, $P_k(x)$ is the Legendre polynomial, and θ is the angle from the trap axis. The summation in (2.25) is taken for even k since the trap geometry is symmetric in the axial direction. The coefficients C_k represent the influence of the correction voltage on each term. For instance, C_2 and C_4 can be expressed as below.

$$C_2 = C_2^{(0)} + D_2 \frac{U_c}{U_0} \tag{2.26}$$

$$C_4 = C_4^{(0)} + D_4 \frac{U_c}{U_0} \tag{2.27}$$

$C_k^{(0)}$ and D_k are determined by the geometry of the trap. C_4 can be canceled out by selecting a specific ratio of the ring voltage and correction voltage U_c/U_0, which is called 'tuning ratio (TR)'. Although changing the correction voltage generally changes C_2, namely the depth of the potential well, a specific geometry makes D_2 zero. When $z_c/z_0 \approx 0.8351$ and $\rho_0/z_0 \approx 1.0239$, D_2 is equal to zero. In such a geometry, which is called an 'compensated trap', the term of the order of 4 and 6 can be canceled out simultaneously without altering the harmonic potential well.

2.2.4 Measurement method

As discussed above, to measure the charge-to-mass ratio, the cyclotron frequency of the confined particle $\nu_c = qB_0/2\pi m$, and it is calculated using the invariance theorem $\nu_c^2 = \nu_+^2 + \nu_z^2 + \nu_-^2$.

The g-factor of a particle can be obtained using the cyclotron frequency ν_c and the Larmor frequency $\nu_L = g\mu_B B_0/\hbar$, which is the frequency of the spin precession in a magnetic field. They are connected with the g-factor as below.

$$\frac{g}{2} = \frac{\nu_L}{\nu_c}. \tag{2.28}$$

The axial frequency ν_z is measured using electronic detector circuit built in the trap using the image current induced by the axial motion of the particle. The other frequencies $\nu_\pm, \nu_L$ can be measured indirectly via the axial frequency detector. The methods to measure each frequency are described below in detail.

Axial frequency measurement

While a particle is confined in a Penning trap, the particle oscillates in the axial direction because of the harmonic electrostatic potential. Since a charge near a metal surface induces an image charge in the metal, a moving particle induces an image current on the electrodes.

Although the image current is on the order of fA, it can be amplified by a large impedance to a detectable level. To this end, a resonance circuit consisting of an inductance L and a capacitance C connected in parallel is connected between electrodes. When the particle is oscillating at the resonance frequency $\nu_{\text{res}} = 1/2\pi\sqrt{CL}$, the resonance circuit works as a impedance

$$R_p = 2\pi\nu_{\text{res}} Q L \tag{2.29}$$

where Q is the quality factor of the resonance circuit. The particle loses its energy and is cooled to the thermal level of the resonance circuit due to energy dissipation at the impedance. The cooling rate γ of this resistive cooling is

$$\gamma = \frac{Rq^2}{mD^2} \tag{2.30}$$

where D is the characteristic trap size. When a particle inside a trap has enough energy and it is dissipated at the resonance circuit, a FFT (Fast Fourier Transformation) spectrum converted from the transient signal at the resonator shows a peak at the particle frequency, which tells the existence of the particle in the trap.

After the particle is cooled to the thermal level, the particle works as a series LC circuit consisting of an inductance $l_p = mD^2/q^2$ and capacitance $c_p = q^2/m\omega_z^2 D^2$ [31].

$$l_p = \frac{mD^2}{q^2} \tag{2.31}$$

$$c_p = \frac{q^2}{m(2\pi\nu_z D)^2} \tag{2.32}$$

At the frequency of the particle's oscillation, the equivalent series LC circuit has zero impedance and makes a short circuit with the detector circuit. Therefore, when the particle is cooled to the thermal level, the FFT spectrum of the signal shows a so called particle dip at ν_z. ν_z can be measured by fitting a known shape of the dip to that on the spectrum.

The thermal noise observed in the FFT spectrum is the so-called Johnson-Nyquist noise[32][33] which is given as

$$E^2 d\nu = 4Rk_\mathrm{B}T d\nu \tag{2.33}$$

where E is the voltage noise density, R is the real part of the impedance of electrical components, k_B is the Boltzmann constant, and T is the temperature.

The impedance of the detector circuit combined with the equivalent circuit of the particle is

$$Z(\nu) = \left[\frac{1}{R_p} + i\left(2\pi\nu C - \frac{1}{2\pi\nu L}\right) - i\left(\frac{1}{2\pi\nu l_p - (2\pi\nu c_p)^{-1}}\right)\right]^{-1} \tag{2.34}$$

Using 2.29, 2.30, 2.31, and 2.32 the real part of $Z(\nu)$ is written as

$$R = \frac{R_p}{1 + \left(Q\frac{\nu_\mathrm{res}^2 - \nu^2}{\nu_\mathrm{res}\nu} + \frac{\gamma}{2\pi}\frac{\nu}{\nu^2 - \nu_z^2}\right)^2}. \tag{2.35}$$

The noise can be written as

$$E^2 d\nu = \frac{4k_\mathrm{B}TR_p}{1 + \left(Q\frac{\nu_\mathrm{res}^2 - \nu^2}{\nu_\mathrm{res}\nu} + \frac{\gamma}{2\pi}\frac{\nu}{\nu^2 - \nu_z^2}\right)^2} \tag{2.36}$$

The width of the dip $\Delta\nu_z$ is defined as the difference between the frequencies at which the noise level drops to $\sqrt{4k_\mathrm{B}TR_p/2}$. For $\nu_z = \nu_\mathrm{res}$, the dip width of a single particle is given as

$$\Delta\nu_z = \frac{\gamma}{2\pi} = \frac{R_p q^2}{2\pi m D^2} \tag{2.37}$$

In the case of an ensemble of antiprotons, the dip width is

$$\Delta\nu_z(N) = \frac{NR_p q^2}{2\pi m D^2}. \tag{2.38}$$

Therefore, the number of particles confined in the trap can be estimated by measuring the dip width.

Radial frequencies measurement

The frequencies of the radial motions can be measured using the sideband coupling with the axial frequency ν_z. To this end, a dynamic quadrupole potential oscillating at a drive frequency $\nu_\mathrm{rf} = \nu_\pm \mp \nu_z$ is applied.

$$\mathbf{E}(\mathbf{r}, t) = \frac{1}{D^2} V_\mathrm{rf} \cos(2\pi\nu_\mathrm{rf} t)(z\mathbf{e}_\rho + \rho\mathbf{e}_z) \tag{2.39}$$

It causes a periodic exchange of the energy called Rabi oscillation between the axial motion and the coupled radial motion, thus the amplitudes of the motions are modulated.

$$z(t) = a_z \sin(\frac{\Omega_0}{2}t)\sin(2\pi\nu_z t) \tag{2.40}$$

$$= \frac{a_z}{2}\left[\cos\left((2\pi\nu_z - \frac{\Omega_0}{2})t\right) - \cos\left((2\pi\nu_z + \frac{\Omega_0}{2})t\right)\right] \tag{2.41}$$

$$\rho_\pm(t) = \rho_\pm \cos(\frac{\Omega_0}{2}t)\sin(2\pi\nu_\pm t) \tag{2.42}$$

$$\Omega_0 = \frac{qV_{\mathrm{rf}}}{4\pi m D^2\sqrt{\nu_z\nu_\pm}} \tag{2.43}$$

where Ω_0 is the Rabi frequency, which is the frequency of the Rabi oscillation. The modulated axial oscillation can be separated into two modes at frequencies

$$\nu_l = \nu_z - \frac{\Omega}{4\pi} \tag{2.44}$$

$$\nu_r = \nu_z + \frac{\Omega}{4\pi} \tag{2.45}$$

The frequency spectrum of the modulated oscillation shows peaks at these frequencies.

In an experiment, the drive frequency ν_{rf} is slightly detuned by δ from $\nu_\pm \mp \nu_z$ as $\nu_{\mathrm{rf}} = \nu_\pm \mp \nu_z \pm \delta_\pm$. In this case, the modulated axial oscillation is

$$z(t) = a_z \sin(\frac{\Omega_\pm}{2}t)\sin(2\pi\nu_z) \tag{2.46}$$

$$\Omega_\pm = \sqrt{\Omega_0^2 + 4\pi^2\delta_\pm^2} \tag{2.47}$$

and the frequencies of components in $z(t)$ are

$$\nu_l = \nu_z - \frac{\delta_\pm}{2} + \frac{\Omega_\pm}{2\pi} \tag{2.48}$$

$$\nu_r = \nu_z - \frac{\delta_\pm}{2} - \frac{\Omega_\pm}{2\pi} \tag{2.49}$$

Although there is a detune of the drive frequency, the radial frequencies $\nu_\pm$ can be derived precisely using $\nu_{l,r}$, ν_z and ν_{rf}

$$\nu_\pm = \nu_{\mathrm{rf}} \pm (\nu_l + \nu_r - \nu_z) \tag{2.50}$$

The modified cyclotron frequency can be also measured directly in the same manner for the axial frequency. To this end, one of electrodes in a trap is radially separated so that radial motions can induce the image current between them, and they are connected via a resonant circuit tuned for one of the radial frequencies.

Larmor frequency measurement

A Larmor frequency ν_L is not related to any of the three motions of a particle inside a Penning trap, therefore it is not possible to measure ν_L directly using the detector system for the axial frequency. To measure the Larmor frequency, a magnetic field gradient is used to relate ν_L with the axial motion and detect it via the detector system.

To this end, a strong inhomogeneity of a magnetic field depending quadratically on the z-coordinate, which is called a magnetic bottle, needs to be produced at the center of the oscillation. The axial component of the magnetic field in a Penning trap can be expanded in the z-axis [30]

$$B_z(z) = B_0 - 2B_1 z + B_2 z^2 + \cdots \tag{2.51}$$

where B_0 is the offset of the magnetic field, B_1 is a coefficient of a proportional dependency on z, and B_2 is a coefficient representing the depth of a magnetic bottle. A magnetic bottle can be produced in a Penning trap by a ferromagnetic electrode with specialized geometry.

A magnetic dipole moment $\boldsymbol{\mu}$ in a magnetic field $\mathbf{B}$ feels a potential $\Phi = -\boldsymbol{\mu} \cdot \mathbf{B}$. Therefore, an antiproton which has a magnetic moment $\boldsymbol{\mu}_{\bar{p}}$ feels a harmonic potential because of the quadratic term of the magnetic moment. Combined with the electrostatic potential, the harmonic potential of a magnetic moment affects the axial motion of a particle. The axial frequency of an antiproton will split into two values which respectively represent the parallel and antiparallel spin states since they have opposite magnetic moments. This effect is called the continuous Stern-Gerlach effect. The frequency shift between the states is

$$\Delta\nu_{z,SF} = \frac{1}{2\pi^2}\frac{\mu_{\bar{p}}B_2}{m_{\bar{p}}\nu_z} \tag{2.52}$$

In BASE, a typical B_2 value is around 3×10^5 T/m^2, which results in a difference in the axial frequencies of about 231 mHz out of 549 kHz axial frequency.

2.2.5 Experimental setup of BASE

To achieve high-precision measurements of the charge-to-mass ratio and g-factor of an antiproton, BASE constructed a Penning trap system in the Antiproton Decelerator (AD) which supplies low energy antiprotons, located in CERN. The detailed features of the apparatus are described below.

Apparatus

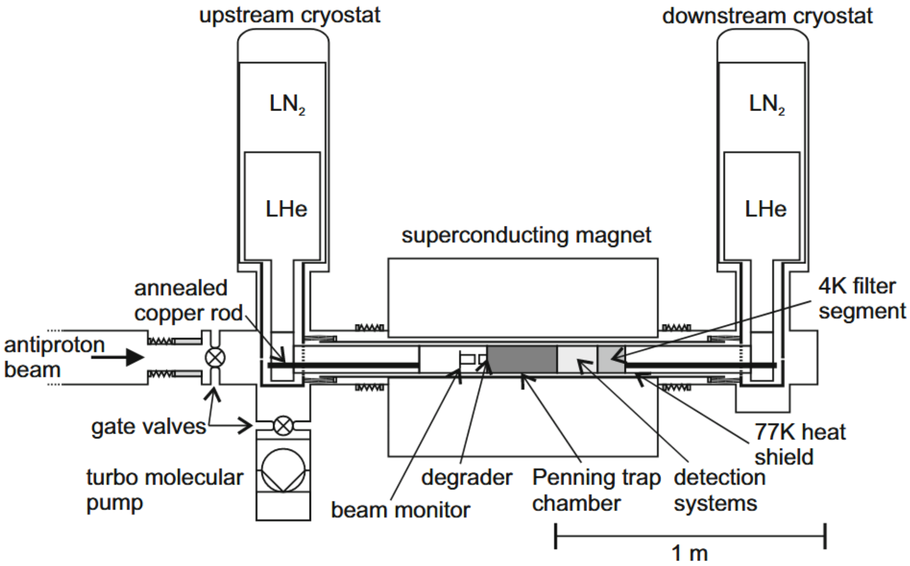

Figure 2.5: A cross-section view of the BASE apparatus. Taken from [9]

Fig. 2.5 shows a cross-section view of the BASE apparatus. The BASE apparatus has a superconducting magnet to produce a strong and homogeneous magnetic field, and two cryostats for liquid nitrogen and liquid helium to cool the trap system. The superconducting state of the magnet is maintained by separate cryoliquid reservoirs The magnet is operated to produce a magnetic field of $B_0 = 1.945\,\text{T}$. A trap chamber, which has the trap electrodes inside it, and detector circuits are fixed in a horizontal bore of the magnet by a support structure which is connected to the cryostats. The cryostats and the trap are isolated from the atmosphere by an isolation vacuum which is pumped by a turbo molecular pump placed below the vacuum chamber.

Antiprotons are injected from the beamline from AD and decelerated by a degrader foil, which is a thin ($\sim 2\,\mu$m) foil made of polymer. Injected antiprotons are caught by potential walls produced by high voltage electrodes, cooled and stored in the trap [9]. The pressure inside the trap is maintained below 10^{-19} mbar by cryopumping [34], which enables a long term storage of an antiproton cloud as long as a few years.

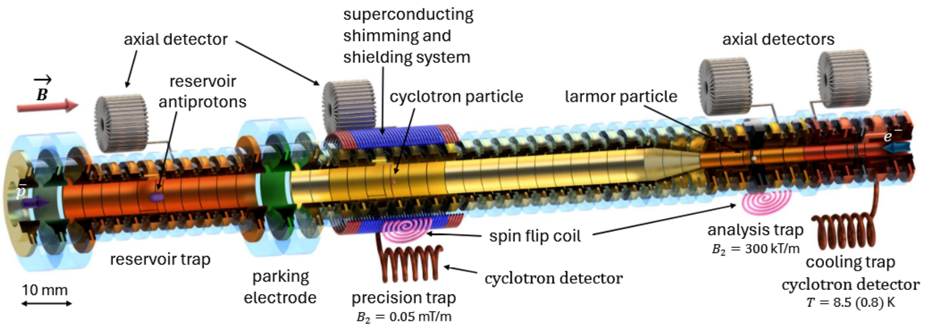

Figure 2.6: An overview of the Penning trap system of BASE taken from [34]

Fig. 2.6 shows an overview of the Penning trap system of BASE. It consists of four different traps which are dedicated to different operations in measurements. Each trap implements a different function as described below.

The reservoir trap (RT) is placed at the upstream end of the trap assembly with two high voltage electrodes at both ends of RT, and it aims to catch and store antiprotons supplied from AD. Five electrodes placed near the center of the RT are used for trap electrodes (a ring electrode, correction electrodes, and endcaps) to confine antiprotons, and other electrodes are usually used to transport antiprotons to other traps. An axial detector circuit is connected to monitor the number of antiprotons trapped inside RT. The RT typically stores $\sim$ 100 antiprotons, which is enough to continue a measurement campaign for a few years.

The precision trap (PT) is dedicated to cyclotron frequency measurements. To ensure maximum precision, it has a shimming and shielding system which is made of superconducting coils and enables us to cancel linear and quadratic magnetic inhomogeneities B_1 and B_2. An axial detector circuit and a cyclotron detector which is optimized for directly measuring and cooling the modified cyclotron frequency ν_+ are connected to a electrode.

The analysis trap (AT) aims to measure the Larmor frequency ν_L. Unlike other traps, the ring electrode of AT is made of a ferromagnetic material and has a specially designed shape to produce strong magnetic bottle by distorting the magnetic field produced by the main superconducting magnet. The AT has an axial detector connected to one of endcaps and a coil to drive the spin flip of an antiproton.

The cooling trap (CT) is placed at the downstream side to cool the modified cyclotron mode. It has a ferromagnetic ring electrode as well as the analysis trap, though it produces a weaker magnetic bottle. CT is equipped with a cyclotron detector which enables resistive cooling of the modified cyclotron mode to the level as low as 200 mK together with an axial detectors [35]. Note that the temperature 200 mK is not that of the cyclotron detector, but the amplitudes corresponding to that temperature. The modified cyclotron mode cooling suppresses fluctuations of the axial frequency dependent on the energy of the modified cyclotron mode, and enables a spin flip detection with high fidelity.

The trap electrodes are made of oxygen-free copper (OFC) coated with gold on its surface. Sapphire rings are used to isolate and align the electrodes. While the upstream side of the trap assembly is opened for injection of antiprotons, an electron gun is placed at the other end. Electrons injected from the electron gun are used to cool antiprotons injected from the beamline which have high radial motion energy.

Antiproton production

Fig. 2.7 shows the beamlines of the accelerator complex used for produce and provide antiprotons. The antiprotons used in BASE are provided by the CERN Antimatter Factory (AMF), which is the only facility in the world so far that is capable of providing low-energy antiprotons. In the AMF, antiprotons are produced by the collisions of protons and a target material[36] and decelerated by two decelerator rings, the Antiproton Decelerator (AD) and the Extra Low Energy Antiproton ring (ELENA) to the energy of 100 keV, approximately.

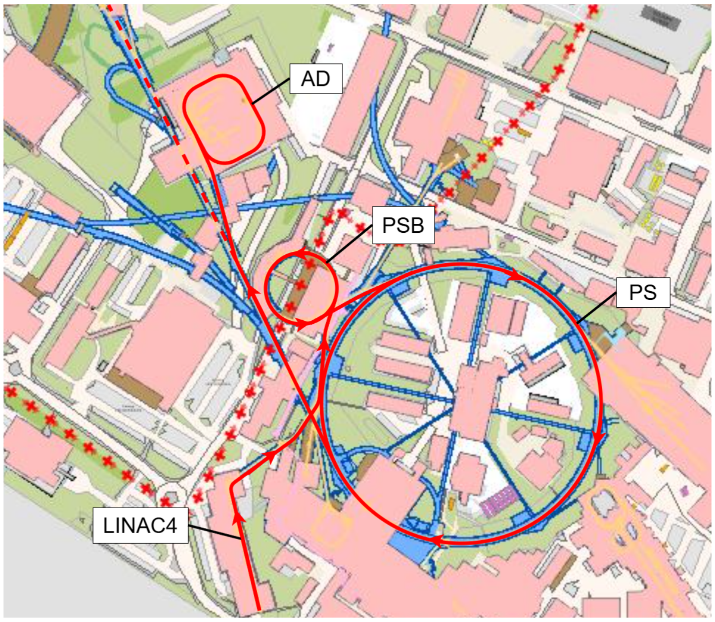

Figure 2.7: The beamlines of the accelerator complex used to supply protons to AD.

At first, the linear accelerator (LINAC4) accelerates negative hydrogen ions (H^-) to 160 MeV energy and the H^- ions are transmitted to the next circular accelerator, the Proton Synchrotron Booster (PSB). As the H^- ions are ejected from the LINAC4 and injected into the PSB, two electrons of the ions are removed, and remaining protons are divided and accelerated by four superimposed rings composing the PSB up to the energy of 2 GeV. The 2 GeV protons are injected into the larger accelerator, the Proton Synchrotron (PS) to e accelerated to the energy of 26 GeV, which is high enough to produce antiprotons by the pair-creation reactions.

The protons transmitted from the PS to the AD are injected into the target material made of a thin iridium rod with 3 mm × 55 mm diameter and length embedded in graphite and enclosed in a sealed titanium container[36]. The emerging antiprotons are focused into the injection line by a magnetic horn used as a collector lens.

The injected antiprotons travel in about 190 m long beamline of the AD [37]. A bunch of antiprotons, which has the momentum of 3.7 GeV/c, is first cooled using the stochastic cooling technique to suppress the spread of the bunch in phase space.

In the stochastic cooling phase, a fraction of the beam is sampled to obtain the average transverse position or longitudinal momentum of the sample using a non-destructive measurement device called a pick-up [38, 39]. The signal from the pick-up is amplified and sent to a kicker, which is placed downstream of the pick-up and applies a correction voltage to counteract the displacement of the sample according to the signal. Although the entire bunch of the particles cannot be cooled within a single cycle since the kicker only counteracts a fraction of the beam, the sample is cooled after many cycles while the rest of the bunch is not affected averaging the cycles.

After the first stochastic cooling phase, the bunch of the antiprotons is decelerated by the deceleration rf system with 3.5 kV peak voltage to a intermediate energy level of 2 GeV/c.

Another stochastic cooling process takes place again at 2 GeV/c, afterwards the antiprotons are further cooled to 300 MeV/c.

Here another cooling technique called electron cooling takes place. In this step, an electron beam with well gathered momenta is injected into the antiproton beamline and merged with the antiproton bunch [40, 37]. The merged beam reaches the thermoequilibrium by the Coulomb interaction, hence the kinetic energy of the antiprotons is transferred to the electrons. The electrons are extracted from the beam and dumped.

The cooled antiprotons are decelerated to 100 MeV/c (5.3 MeV kinetic energy) and electron cooled to be handed over to the ELENA.

The ELENA is a hexagonal decelerator ring with the circumference of about 30 m. The antiprotons injected into ELENA undergo the deceleration from 100 MeV/c to 13.7 MeV/c (100 keV kinetic energy), while electron cooling phases take place at momenta 35 MeV/c and 13.7 MeV/c [37]. Subsequently the antiprotons are ejected from ELENA and distributed to the experiments by electrostatic beamlines at 100 keV energy.

The deceleration processes by the AD and ELENA take about 100 s and 20 s approximately, and the antiprotons are usually supplied in 2 minute cycles.

Measurement sequence

At first, the antiprotons injected from ELENA traverse the degrader foil placed at the entry of the trap system and are decelerated to the energy of a few keV. A fraction of the antiprotons with an energy below a certain level is reflected by a potential wall formed by the high voltage (HV) electrode located next to the downstream end of the RT. Afterwards, the other HV electrode on the upstream end is quickly ramped to confine the particles inside the RT. The confined particles with energy of a few keV are cooled into a range of 4 K to 200 K by electrons stored in the RT in advance [41].

For the charge-to-mass ratio measurement, an antiproton and a H^- ion, as a proxy of a proton, are simultaneously confined and measured in turns. This method enables us to use a common electric potential and avoid a systematic error due to inverting the voltage. Since a H^- ion contains two electrons, it is slightly heavier than a proton[11]

$$R_{H^-,p} = \frac{m_{H^-}}{m_p} = 1.00108921875380(3). \tag{2.53}$$

The ratio of masses of the two particles is calculated theoretically and has an uncertainty of 3×10^{-14}.

From the composite cloud of the antiprotons and H^- ions stored in the RT, an individual antiproton and H^- ion are extracted and one of them is transported to the trap position of the PT while the other particle is stored at the parking position next to the upstream end of the PT. After a measurement of the first particle in the PT is completed, it is transported to another parking position at the downstream end of the PT, and the other particle is transported to the PT to be measured.

Repeating these procedures, data of over 24,000 frequency measurements were collected in four measurement campaigns between December 2017 and May 2019 [11]. From this dataset, the ratio of charge-to-mass ratios of a proton and antiproton was obtained as

$$\frac{(q/m)_p}{(q/m)_{\bar{p}}} = -1.000000000003(16). \tag{2.54}$$

This result support the CPT symmetry, having 16 ppt uncertainty and is currently the most precise measurement of this quantity.

During a measurement of the g-factor of the antiproton, two antiprotons are used simultaneously. One of antiprotons is first prepared in the PT, the magnetron mode is cooled by sideband coupling to the axial mode, and the cyclotron mode by direct resistive cooling using the cyclotron detector. The cooling of the modified cyclotron mode is especially important to establish a high-fidelity detection of a spin flip [42, 10, 35]. The frequency shift caused by a spin flip $\Delta\nu_{\mathrm{SF}}$ is only ppm level compared to the axial frequency. The cyclotron energy E_+ needs to meet $E_+/k_{\mathrm{B}} < E_{\mathrm{th}}/k_{\mathrm{B}} = 0.2\,\mathrm{K}$ to suppress axial frequency fluctuations dependent on E_+ sufficiently compared to the frequency shift of a spin flip [10]. The cooled antiproton is transported to the AT, where the strong magnetic bottle $B(z) = B_0 + B_2$ at $B_0 = 1.23\,\mathrm{T}$ and $B_2 = 272(12)\,\mathrm{kT/m^2}$, to check if E_+ is low enough by measuring the axial frequency, which depends on E_+ under the strong magnetic bottle. Such cooling processes are repeated until the cyclotron energy is cooled below the threshold.

The cooled antiproton (Larmor particle) is transported to the AT after the cooling, and another antiproton (cyclotron particle) is loaded into the PT. The first step of the measurement is to identify the spin state of the cold antiproton. To this end, an axial frequency measurements and spin flip drives are implemented in turn until a frequency shift due to a spin flip is observed:

$$\Delta = \nu_{z,k,j+1} - \nu_{z.k,j} > 190\,\mathrm{mHz} \tag{2.55}$$

where j is the index of the axial frequency measurements and k is the index of the entire measurement cycles. Subsequently, the cyclotron frequency of the cyclotron particle in the PT is measured three times $j \in \{1, 2, 3\}$. Afterwards, the cyclotron frequency is transported to the parking electrode placed on the upstream side, and the Larmor particle is carried to the PT. The Larmor particle is driven by a

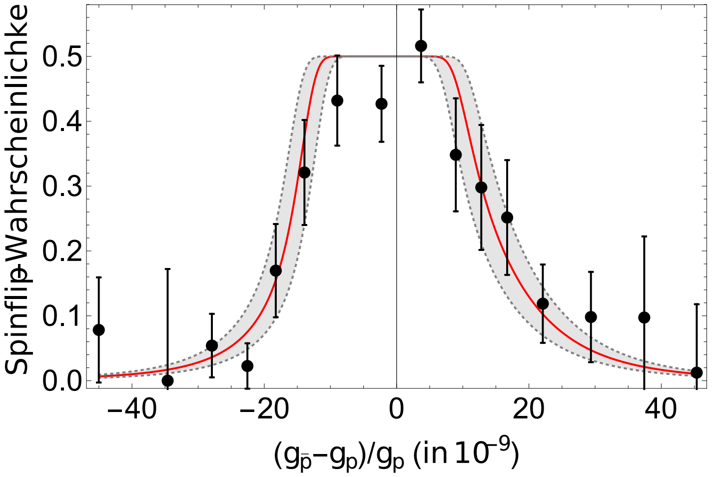

Figure 2.8: The g-factor resonance of the antiproton as a function of the irradiated frequency ratio ν_{rf}/ν_c from [10]. The red line is the result of a direct likelihood estimation of $g_{\bar{p}}$ and Ω_R. The gray area indicates the 68% error band.

RF field at a drive frequency $\nu_{\mathrm{rf},k}$ and spin transition Rabi frequency Ω_R for a certain duration using the spin flip coil placed beside the trap. The Larmor particle and the cyclotron particle are moved back to the AT and PT, respectively, and additional three cyclotron measurements in the PT and the spin flip determination in the AT are implemented.

The cycle of measurements is repeated for different drive frequencies $\nu_{\mathrm{rf},k}$ and the g-factor resonance $\Gamma_k = \nu_{\mathrm{rf},k}/\nu_{c,k}$, which is the probability of spin flip, can be obtained by normalizing the drive frequency by the averaged cyclotron frequency as shown in fig. 2.8.

In the latest report [10], the g-factor of the antiproton was measured as

$$\frac{g_{\bar{p}}}{2} = 2.792847350(9), \tag{2.56}$$

which is in agreement with CPT invariance, with 1.5 parts-per-billion uncertainty.

2.3 Influence of the magnetic field fluctuation

Since the frequencies measured in a Penning trap are dependent on the magnetic field, it is required to be stable during the measurement. Though a superconducting magnet operated in persistent-mode yields high stability of the produced magnetic field, the best Penning trap experiments have reached a frequency stability of up to 10^{-11} in subsequent measurements. While an offline Penning trap measurement which is affected by the intrinsic stability of the superconducting magnet, BASE which is operated inside the Antiproton Decelerator facility needs to consider the fluctuations of the external magnetic field produced by the decelerator.

The AD/ELENA complex ramps its magnets during the deceleration process, so it produces periodic shifts in the magnetic field. The periodic change of the magnetic field inside AD is up to about $3\,\mu$T as shown in fig. 2.9(a) and it would cause a systematic relative shift of 10^{-6} level in a frequency measurement if it exists at the trap center.

Even though the BASE Penning trap system has the shielding coil system around the PT, which can suppress the fluctuations of the external magnetic field by a factor of up to 225(15), frequency measurements in the AD are limited by the magnetic fluctuations during AD operations. For instance, the measurement of the cyclotron frequency ratio of the antiproton and H^- ion has a relative uncertainty of $\Delta R/R = 2000$ ppt during an AD operation, while $\Delta R/R = 300$ ppt under "AD-off" conditions. This fact results in that achieving a relative precision of 3 ppt requires 10,000 measurements while the AD is off, corresponding to a measurement time of ~ 30 days, while the same precision needs a measurement time of 44 months while the AD is running. Considering that systematic studies which involve evaluations of multiple systematic errors are needed in addition to the frequency measurements, the total time required for complete measurements is several times longer than that for frequency measurements, which means that at least a few months are required even under the best conditions.

Usually, the AD/ELENA complex is switched off during the Year End Technical Stop (YETS), which typically takes place from December to the beginning of next April. During YETS, BASE typically has two weeks of 12h calm facility after the end of the antiproton run while the other experiments are still active, four weeks of 24/7 calm facility during Christmas and at the beginning of the year, and six weeks of 12h calm facility when ELENA is being commissioned from the middle of February to the beginning of April. The duration of calm facility is not sufficient to achieve a precision of a few ppt which is 10-fold higher than any precision achieved so far.

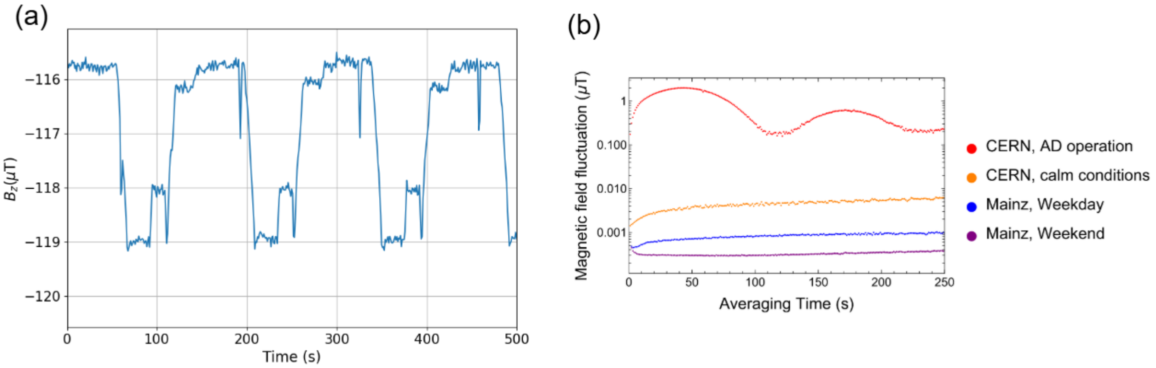

Figure 2.9: (a) Transient magnetic field measured in BASE-STEP experimental area in AD during the AD facility is working. (b) The allan deviation 2.57 measured in the AD and the university of Mainz.

Fig. 2.9(b) shows the influence of the AD facility on the magnetic field fluctuation. Here, mean magnetic fields $\mu_{t_i,t_i+\tau}(B)$ of certain durations from t_i to $t_i+\tau$ were calculated from a data set of a measurement lasting 24 hours. Then Allan deviation using differences between consecutive time bins was calculated as a function of the averaging time τ.

$$\sigma_B(\tau) = \sqrt{\frac{1}{N}\sum_{i=1}^{N-1}(\mu_{t_i+\tau,t_i+2\tau}(B) - \mu_{t_i,t_i+\tau}(B))^2} \tag{2.57}$$

where $t_{i+1} - t_i = \tau$. These values were measured and calculated at some experimental conditions, in the AD facility of CERN while the AD is on (red) and off (orange), and in the experimental area of BASE in the University of Mainz, on a weekday (blue) and a weekend (purple).

While the "AD on" condition shows periodic changes due to the periodic correlation, it is in the range of 0.1 to 1 μT. The "AD off" condition yielded about 40 times lower deviation at $\tau = 120\,\mathrm{s}$ compared to the AD on condition, though there were still contributions by other experiments' activities in the AD hall. The deviation in the Mainz experimental zone is lower than that in the AD. While there is a difference of a factor of 4 to 5 between the weekday and weekend, it was a few times 0.1 nT in the weekend condition.

Therefore, performing the measurements in an offline laboratory reduces the magnetic-field fluctuations by a factor of several hundred compared to the AD during operation, which significantly improves the measurement precision. A transportable antiproton trap that allows the experiment to be moved from the AD to an offline laboratory is essential for achieving higher precision.

2.4 BASE-STEP

BASE-STEP (Symmetry Test in Experiments with Portable Antiprotons) aims to develop a transportable Penning trap system which can transmit antiprotons from AD to an offline laboratory located at CERN or other institutions. The trap system will be loaded and carried on a truck while the system will be working to confine antiprotons.

To this end, the BASE-STEP Penning trap system was designed to be transportable, autonomous and open for injection, storing, carrying and ejection of antiprotons.

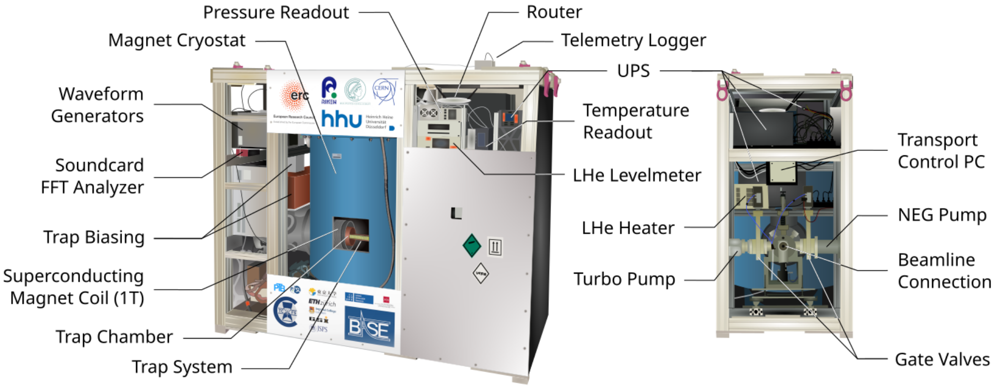

Figure 2.10: An overview of the transportable frame of BASE-STEP trap system. The antiprotons are injected from the right side of the left picture.

2.4.1 Apparatus

Fig. 2.10 shows an overview of the transport frame with the Penning trap system. All of the components needed to operate the trap are installed inside a frame sized 194 cm × 85 cm × 160 cm. In addition to the trap biasing, waveform generators, and a FFT analyzer, which are essential for the operation of the trap and the measurements, uninterrupted power supplies (UPS), a router, and a control PC are placed for the transport operation. A liquid helium levelmeter and pressure readouts are also included in the frame to monitor the status of the cryostat and the vacuum chamber.

The magnetic field for particle confinement is provided by the superconducting magnet with a single cryostat for liquid helium. The magnet is operated at a magnetic field level up to 1 T, depending on the kind of the operation such as catching and transporting.

The trap system inside the bore of the magnet consists of two traps which are respectively used for catching and storing antiprotons.

Trap system

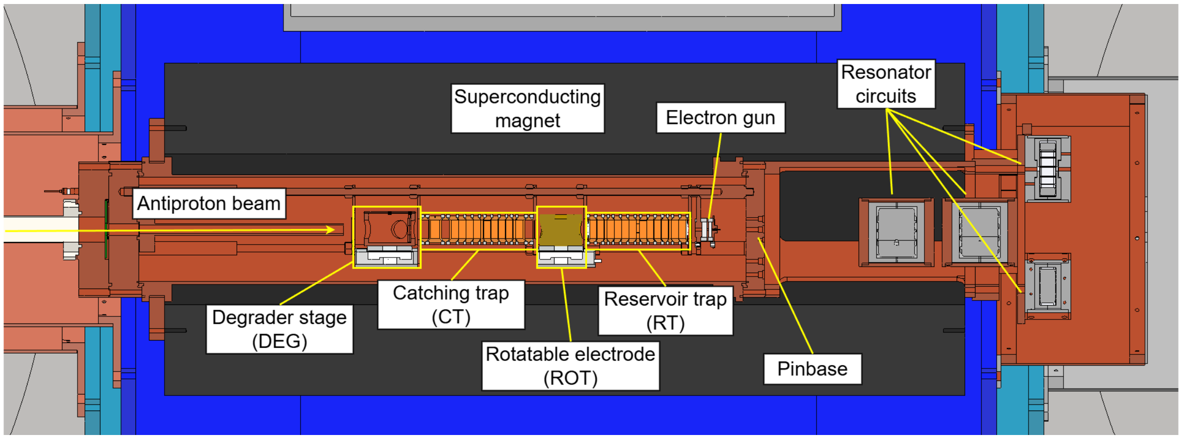

Figure 2.11: A cross-sectional view of the trap system with the name of each component. Antiprotons are injected from the left side.

A schematic cross-sectional view of the trap system is shown in fig. 2.11. The trap electrodes are placed inside the hermetically sealed trap chamber, which is fixed on the superconducting magnet. The resonator circuits for the measurements are placed outside the trap chamber, while they are electrically connected to the electrodes via the feedthrough flange called pinbase, which is placed on the downstream end of the trap chamber.

The trap electrodes consist of two sets of the trap electrodes and two rotatable parts.

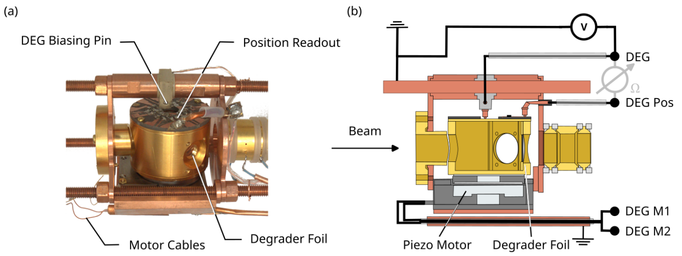

Figure 2.12: (a) A photo of the rotatable degrader stage (DEG). (b) A schematic connection diagram of the DEG.

The rotatable degrader stage (DEG) is placed at the upstream end of the trap stack. It is equipped with a thin foil made of polymer, which is called a degrader foil. A degrader foil is used to decelerate antiprotons traversing through the foil by scattering of antiprotons by electrons and atoms in the degrader foil material, and resulted energy loss. Since antiprotons supplied from ELENA have an energy of 100 keV, which is too high to capture them with an electric potential of a few kV, a degrader foil is essential for capturing antiprotons inside the Penning trap.

Although the capturing process requires a degrader foil, in the ejection process, when the stored antiprotons are transmitted to the relocated measurement apparatus with an energy of a few keV, the degrader foil will completely block the antiproton beam. Therefore, the degrader foil is required to switch its position and an aperture is placed on axis to transmit the slow antiprotons outside.

The rotatable degrader foil stage driven by a piezoelectric motor fulfills this requirement. Its cylinder-shaped rotor has two pairs of windows so that a beam can pass through them, and a degrader foil is fixed on one of the windows. The position of the rotor is monitored by a dedicated monitoring circuit placed on the top of the rotor. Two copper plates are attached on the top of the rotor, and one of them is connected to the readout pin going outside via a resistor while the other is shorted the pin. A fixed grounded probe contacts one of the plates depending on the position of the rotor. The readout probe is connected to the outside of the apparatus, and the resistivity is read there.

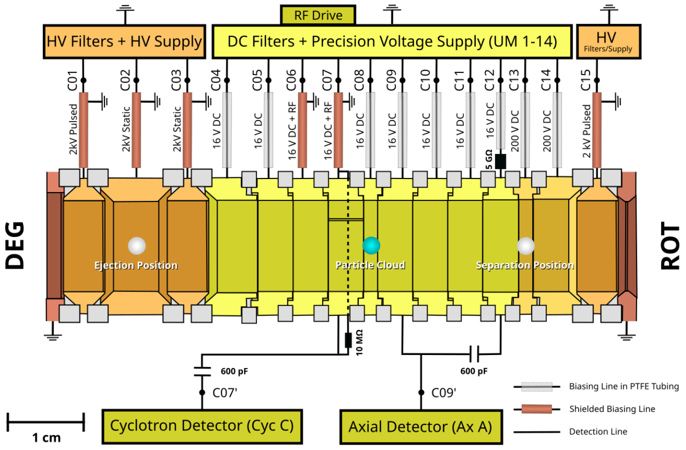

Figure 2.13: A schematic cross-sectional view of the catching trap. The connection of each electrode is also displayed.

The catching trap (CT) is designed to capture antiprotons. It consists of 15 electrodes (from the upstream, C01 to C15) made of gold coated OFC insulated by sapphire rings as the BASE trap system. C01, C03 and C15 are the high voltage electrodes which can be biased up to ±2 kV. C13 and C14 are capable of being biased up to 200 V. The electrodes are connected to the pinbase while the wires are covered by PTFE tubes to avoid a short circuit and mechanically support the wires. Some wires that conduct high voltages or RF signals are shielded by grounded copper tubes to avoid affecting the stability of the electrostatic potential.

The electrodes C06 to C10 compose a 5-electrodes Penning trap, which is equipped with a cyclotron detector (Cyc C, C07) and an axial detector (Ax A, C09).

In the capturing process, While C15 is biased at −2 kV constantly, C01 is ramped from 0 to −2 kV in a short time of about 200 ns by a high voltage switch connected to the electrode and placed outside the STEP apparatus.

The captured antiprotons are cooled to a few eV level by an electron cloud confined in advance, afterwards they are accumulated around C08 by a potential produced by C06 to C10.

The cloud of captured antiprotons can be separated and merged by manipulating the potential [43]. Using this technique, a single antiproton can be extracted from the cloud and ejected from the apparatus to a receiver apparatus, which minimizes risk of losing the entire antiproton cloud. The separation is executed by forming a potential well, which is flat around the three electrodes (C07 to C09) and ramping the ring electrode C08 to form double potential wells separated by a potential wall.

A fraction of antiproton to be ejected is adiabatically transported to C02 where C01 to C03 form a potential well of about 10 V. The three electrodes are ramped up to a high voltage range of 3 kV, keeping the shape of the potential well. The antiproton(s) can be ejected with an energy of about 3 keV by pulsing C01 to 0 V.

The other fraction can be transmitted to the neighboring trap, the reservoir trap. To this end, a process similar to that for the ejection is executed using electrodes from C13 to C15, but with the lower voltage of 200 V.

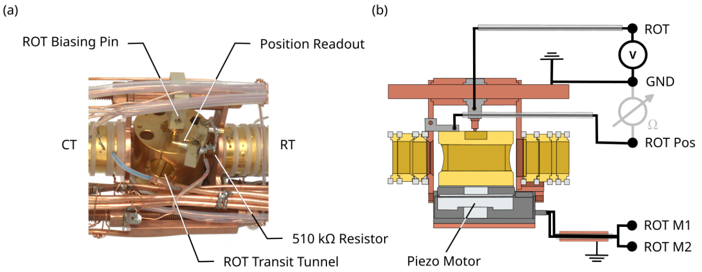

Figure 2.14: (a) A photo of the ROT electrode. (b) A cross-sectional view of the ROT section and a connection diagram

The rotatable electrode stage (ROT) is placed between the catching trap and the reservoir trap (RT), which aims to store antiprotons for a long period. It has a similar design to that of the degrader stage. It consists of a piezoelectric motor, a cylinder-shaped rotor with a tunnel, and a circuit for the position readout function.

The purpose of the ROT is to preserve the antiprotons in the RT during the ejection process. Before the ejection process, a small fraction of the antiprotons is prepared at the CT and the rest is in the RT. When the antiprotons in CT are ejected from the trap, the DEG is rotated to open the path and the trap is exposed to molecular flows coming from outside with a higher pressure. The ROT is turned to block the molecular flow so that the antiproton loss due to annihilation of antiprotons with gas molecules is minimized.

The reservoir trap (RT) is dedicated to the storage of antiprotons. It consists of 15 electrodes (R01 to R15) as well as the CT. R01 to R04 and R13 can be biased up to 200 V while the other electrodes are biased up to 16 V.

The electrodes R01 to R03 are used for shuttling antiprotons between the CT and RT. Capturing antiprotons from CT can be done by pulsing R01 with a constant potential wall at R03.

Antiprotons transmitted from the CT are transported from R02 to R08, the center of the 5-electrodes Penning trap identical to that in the CT. A cyclotron detector (Cyc B) and an axial detector (Ax E) are connected to R07, R09, and C12 respectively.

The separation and merging can be done also in the RT, enabling the merging of antiproton clouds from multiple shots and the storage of up to a few thousands antiprotons.

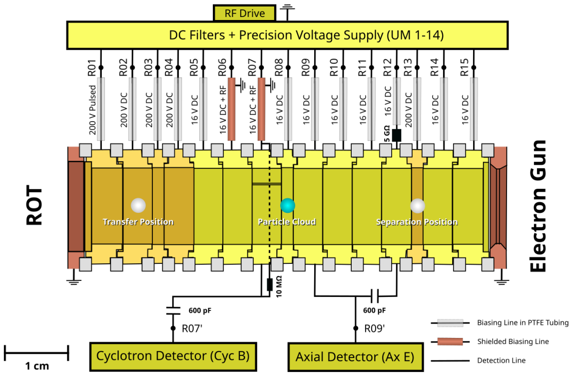

Figure 2.15: A schematic cross-sectional view of the reservoir trap.

The cryogenic and vacuum system

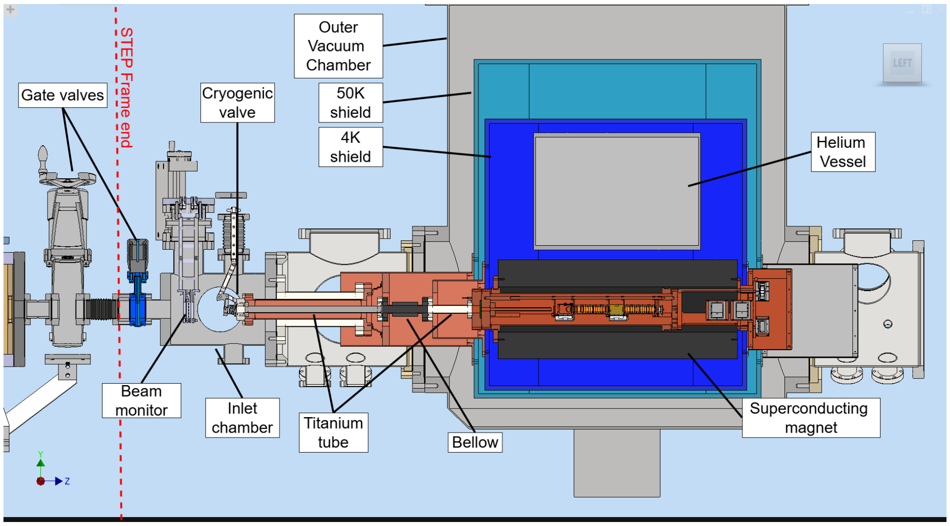

Figure 2.16: A cross section view of the trap system of the STEP apparatus. Each component of cryogenic and vacuum system is labeled. The approximate position of the end of the transport frame is indicated by a red broken line.

Fig 2.16 shows the cross-sectional view of the trap system including the cryostat and vacuum chambers.

The trap chamber is fixed to the superconducting magnet so that the misalignment of the magnetic field is minimized. The magnet consists of one main solenoid of 500 mm long and four shim coils, which are made of Niobium Titanium (NbTi) wires and integrated in the circuit of the main solenoid. It achieves magnetic inhomogeneity of $|B_1| < 0.85\,\mathrm{mT/m}$ and $|B_2| < 0.64\,\mathrm{T/m^2}$ between $z = -75\,\mathrm{mm}$ and $z = 75\,\mathrm{mm}$, where $z = 0$ is the center of the magnet. The magnet is fixed and thermally connected to the helium vessel. The helium tank has five tubes connected to the outside named H1 to H5. Each vessel is used for the following purposes:

1. H1 Helium exhaust line: It connects the tank to the outside via two heat exchangers on two heat shields.

2. H2 Helium relief/siphon line: Helium can be exhausted without the heat exchanger. Helium is refilled to the tank using this line.

3. H3 Helium safety valve: It is equipped with a safety valve opening at 1.0 bar.

4. H4 Helium rupture disc: It is equipped with a rupture disc opening at 1.5 bar.

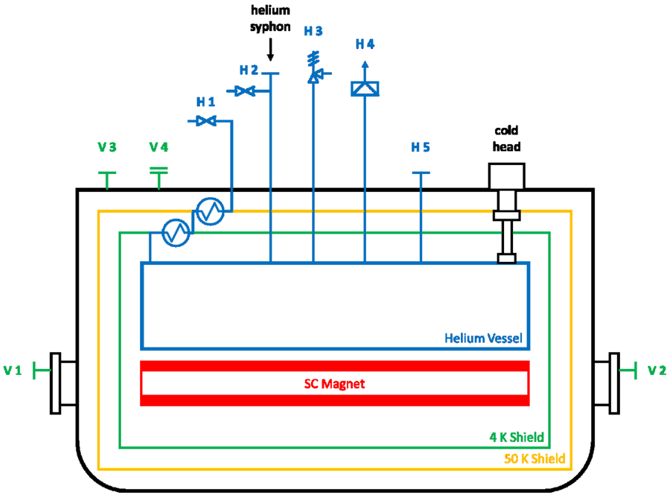

Figure 2.17: A schematic of the cryostat with indicating the connection of the vessels and the coldhead.

5. H5 Helium instrumentation: The probe of the helium tank levelmeter is connected.

The helium tank is also connected to the cold head of the two-stage pulse tube cryocooler to reliquify helium from a gas source. The cooling of the system is supplied by this cryocooler at a stationary operation in the AD, while it is done by liquid helium tank during a transport operation.

The cryostat contains two heat shields to decrease the heat load from the outside, which are at 4 K and 50 K, respectively. The components described above are put in the outer vacuum chamber (OVC), and the volume inside the OVC, including that inside the 50K and 4K heatshields, are pumped out so that the cryogenic components are better insulated from the room temperature environment.

The aperture of the trap chamber is extended by tubes made of titanium and a bellow placed between them to absorb the mechanical stress. The end of the tube reaches in a vacuum chamber called the inlet chamber. A beam monitor to detect the position of the beam and a cryogenic valve are attached in this chamber. The inlet chamber is evacuated by a NEG pump and two turbo molecular pumps (TMPs) connected in series and backed by two scroll pumps. The pressure reaches 10^{-9} mbar after a few times of activations of the NEG pump. The vacuum inside the trap chamber is expected to be 10^{-16} mbar due to cryopumping, during which the residual gas is frozen on the cold surface of the trap chamber. The difference of the pressure between the inlet chamber and the trap chamber results in a flow of gas molecules. Even though the long tube structure between the inlet chamber and the trap suppresses the amount of gas reaching the trap to some extent, the molecules blown into the trap accumulate on the cold surface and the effect of the cryopumping is decreased. To avoid the early accumulation of the molecules, the cryovalve closes the entrance of the tube section and blocks the gas flow when a beam is not injected.

2.4.2 The STEP Beamline

Antiproton bunches ejected from ELENA are transmitted via beamlines spreading to the experiments in the AD. The beamline used to supply the bunches to BASE-STEP is shared with two experiments located behind STEP.

A bunch supplied to STEP is kicked to a small angle of about 8.3 degrees by a fast deflector capable of applying a high voltage pulse. The deflected bunch is further deflected by a large deflector chamber that bends the trajectory into the vertical direction while other bunches going to other experiments go straight.

Beyond the deflector, two beam manipulating devices called ZQNA chamber are placed. A ZQNA chamber consists of two sets of quadrupole electrodes and two pairs of dipole electrodes. The quadrupole electrodes can focus the beam in one direction, though the beam is defocused in the other direction. The dipole electrodes can shift the beam horizontally or vertically by applying positive and negative

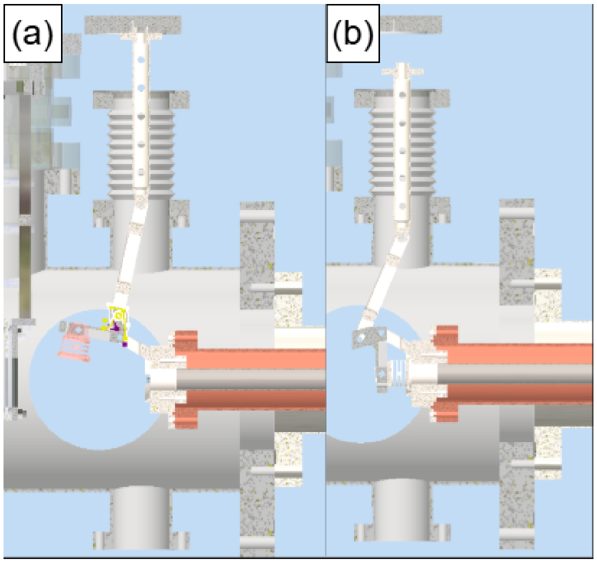

Figure 2.18: The cryovalve when it is open (a) and closed (b). The valve is manipulated by pulling or pushing the rod connected to it using a linear shift bellow.

voltages on each side. Each electrode can be biased up to ±1500 V. The voltages are controlled by a system provided by CERN from the control room of the BASE-STEP. A beam monitor is installed between the ZQNA chambers.

The beamline from ELENA is separated from that in the BASE-STEP experimental zone by a gate valge called the handover valve. The handover valve is controlled by CERN's control system and can be opened only when the pressure of the beamline on the STEP side is below 5×10^{-9} mbar and the experimental area is locked.

In the BASE-STEP experimental area, a vacuum chamber to install a beam monitor described in the chapter 3 is connected to the handover valve via a reducer flange. In addition to the beam monitor, a scroll pump backed turbo molecular pump and two vacuum gauges, which input the status of the vacuum to the control system of the handover valve, are installed on the chamber. To bend the beam into the horizontal direction, another deflector chamber is installed above the beam monitor chamber. It has a pair of bended electrodes to produce a centripetal electric field. Typically, a voltage of about 10000 V is applied between the electrodes to deflect the beam by 90 degrees. It is connected to two TMPs, behind which the vacuum vessels are merged and connected to the backing TMP and scroll pump. Beyond the second beam monitor installed at the downstream end of the deflector chamber, a ZQNA chamber, which has the same design as that in the beamline beneath the floor, is installed. The electrodes of the deflector chamber and the ZQNA chamber are connected to a high voltage power supply placed in the experimental area and controlled from the BASE-STEP control room by our control system. The gate valves at the end of the STEP trap and the beam lines are connected with a bellow and T-piece. The branch of the T-piece is connected to a TMP backed by a scroll pump, and the section was evacuated before the gate valves were opened. When the trap system does not need to be connected to the beamline or is going to be transported, the gate valves are closed and the intermediate section is removed.

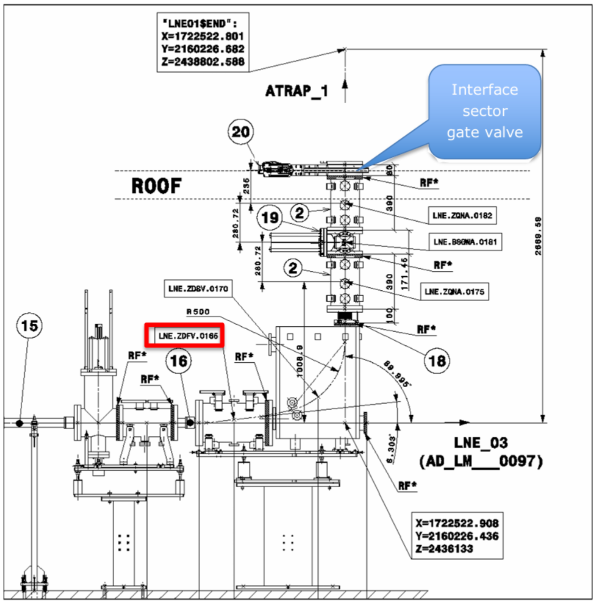

Figure 2.19: The drawing showing the beamline from ELENA under the experimental area of STEP.

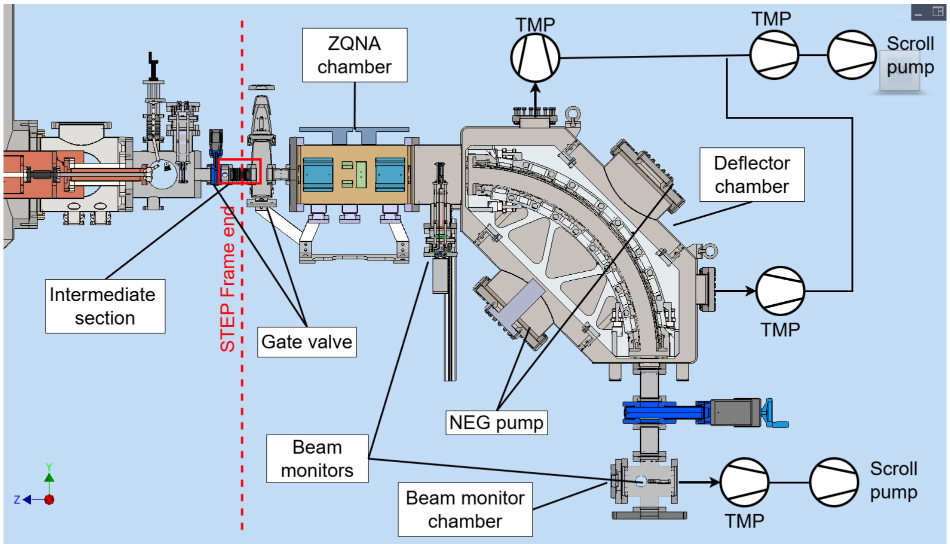

Figure 2.20: Section view of the entire beamline in the STEP experimental zone. The position of the transport frame is indicated as well as fig. 2.11. The connection to the vacuum pumps is also schematically depicted. The gate valve installed between the beam monitor chamber and the deflector chamber was originally installed and removed later because of a malfunction.

3 Development of the beam monitors

In front of the trap chamber where the antiprotons are captured and confined, there is the differential pumping section with the length of 696.5 mm and the diameter of 6 mm at the minimum. Because of this geometry, there is the angular acceptance as low as $\theta = 0.015\,\mathrm{rad}$. To reduce the effort to inject the beam into the trap, the beam monitors that are capable of monitoring the position of the beam are essential.

A concept of the beam monitor that four detector plates placed around the beamline axis collect the charged particles of the beam was proposed and some prototypes have been installed on the beamline. However, this beam monitor does not have enough precision for the beam near the beamline axis. Moreover, the electronics to amplify a small signal of the collected charge to a readable signal had instability of its response.

To overcome these problems, a new beam monitor composed of a grid of detectors, which enables the estimation of the beam position and its shape needs to be developed and installed, especially in the section in front of the trap. The electronics that work with enough stability also need to be developed by improving their design and parameters.

In this study, the new beam monitors were designed, assembled and tested using the antiproton beam and H^- ion beam from ELENA, and the electronics were also designed to achieve the readout of the signal. The control system to operate the beam monitors were also developed and described here.

As a result, the readout of the charge signal from the detector, the calibration of the beam monitors, and the estimation of the beam profile using the new beam monitor were achieved, while there is still some room to improve in the adjustment of the parameters for better accuracy.

3.1 Design

3.1.1 Mechanics

Currently, four beam monitors are installed on the BASE-STEP beamline. The common principle among these beam monitors is that metal parts acquire some charge from the collision of antiprotons with the parts and transmit the charge to the electronics placed outside the beamline vacuum. Here, the details of the design of each beam monitor are described.

First beam monitor

The first beam monitor in the beamline is placed in the vertical section, approximately 20 cm above the handover valve, which divides the beamline controlled by our experiment and the ELENA beamline. This beam monitor was developed earlier by F.Abbass et.al. This beam monitor has four metal plates with the inner diameter of 20 mm, which are placed around the beam axis and fixed on a holder part while keeping them isolated from the holder by using ceramic washers (Fig. 3.1). The holder is connected to the feedthrough flange, which has a 9-pin D-sub receptacle, by a metal rod, while each plate is connected to the pin of the feedthrough by bare copper wire. The feedthrough flange is connected horizontally on a cross flange on the handover valve. The position of the beam monitor was adjusted by inserting washers at the joint of the flange and the rod.

When the position of the beam is misaligned from the center of the beam monitor, plates closer to the beam center collect more particles than the other plates, thus generate a higher signal. When the the beam is aligned at the center of the beam monitor, these plates collect roughly equal amount of antiprotons, or no particles when the beam is focused.

Second beam monitor

The second beam monitor is placed behind the deflector chamber. It is composed of nine 1 mm diameter copper wires to collect antiprotons, a holder part to fix them, four rods to hold it on the position, and pedestal parts to connect the whole components on a feedthrough flange. 5 wires were placed horizontally and 4 were placed vertically to make a grid with approximately 4 mm gaps, as shown in Fig. 3.3(a). These wires were soldered onto ring terminal connectors and fixed to the holder across its aperture with ceramic washers for isolation after cleaning them in an ultra sonic bath. They

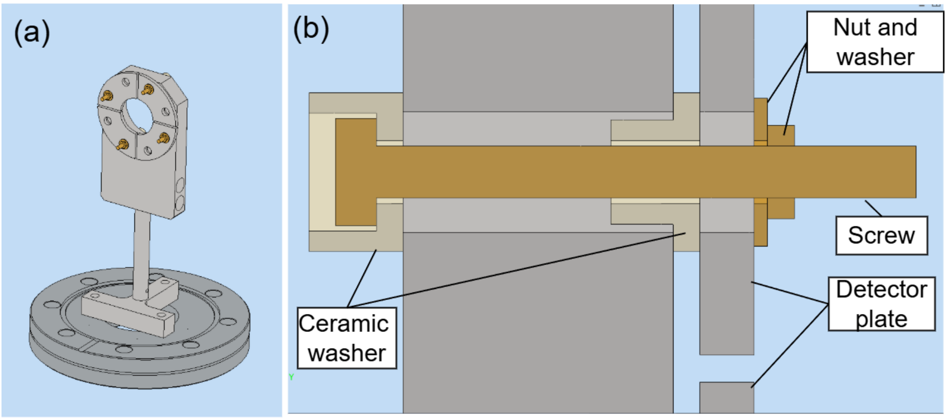

Figure 3.1: (a): A view of the first beam monitor. (b): A cross-sectional view of screwed connection between the detection plate and the holder part.

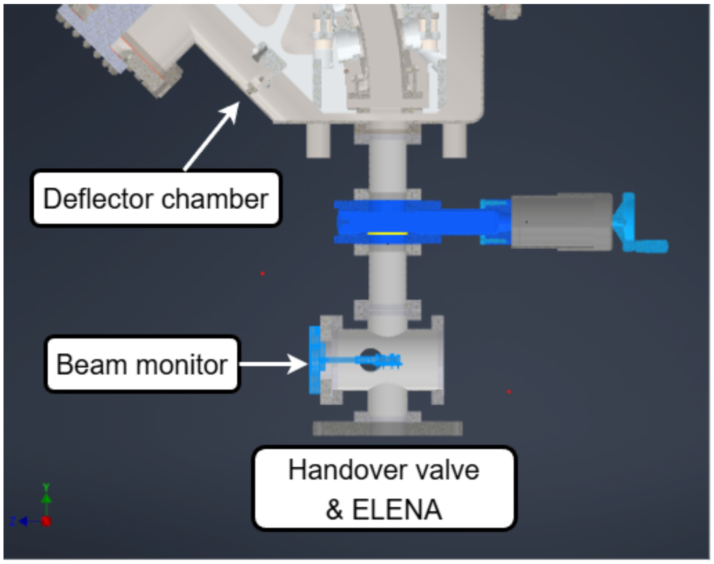

Figure 3.2: The location of the installed first beam monitor. The assembly is highlighted in blue.

were connected to the feedthrough flange with two 9-pin D-sub receptacles. The wires from the vertical lines and the wires from the horizontal lines were connected to different receptacles on the flange.

The wire holder was enclosed with 2 holder parts. These parts aim to protect the section of copper wires, which does not compose the detection grid, from the antiproton beam. The metal parts described above other than the copper wires were made from stainless steel 316L to reduce outgassing in the vacuum. For the same reason, specialized solder made from Tin, Silver and Copper was used for soldering.

To avoid the loss on the beam monitor when it is not needed and to adjust its position, the assembled beam monitor was installed on the beamline with a linear shift bellow (Hositrad HOBLT45S-02), which is able to adjust the length of the bellow by a screw.(Fig. 3.3(c))

Third beam monitor

The third beam monitor is located in the inlet chamber, the first vacuum chamber inside the STEP frame. Compared to the second beam monitor, this beam monitor has basically the same design, but it has nine copper bars with 4 mm width instead of copper wires. These wires were placed on the holder part with 7 mm intervals.

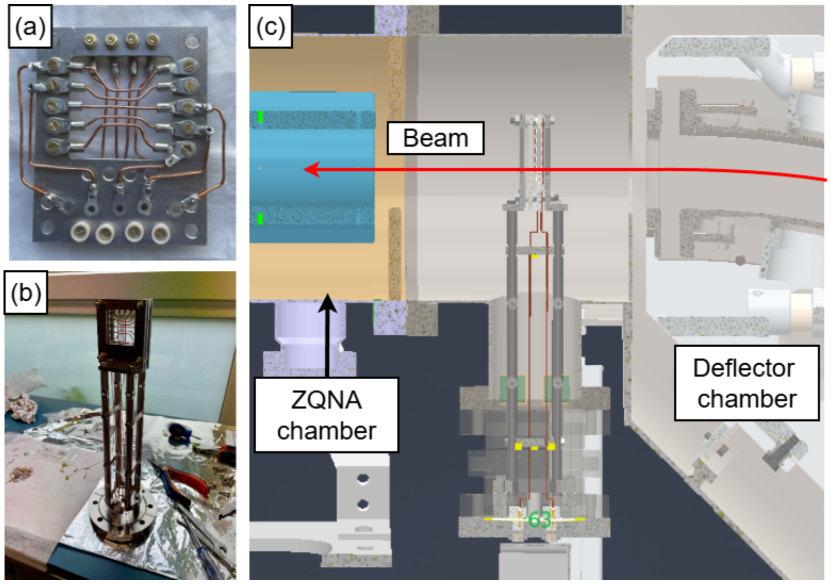

Figure 3.3: (a): A grid composed of copper wires. (b): The assembly of the second beam monitor. (c): The location of installation.

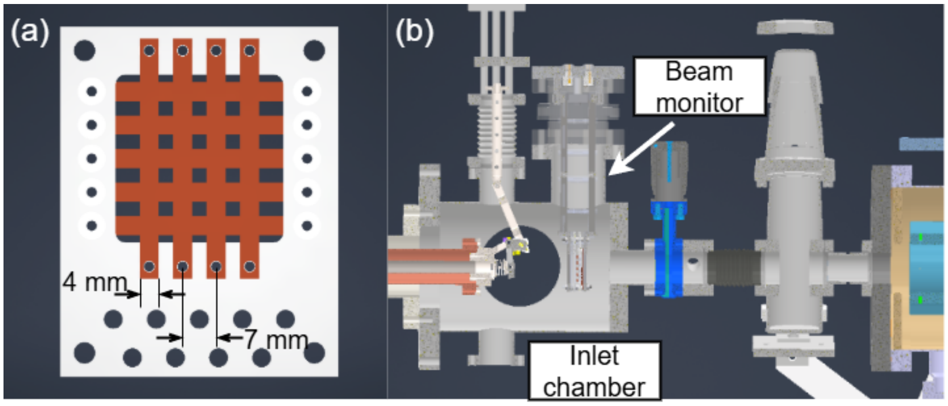

Figure 3.4: (a): The grid of the third beam monitor composed of copper strips. (b): The location of installation.

Fourth beam monitor

The fourth beam monitor is located at the entrance of the trap chamber, where the end of the differential pumping section is connected. There is a printed circuit board, which has aperture on its center and four bare copper planes surrounding the aperture, on the flange of the trap chamber. The copper planes work as detector plates and the charge is transmitted via wires to the feedthrough flange with a 9-pin D-sub connector, which is attached on the inlet chamber.

All of the beam monitors described above are connected to a feedthrough flange with D-sub 9-pin connectors for readout. To protect the weak signal of the collected charge that is typically a few millions elementary charges from external noise and crosstalks between neighboring channels, interface boxes, which convert the connector from D-sub to BNC, were placed on each flange, and the signal was transmitted via coaxial cables.

3.1.2 Electronics

As a cost-effective solution to read out signals on multiple channels, it was planned to read the signals by Arduino. Arduino Due has 12 analog input pins which can read an analog signal in a range from 0 V to 3.3 V quantized in 1024 steps.

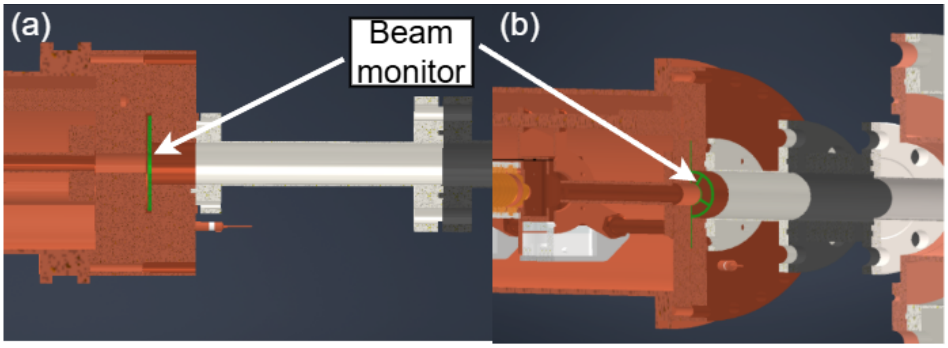

Figure 3.5: (a): Cross sectional view in the direction of the normal of cut plane. (b): An angled view of (a). The green colored component is the substrate of the fourth beam monitor, and brown planes on it is the detection plates made of copper planes.

Considering that the output from the beam monitor is a small charge signal and Arduino Due has sample rate of around 30 kHz (see appendix), a signal processing electronic circuit that amplify and prolong the charge signal is required.

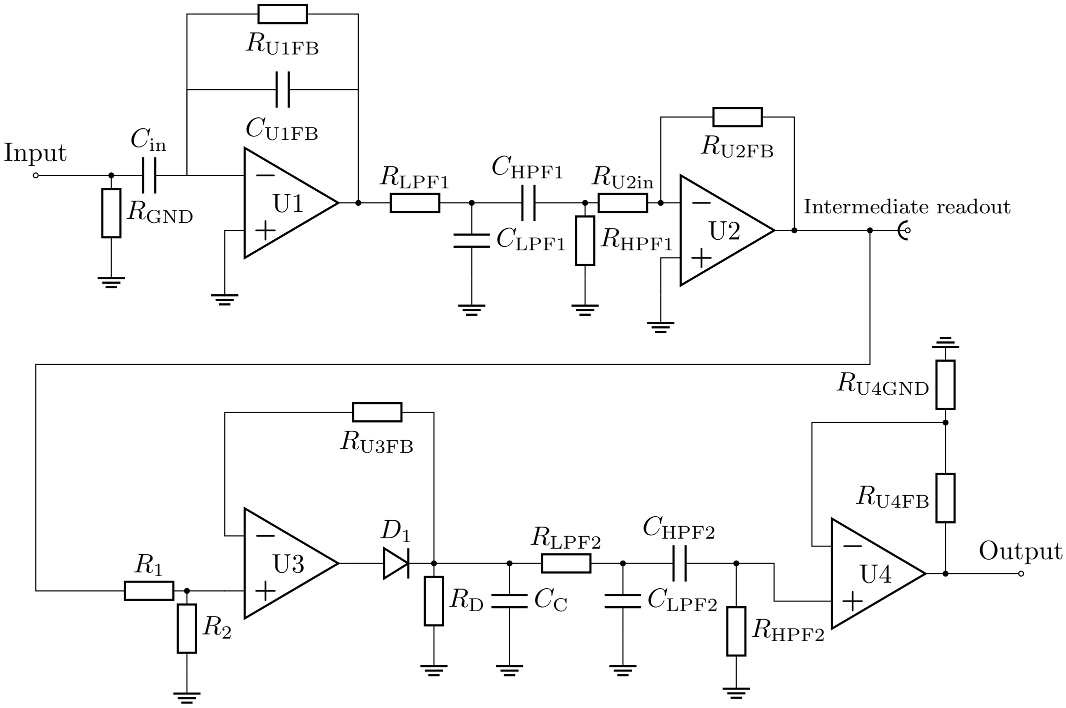

Figure 3.6: The whole diagram of the signal processing circuit.

The signal processing circuit was designed to have these functions. The diagram of the circuit is shown in figure 3.6. The circuit can be divided into four segments that each of them has one operational amplifier.

The first segment of the circuit, which is referred as the charge integrator here, aims to convert charge into a voltage pulse. It has a capacitor (C_{in}) and a grounded resistor (R_{GND}) at its input so that the input current pulse is converted into a voltage pulse and the accumulated charges on the input line are discharged. When the total amount of the input charge is Q_{in}, the coupling capacitor C_{in} will cause the voltage V_p

$$V_\mathrm{p} = \frac{Q_\mathrm{in}}{C_\mathrm{in}}. \tag{3.1}$$

The following op amp (LMV796, Texas Instruments) with feedback resistance and capacitance ($R_\mathrm{U1FB}, C_\mathrm{U1FB}$) amplifies the converted voltage pulse. Theoretically, when an AC current $I_\mathrm{in}(\omega) = \exp(-i\omega t)$ is put into the circuit and assuming the op amp is ideal, the output $V_\mathrm{out}(\omega)$ is calculated as

$$V_\mathrm{out}(\omega) = -I_\mathrm{in}(\omega)\left(\frac{1}{R_\mathrm{U1FB}} - i\omega C_\mathrm{U1FB}\right)^{-1}. \tag{3.2}$$

Therefore the gain of the circuit $G(\omega)$ at the frequency ω is

$$G(\omega) = \left(\frac{1}{R^2_\mathrm{U1FB}} + (\omega C_\mathrm{U1FB})^2\right)^{-\frac{1}{2}} \tag{3.3}$$

and

$$G(\omega) = \frac{1}{\omega C_\mathrm{U1FB}} \tag{3.4}$$

for high frequency ω and high R_U1FB.

A low-pass and high-pass filters (LPF and HPF) are placed following this segment to reduce noise.

The second segment is an ordinary inverting amplifier circuit using same op amp as the first segment. It amplifies the voltage pulse to a level high enough to activate the peak tracker circuit following this segment. Behind this segment, a SMA connector as intermediate readout for debugging and board evaluation, and resistors for impedance matching are placed.

The third segment is a peak tracker circuit, which detects and holds the peak of the input signal to output a longer pulse readable by the Arduino. When a pulse is put into this circuit, the output of the op amp (MCP661, Microchip Technology) follows the input and charges the capacitor placed beyond a diode (1N5711). After the input pulse ramps down, the diode prevents the voltage behind it from declining, while the grounded resistor placed in parallel with the capacitor discharges it slowly. The circuit is followed by the LPF and HPF optimized for longer pulses.

The final stage of the circuit is a non-inverting amplifier circuit using an op amp TLV 9151 by Texas Instruments. Its aim is to adjust the amplitude of the output signal in the range of 0 V to 3.3 V, which is the acceptable range of voltage of analog read by Arduino.

The op amps in the first three stages are supplied with bipolar voltages of ±2.5 V, and the last op amp is driven by voltages of ±3.3 V.

3.2 Simulation

Preceding the production of a test board for evaluation, the simulation of the circuit and optimization of the parameters were implemented. The simulation took place using PSpice for TI, the software provided by Texas Instruments and based on PSPICE.

3.2.1 Input

A bunch of antiprotons ejected from ELENA typically includes 10^7 antiprotons. When the beam diameter is 10 mm, which can be detected by multiple wires and the position can be estimated by the difference of the signal intensity, and antiprotons are spread uniformly, a wire with 1 mm diameter of the second beam monitor will be collided by approximately 1.2×10^6 antiprotons at maximum, which is equal to 1.9×10^{-13} C. The collision of particles with energy of 100 keV on a metal surface will cause the emission of secondary electrons, which leads to positive charges on the metal part. In the case of the collision of antiprotons, also the annihilation of antiprotons inside the copper wire will be another cause of the secondary electron emission. Although the number of emitted secondary electrons from a collision of a particle is not known well, I assumed that a collision of one antiproton causes two emitted secondary electrons and the detector part obtains the same amount of charges of that of the

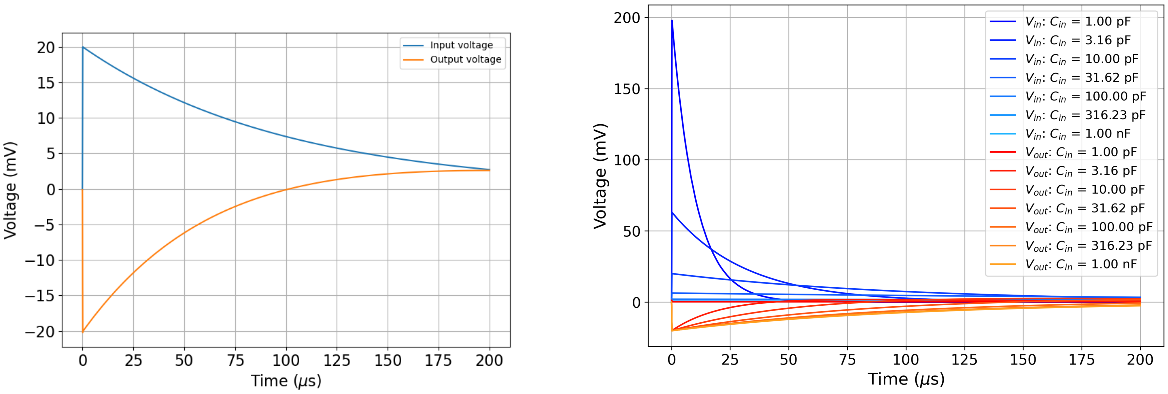

(a) The voltage waveforms of input and output of charge integrator when $C_{\mathrm{in}} = 10\,pF, R_{\mathrm{GND}} = 10\,\mathrm{M}\Omega, C_{\mathrm{U1FB}} = 10\,pF, R_{\mathrm{U1FB}} = 10\mathrm{M}\Omega$

(b) Multiple waveforms of input and output with swept C_{in} from 1 pF to 1 nF

Figure 3.7: Typical input and output and results with C_{in} sweeping

colliding antiprotons to estimate the signal strength. The simulations and optimization below took place under this assumption. Since the length of a bunch is expected to be 100 to 200 ns, a typical input is defined as a current pulse that has the rise and fall time of 100 ns, and the peak current is $-2\,\mu$A. The simulations discussed below took place using this input unless mentioned especially.

3.2.2 Charge integrator

At first, a simulation around the charge integrator with the parameters of $C_{\mathrm{in}} = 10\,pF, R_{\mathrm{GND}} = 10\,\mathrm{M}\Omega, C_{\mathrm{U1FB}} = 10\,pF, R_{\mathrm{U1FB}} = 10\mathrm{M}\Omega$ was implemented. As shown in fig. 3.7, the result showed that the input current pulse induces a negative voltage pulse which has $-20\,$mV peak and $30\,\mu$s FWHM (fig. 3.7(a)) and the charge integrator transmits the signal resulting in a positive voltage pulse output with the same peak height and $\tau_{\mathrm{out}} = 70\ \mu$s FWHM (fig. 3.7(b)). A simulation with sweep of C_{in} from 1 pF to 1 nF followed it to define the coupling between the input and the charge amplifier. Because of the relation between a voltage applied on a capacitor and its charges $V = Q/C$, the peak voltage of the input pulse is proportional to the inverse of the input capacitance C_{in}, and a larger grounded resistor causes longer discharging of the collected charge, thus the longer pulse. On the other hand, it was shown that the difference in C_{in} does not affect the intensity of the output signal from the charge integrator.

Following them, the simulations with the sweeping of the feedback capacitor and resistor were implemented. It resulted in the peak height of the output voltage being inversely proportional to the feedback capacitance (fig. 3.8a,3.8b), which validates the theoretical expectation $V_{\mathrm{out}} = -Q_{\mathrm{in}}/C_{\mathrm{U1FB}}$. The larger feedback resistance led to a longer output pulse, while both of the feedback resistance and capacitance did not affect the shape of the input voltage pulse.

The cutoff frequency of the HPF and LPF is determined as $f_c = 1/2\pi RC$, where R and C are the resistance and capacitance composing the filter. The parameters of the filters are determined to pass the frequency $1/\tau_{\mathrm{out}} = 14\,$kHz characterizing the output signal of the charge integrator.

$$\begin{aligned} R_{\mathrm{LPF1}} &= 1\,\mathrm{k}\Omega \\ C_{\mathrm{LPF1}} &= 47\,\mathrm{pF} \\ R_{\mathrm{HPF1}} &= 100\,\mathrm{k}\Omega \\ C_{\mathrm{HPF1}} &= 1\,\mathrm{nF} \end{aligned}$$

Fig. 3.9b shows the comparison of the waveforms of the input and output of the filters. The peak height of the output signal was about 90 % of that of the input signal, while the pulse length of the output was shorter by a factor of 4 than the input signal. Fig. 3.9a shows the frequency response of the filters and the frequency spectrum of the input and output signals of the filters from 1 kHz to 10 MHz. The filters transmit 90 % of the input amplitude for the frequencies from 100 kHz to 1 MHz.

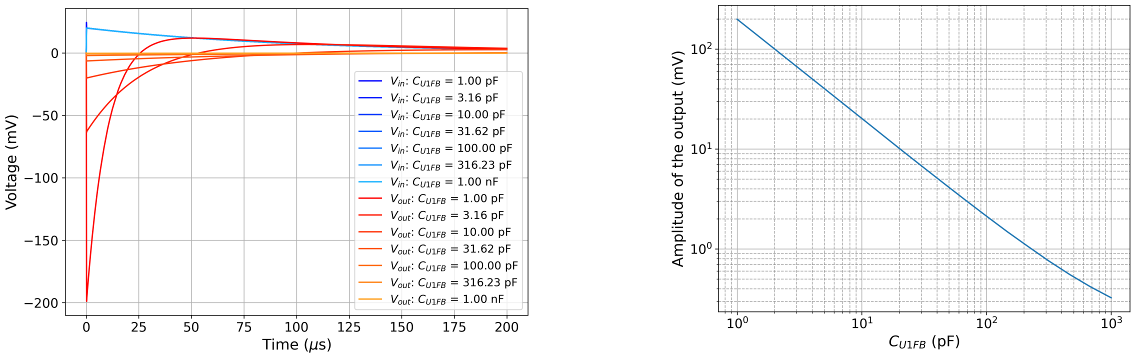

(a) The voltage waveforms of the input and the output of the charge integrator at each C_{U1FB} from 1 pF to 1 nF.

(b) The dependency of the peak voltage of the output signal from the charge integrator on C_{U1FB}, from 1 pF to 1 nF.

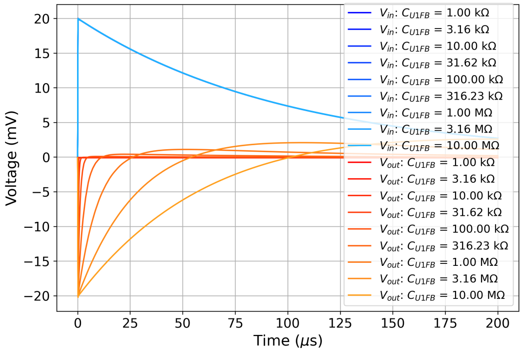

(c) The voltage waveforms of the input and the output at each R_{U1FB} from 1 kΩ to 10 MΩ.

Figure 3.8: Results of simulation with sweeping of C_{U1FB} and R_{U1FB}

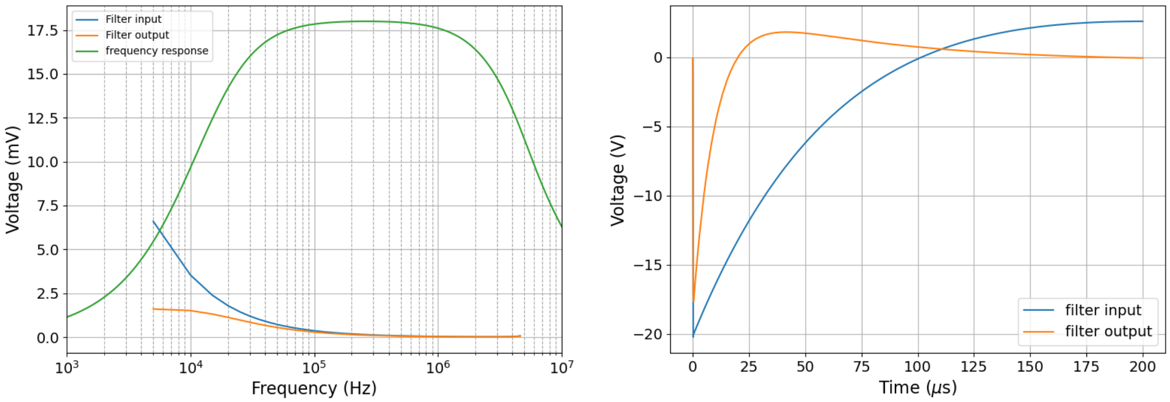

(a) Frequency response of the combination of the HPF and LPF (green). Sine waves of 20 mV amplitude was put into the filters at the each frequency. The vertical axis is the amplitude of the output wave. Blue and orange lines are the frequency spectrum of the input and output signal of the filters.

(b) Comparison of input and output waveforms of the filter when the input current pulse of 2 μA is put into the charge integrator.

Figure 3.9: The results of simulations around the filters

The Fourier spectrum of the input signal has higher amplitudes at lower frequencies below 10 kHz, and the components in the range of the frequency are suppressed by the filter, which is supposed to be the cause of the shorter output pulse.

3.2.3 Peak tracker circuit

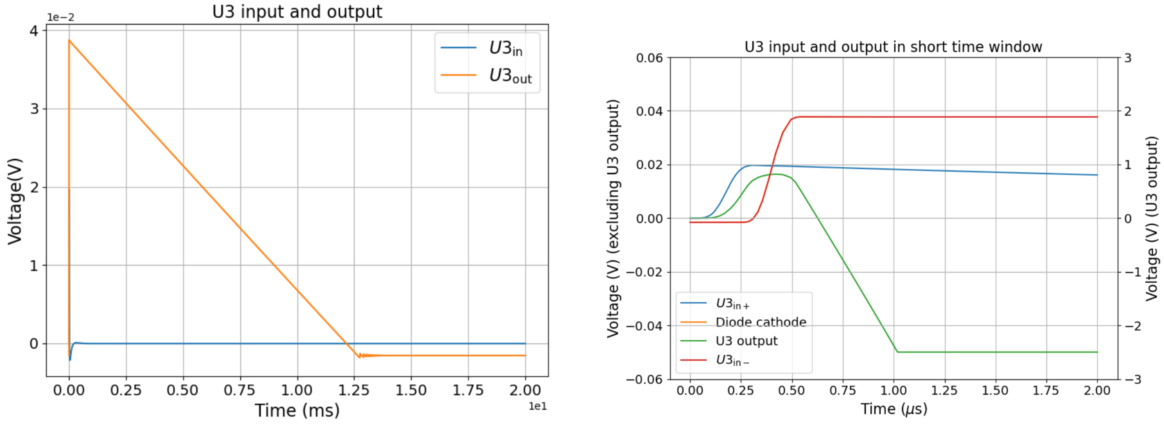

(a) The waveform of the input and output of the peak tracker circuit.

(b) The waveforms of each node around the peak tracker. The waveform of diode cathode is not visible because it is almost identical to that of U3 in_-

Figure 3.10: The results of the simulation of the peak tracker circuit.

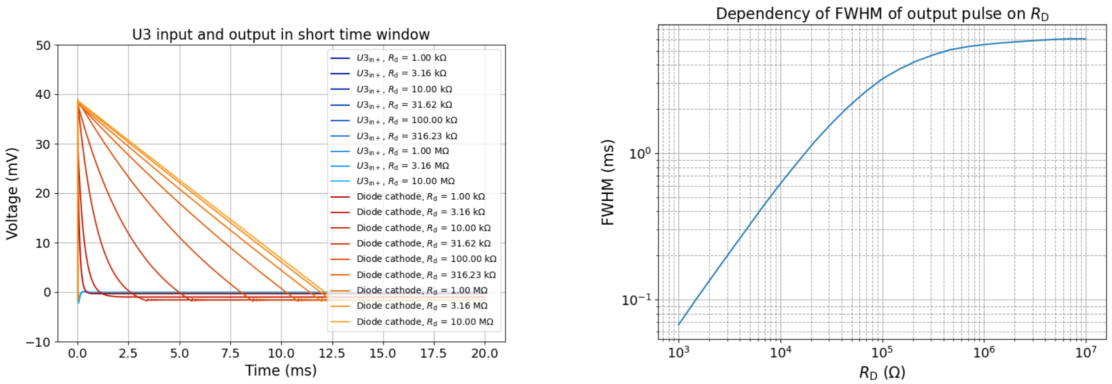

(a) The waveforms of the output of the peak tracker with various R_D value

(b) The dependency of the FWHM of the output pulse on R_D

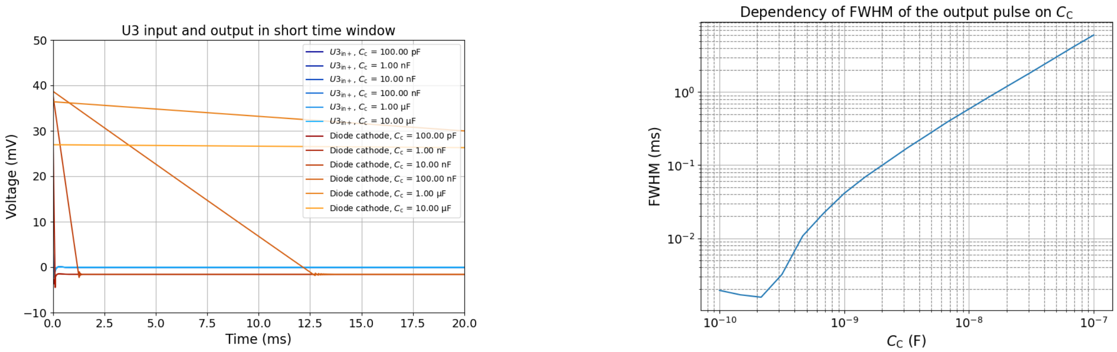

(c) The waveforms of the output of the peak tracker with various C_C value

(d) The dependency of the FWHM of the output pulse on C_C

Figure 3.11: The results of simulations with sweeping of R_D and C_C

Regarding the Peak tracker circuit, its functionality was checked by simulating it with parameters of $R_{\mathrm{D}} = 1\,\mathrm{M}\Omega, C_{\mathrm{C}} = 100\,\mathrm{nF}, R_{\mathrm{U1FB}} = 100\,\Omega$ (Fig. 3.10a). It showed that the circuit converted the input signal to a longer pulse with 5 ms FWHM.

The responses of each nodes around the circuit, two inputs and the output of the op amp (U3), and the cathode side of the diode, which is also the output of the peak tracker, were also investigated in a short time window (Fig. 3.10b). It shows that as soon as the input voltage ($\mathrm{U3}_{\mathrm{in+}}$) ramps up, the output of the op amp also ramps up. However, the voltage on the cathode pole of the diode does not rise immediately because of the non-linear relation between the forward voltage and the forward current of the diode. The output voltage did not immediately fall even after the voltage of the diode cathode and the inverting input of the op amp exceeded the non-inverting input. The cause of this phenomenon may be the phase delay of the op amp because of the large capacitive load C_C. As a result, the voltage on the cathode side of the diode continued to increase over the input voltage level and reached $40\,\mathrm{mV}$, twice the input amplitude.

The influence of each parameter on the output signal was also investigated by sweeping them. A simulation with sweeping of the discharging resistor R_{D} and the charging capacitor C_{C} resulted in that the FWHM of the output pulse was proportional to both R_{D} and C_{C}, while it was constant at higher R_{D}, probably due to the parallel resistivity of the surrounding components. It also showed that too large C_{C} leads to a decrease of the output signal because the output voltage rises slower to charge up the large capacitance.

The sweeping of R_{U3FB} from $10\,\Omega$ to $1\,\mathrm{M}\Omega$ was also implemented. It showed that the peak height of the output of the peak tracker increased at R_{U3FB} larger than around $1\,\mathrm{k}\Omega$. Since it was observed that the voltage on the IN- pin of the op amp was low and rose slower than the cathode of the diode, the reason of this effect is supposed to be that the voltage on the IN- pin of the op amp is decreased by a voltage divider made of the feedback resistor and input impedance of the op amp and the cathode voltage keeps rising until IN- voltage reaches to IN+ voltage.

The nonlinearity of the response of the peak tracker circuit is a remarkable aspect of it. Because of the nonlinear $V_F - I_F$ response of the diode, the output of the peak tracker is not proportional to its input when it is higher than a certain level. Fig. 3.13 shows the dependency of the output peak voltage on the input peak voltage. The output voltage is proportional to the input in the range of $V_{\mathrm{in}} < 0.16\,\mathrm{V}$, while the slope decreases in the regime beyond the voltage. The input voltage where the output voltage becomes nonlinear to the input was determined as $0.16\,\mathrm{V}$ by the fitting of the curve.

To achieve the output pulse with the length of $10\,\mathrm{ms}$ scale, C_{C} and R_{D} were set to $100\,\mathrm{nF}$ and $1\,\mathrm{M}\Omega$, and R_{U3FB} was set to $100\,\Omega$.

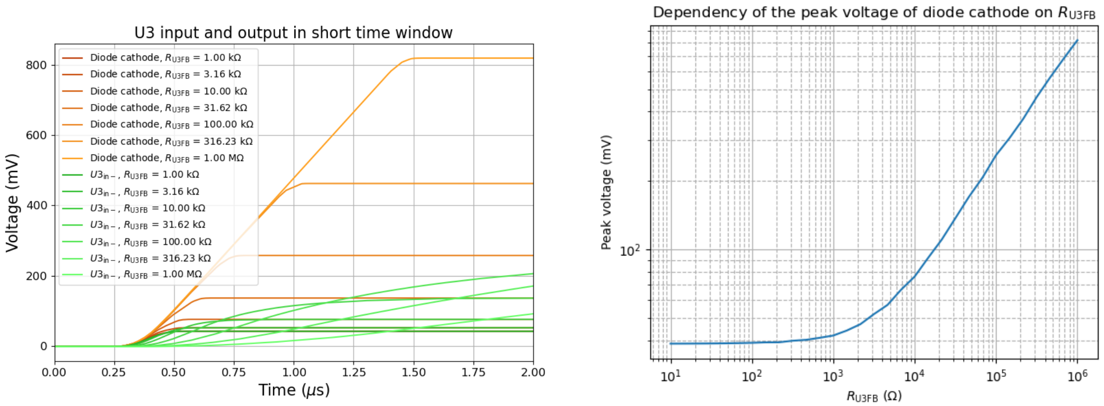

(a) The waveforms of the output of the peak tracker (diode cathode, red) and the IN_- pin ($\mathrm{U3}_{\mathrm{in-}}$, green) at varied R_{U3FB}. Although R_{U3FB} was varied from $10\,\Omega$ to $1\,\mathrm{M}\Omega$, data points of R_{U3FB} below $1\,\mathrm{k}\Omega$ were omitted since they are almost identical

(b) The dependency of the output peak on R_{U3FB}

Figure 3.12: The results of simulations with sweeping of R_{U3FB}. The input is the current pulse with a $2\,\mu\mathrm{A}$ peak defined above.

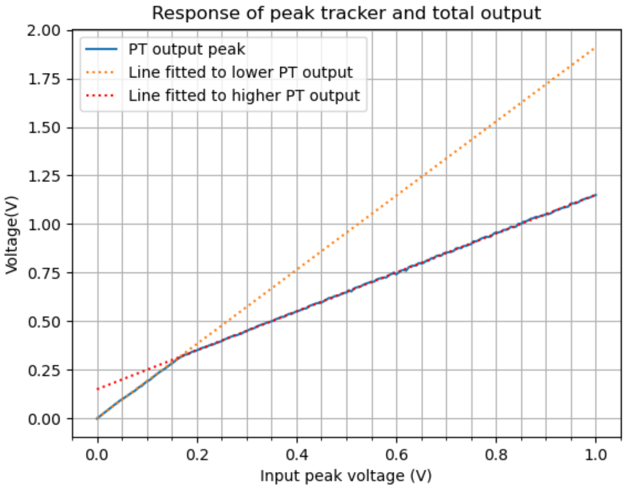

Figure 3.13: The dependency of the output of the peak tracker on the input voltage.

3.2.4 1st and 2nd amplifiers and total output

The peak of the final output of the entire circuit is required to be in the range of 0 V to 3.3 V. The adjustment of the gain of the circuit can be done by modifying the gains of the two amplifiers which are placed after the charge integrator and the peak tracker, respectively.

Since a linear circuit output makes it easy to estimate the position and shape of the beam, the nonlinearity of the response of the peak tracker argued above is a main limitation against the gain of the first amplifier G_1. The input peak voltage of the peak tracker needs to be below 0.16 V at maximum in order to achieve the linearity of the output.

Since a bunch of the beam from ELENA contains 10^7 antiprotons, the maximum input current would have a peak current of 16 μA. Fig. 3.14 shows the dependency of the input to the peak tracker on R_{U2FB} that determines the gain of the first amplifier. While the input voltage is linear to the gain, the output is linear at $R_{\mathrm{U2FB}} \leq 33\,\mathrm{k}\Omega$, where the input of the peak tracker is under 0.16 V. Based on this result, R_{U2FB} was determined as 22 kΩ.

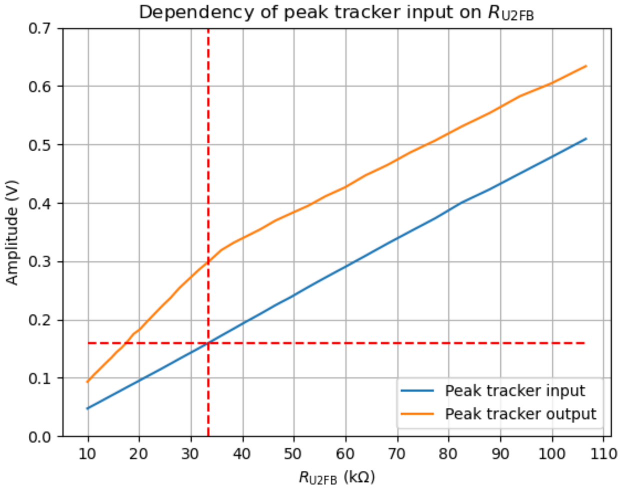

Figure 3.14: The dependency of the output of the peak tracker on the gain of the first amplifier. The two red dashed lines represent 33 kΩ and 0.16 V.

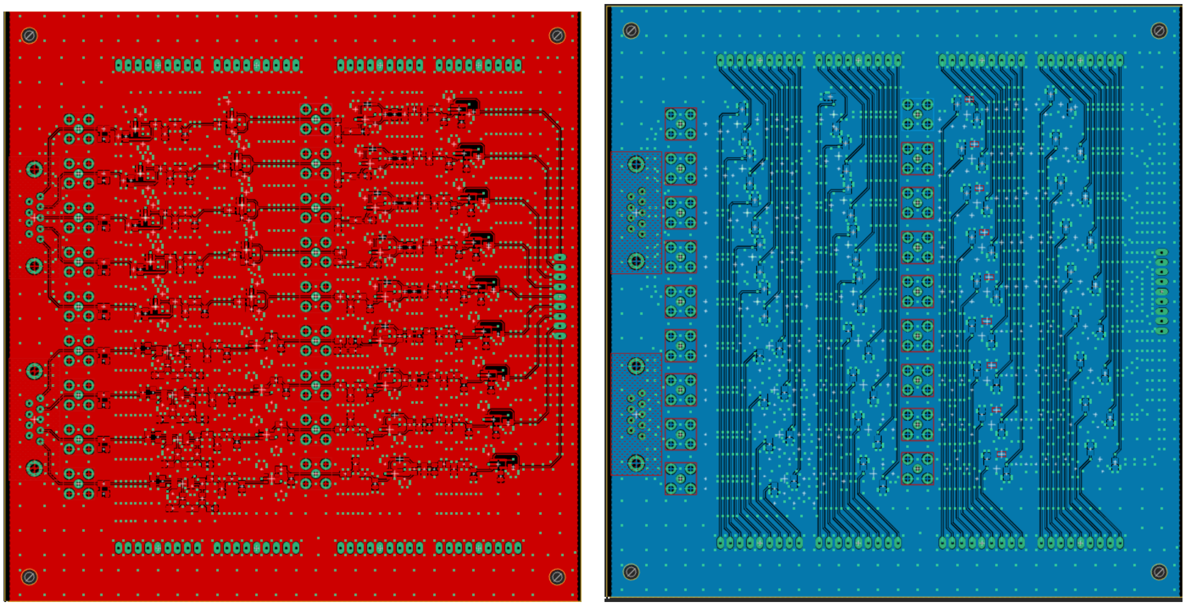

(a) The top side of the PCB design. The input connectors are placed on the left side and the amplifiers are placed in-line at each channel. Via holes are placed along the wire to minimize the influence of the noise.

(b) The bottom side of the PCB design. The connectors for the positive and negative biasing are placed on the top and bottom sides, respectively. The buffer capacitors are placed on this side near the pins of the op amps.

Figure 3.15: The design of the signal processing board.

3.3 PCB design and evaluation

After the simulations above, a printed circuit board (PCB) was designed and built. The beam monitor has nine channels to transmit the signal at most, so a single PCB is required to have nine independent channels to amplify the signal. This number of channels also covers two plate-type beam monitors which have four channels per one.

The designed PCB is a 4-layer board made of FR-4 substrate and $35\,\mu\mathrm{m}$ copper layers with $152\,\mathrm{mm} \times 140\,\mathrm{mm}$ size. The wire patterns and components to transmit the signal were placed on the top side of the board linearly to avoid producing a parasitic inductance. The patterns for powering of the op amps and buffer capacitors connected between power lines and ground were placed on the bottom side of the board. Two D-sub connectors were placed for the signal input, and a 9-pin header was placed for the output. Additionally, SMA connectors were placed after the first amplifier for the intermediate readout.

The evaluation of the board was implemented by putting a voltage signal generated by a function generator. The waveform of the input signal was set as a pulse that has 200 ns rise time and $20\,\mu$s fall time to imitate the voltage waveform at the input that appeared in the simulations above.

The amplitude of the input signal varied from 0 mV to 30 mV by 5 mV steps, which corresponds to 0 to approximately 2×10^7 antiprotons.

Fig. 3.16a shows the dependency of the amplitudes of the total and intermediate outputs on the amplitude of the input signal. The amplitude of the intermediate output followed a linear response matching the results of the simulations, with the gain from the input voltage to the intermediate output of $G_{\mathrm{IM}} = V_{\mathrm{IM}}/V_{\mathrm{IN}} = 23.2$. Although the total output was also linear to the input amplitude with the total gain of $G_{\mathrm{tot}} = V_{\mathrm{tot}}/V_{\mathrm{IN}} = 203.1$ at the input voltage below 11 mV , it was lower than the linear response at the input higher than 11 mV. The response of the total output was fitted by a line function

$$V_{\mathrm{tot}}(V_{\mathrm{IN}})[\mathrm{mV}] = 99.0V_{\mathrm{IN}} + 1.050 \times 10^3\,[\mathrm{mV}]. \tag{3.5}$$

Although the shift from the linear output can cause errors on the estimation of the position and the spread of the beam, no correction was done for the estimation of the beam profile discussed above. A correction for this shift can be achieved by approximating the total output by two lines. The gain of the first amplifier can be set lower to use the lower range of the input for the peak tracker. The gain of the second amplifier needs to be increased to compensate the lower output from the peak tracker.

The tests of crosstalk produced by adjacent channels were also implemented. In these tests the function generator was connected to channel 1, and voltage signals from 10 mV to 50 mV peak voltage were input by 10 mV steps. The neighboring channels of the input channel, channel 2 to 5, were measured by the oscilloscope. The results (Fig. 3.16b) shows that the signals induced on the neighboring channels slightly rise as the input signal gets higher, but they are below the level of 10 mV compared to 3.3 V for the full output range.

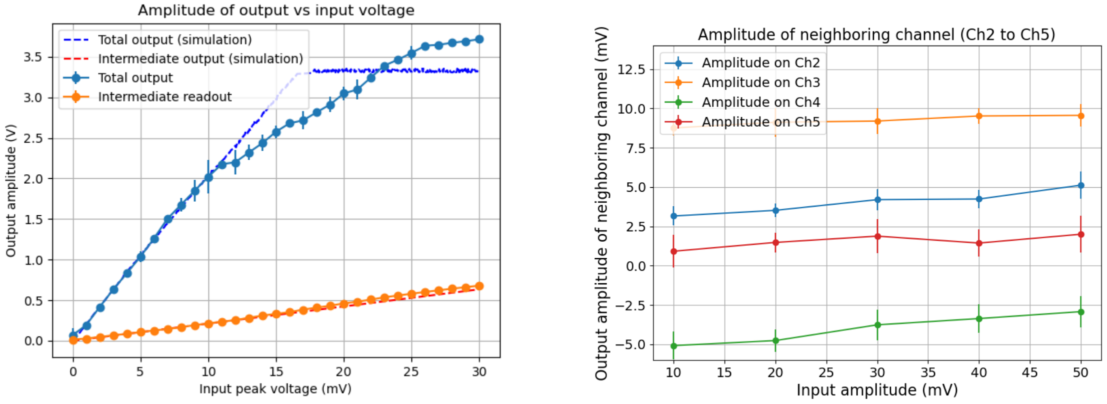

(a) The plot of the amplitudes of intermediate and total output. The dashed lines are the simulation results.

(b) The amplitudes of each neighboring channel at input voltage of 10 to 50 mV.

3.4 Software

The software for reading the amplitude of the signal from the beam monitors is described here.

The Arduino Due has 12 pins (A0 to A11) that can read voltage analogically. Nine of them (A1 to A9) are connected to the output pins of the signal processing board, and one of them is connected to a trigger source.

Arduino waits for a trigger from the source by recursively reading the voltage on the A0 pin in the loop structure of its code. Once the voltage on the pin exceeds 1 V, it starts reading the voltages on A1 to A9. In this phase, the voltages on A1 to A9 are read in order, and it is iterated 1000 times. The measured values are stored in an array variable as waveforms, and the maximum value of each channel is extracted from the array. Both the maximum values and waveforms are transmitted to a computer connected to the Arduino.

The data sent from the Arduino are displayed and saved by a LabVIEW program running on the computer. It waits for the data by checking if there are bytes at the port continuously, and receives all of the data.

```
int trig = A0;
int ai1 = A1;
int ai2 = A2;
int ai3 = A3;
int ai4 = A4;
int ai5 = A5;
int ai6 = A6;
int ai7 = A7;
int ai8 = A8;
int ai9 = A9;

float value = 0;
int num_channels = 9;
int iter = 1000;

void setup() {
SerialUSB.begin(115200); // Initialize serial communication
SerialUSB.setTimeout(5000);
```

```
//SerialUSB.println("serial setup");
}

void loop() {
value = analogRead(trig); // Read the analog input
short valuearray[num_channels][iter];
if (value >= 512/3.3) {
  for (int n = 0; n <= iter -1; n++){
    for (int i = 0; i <= num_channels -1; i++){
    value = analogRead(55 + i);
    valuearray[i][n] = value;
    }
  }
  String delimited_string = "";
  float Maxvollst[num_channels];
  for (int i = 0; i <= num_channels -1; i++){
    float Maxvalue = findMax(valuearray[i], iter);
    Maxvollst[i] = Maxvalue /1023 *3.3;
    if(i<num_channels -1){
      delimited_string = delimited_string + Maxvollst[i] + ",";
    }else{
      delimited_string = delimited_string + Maxvollst[i];
    }
  }
  SerialUSB.println(delimited_string);

  for(int i = 0; i < num_channels; i++){
      delimited_string = "";
      for (int n = 0; n< iter; n++){
        if(n < iter -1){
          delimited_string = delimited_string + valuearray[i][n] +",";
        }else{
          delimited_string = delimited_string + valuearray[i][n];
        }
      }
      SerialUSB.println(delimited_string);
      delimited_string = "";
  }
  }
}

float findMax(short arr[], int size) {
  float maxVal = arr[0];
  for (int i = 1; i < size; i++) {
    if (arr[i] > maxVal) {
      maxVal = arr[i];
    }
  }
  return maxVal;
}
```

Listing 1: Arduino code

3.5 Commissioning of the beam monitors

The signal processing PCB and Arduino board were placed in a rack mount case sized 88 mm × 483 mm × 250 mm. As auxiliary boards, voltage distributor boards and signal swapper boards are also placed inside the case. The voltage distributor board is designed to distribute the voltage input from a power supply to each channel on the signal processing board and has terminal blocks for input and 9 pin connectors for output. Its inputs are connected to BNC adapters placed on the front panel of the case, and the outputs are connected to the power supply pins of the signal processing board by ribbon cables. The signal swapper board is used to change the order of the pins of D-sub connectors to that of feedthrough flange of the beam monitors.

The front panel of the electronics case has 4 BNC adapters for the power supply that are biased ±2.5 V, ±3.3 V respectively and 2 D-sub connectors to connect to the beam monitors. There is also an aperture to insert the cable from a computer to the Arduino board. A DC power supply was connected to the BNC adapters, and the D-sub connectors for signal input were connected to the feedthrough flange of the second beam monitor by coaxial cables soldered onto the D-sub connectors channel by channel.

Additionally, 2 signal processing boards were ordered and placed in the second electronics case. The inputs of the signal processing boards were changed from D-sub connectors to bare pads on which wires were soldered directly, and the D-sub connectors on the front panel of the case were also changed to 9 BNC connectors.

The power supply used above was connected to this box, and BNC connectors for inputs were connected to the remaining beam monitors via interface boxes that has D-sub and BNC connectors and are mounted on each feedthrough flange.

As a trigger source for the Arduino boards, a delay generator (Stanford Research Systems, DG645), which receives a trigger timed of the bunch ejection from ELENA and generates pulses with controlled delay, was connected, while the other outputs of the DG645 triggered also other injection-related components.

3.6 Measurements using the beams from ELENA

3.6.1 Calibration of beam monitors

At first, the calibration of the beam monitors was attempted using the antiproton beam from ELENA.

To this end, the beam was scanned on the first beam monitor by the steerer located on the transfer line from ELENA to the BASE-STEP experimental zone to direct all antiprotons onto a single detection plate.

The beam steerer has 2 sets of bipolar electrodes to bend the beam horizontally and vertically, and 2 sets of quadrupole electrodes to focus the beam in the horizontal and vertical directions. For the scanning on the first beam monitor, the vertical bipolar electrodes were used. At first, the beam was adjusted to the near-centered position and steered gradually to the detection plate.

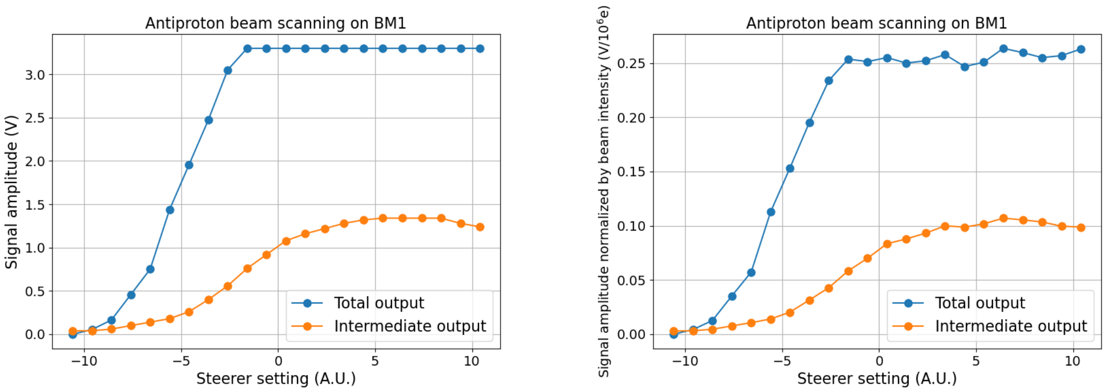

(a) The amplitudes of intermediate and total output of the first beam monitor.

(b) The amplitudes normalized by the beam intensity

Figure 3.17: The results of scanning on the first beam monitor. The horizontal axis is the value of steering system provided by CERN. A unit of the horizontal axis corresponds to approximately 101 V of the voltage of the steerer.

Fig. 3.17 shows the intermediate and total outputs from the plate that the beam was directed. As the beam steered to the detection plate, the amplitude of the total output increased and saturated at 3.3 V, while the intermediate output amplitude also rose and stabilized around 1.3 V within a certain range of the steering setting. The plot of amplitudes normalized by the intensity of the antiproton beam also showed stabilization around 0.10 V per 1 million antiprotons. By taking the last 7 data points, the normalized amplitude of the intermediate output is concluded to be 0.102(3) V per 1 million antiprotons. Using the gain of the intermediate output $G_{\mathrm{IM}} = 23.2$ and the ratio of the input voltage to the input charge $V_{\mathrm{IN}}/Q_{\mathrm{IN}} = 1.6\,\mathrm{mV}/(10^6\bar{p})$, the input charge when 1 million antiprotons are caught by a detector is $Q_{\mathrm{IN}} = 2.7 \times 10^6 e$. This means that a collision of an antiproton on a detector plate causes the emission of the 3.7 secondary electrons on average.

Amplitude (V)	Beam intensity ($\times 10^6 e$)	Normalized amplitude ($\mathrm{V}/10^6 e$)
1.32	13.37	0.099
1.34	13.16	0.102
1.34	12.52	0.107
1.34	12.71	0.105
1.34	12.94	0.104
1.28	12.85	0.100
1.24	12.55	0.099

Table 3.1: The amplitudes and beam intensity of the last 7 data points

Although the total output amplitude gets saturated for the entire beam, the calibration of the total output can be done by using the relation between the intermediate output and the total output. The total output as a function of the intermediate output amplitude $V_{\mathrm{tot}}(V_{\mathrm{IM}})$ can be obtained by $G_{\mathrm{tot}}/G_{\mathrm{IM}}$ for the lower range of the input voltage where both of the outputs are linear to the input, and substituting $V_{\mathrm{IM}} = G_{\mathrm{IM}} V_{\mathrm{IN}}$ into the function $V_{\mathrm{tot}}(V_{\mathrm{IN}})$ (fig. 3.5)

3.6.2 Calibration with the H^- ion beam

The measurement using the H^- ion beam from ELENA with the same configuration as above was also done, and the results are shown in Fig. 3.18. Because the intensity of the H^- beam has a large fluctuation, 5 beam shots were taken per one setting of the steerer.

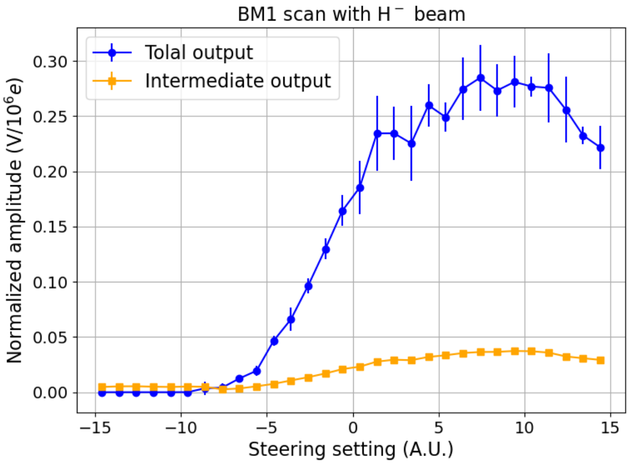

Figure 3.18: The signal amplitudes of H^- beam normalized by the beam intensity

Fig. 3.18 shows the amplitudes normalized by beam intensity. While the amplitudes similar dependency on the steerer setting, it yielded lower signal than the case of the antiproton beam. The normalized amplitudes at the steering setting at which the total output is maximum are $0.28(3)\,\mathrm{V}/10^6 e$ for the total output and $3.6(1) \times 10\,\mathrm{mV}/10^6 e$ for the intermediate output. As well as the antiproton beam, the input charge when 1 million H^- ions hit on a detector can be calculated as

$$Q_{\mathrm{IN},H^-} = 9.6(3) \times 10^5 e, \tag{3.6}$$

which means 1.96 secondary electrons per collision of a H^- ion. The difference in the rate of the number of the secondary electrons implies a considerable contribution by the annihilation of the antiprotons to the amount of the secondary electron emission.

3.7 Measurements during beam steering

For the goal of injecting into and catching antiprotons inside the BASE-STEP trap, steering and focusing of the beam are needed. The beam monitors are required to be able to estimate the position and diameter of the beam.

To demonstrate the estimation of the beam profile, the beam scanning on the third beam monitor was implemented.

The beamline in the STEP experimental area has the deflector chamber that bends the beam from vertical to horizontal direction and the ZQNA chamber that can steer and focus the beam vertically and horizontally. The third beam monitor is located in the inlet chamber inside the STEP trap frame, and has 9 copper bars with 4 mm width composing a grid. In this measurement, the ZQNA horizontal steerer was used because the vertical copper bars are placed facing the upstream side and they could block the detection by the horizontal bars placed on the downstream side. The electrodes of the ZQNA chamber were applied with voltage by 100 V steps up to ±1500 V. In addition to the total output read by the Arduino board, the intermediate output ports of 3 copper bars among 4 vertical bars were connected to a oscilloscope to read the intermediate signals.

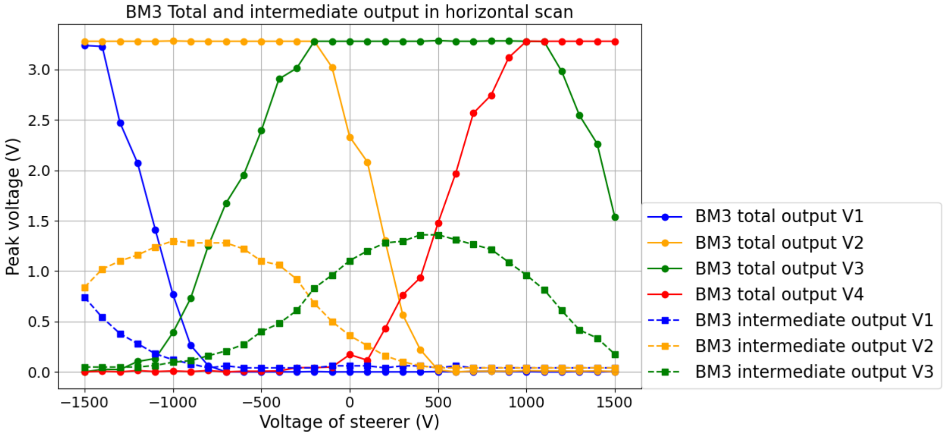

Figure 3.19: The signal during horizontal scanning on Beam monitor 3.

Fig. 3.19 shows the change of the signal amplitudes during the beam scanning in the horizontal direction. The amplitudes of vertical copper strips showed changes as the voltage of the steerer changed. The position and width of the beam can be estimated by fitting of gaussian on the amplitudes of channels V1 to V4 at each steerer condition.

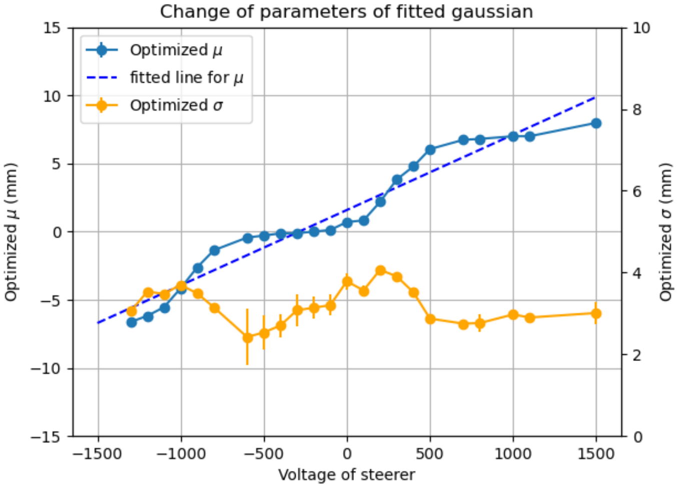

Figure 3.20: The optimized parameters of gaussian fitting on the amplitudes of vertical channels at each condition.

Fig. 3.20 shows optimized parameters of gaussian fitting on the amplitudes of vertical channels at each steerer condition. The fitting failed to converge at some condition because of the insufficient data points. The optimized μ that means the position of the center of the beam shifts with the increase of the voltage at the steerer, while there are some plateaus where μ shifts less due to the saturation of amplitudes. The rate of shift of the beam against the voltage was determined to be 5.5×10^{-3} mm/V by fitting a line to the result. The beam width σ was optimized in a range of 2 to 4 mm

The beam shape can be estimated by another way. The amplitude can be expressed as a definite integral of the gaussian in the interval $[-2, 2]$ that represents the copper strip:

$$V_{\text{out}} = \int_{-2}^{2} dx \frac{A}{\sqrt{2\pi}\sigma} \exp[-\frac{(x(V_{\text{steer}}) - \mu)^2}{2\sigma^2}] \tag{3.7}$$

where A is the scale factor of the signal, μ is the position of the copper strip relative to the center of the beam monitor, and $x(V_{\text{steer}})$ denotes the position of the beam, as a function of the voltage of the steerer. $x(V_{\text{steer}})$ can be written as $x(V_{\text{steer}}) = 5.53 \times 10^{-3} V_{\text{steer}} + 1.588$ using the result of the analysis above.

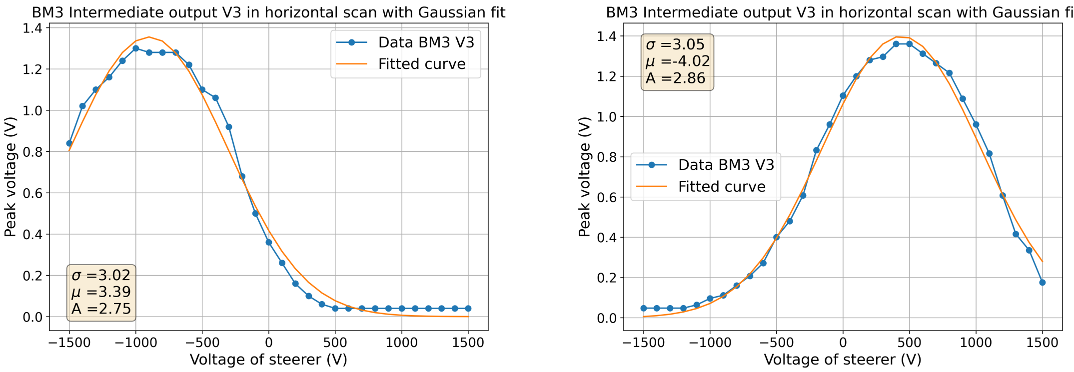

(a) Result of V2 channel.

(b) Result of V3 channel.

Figure 3.21: The amplitudes of intermediate output of V2 and V3 and fitting curve.

This function was fitted to the intermediate output of the channel V2 and V3, which showed their rises, peaks, and falls in the window of the steering voltage. Fig. 3.21 shows the amplitudes of channel V2 and V3 and their fitted curves. The optimized σ converged around 3 mm at both channels, which is also consistent with the gaussian fitting above. The optimized μ also converged to the position of copper strips with errors up to 0.5 mm.

3.8 Conclusion

As a conclusion, the developed electronics enabled the amplification of the charge of a $10^6 e$ level produced by the collision of the antiprotons and H^- ions to voltage pulses of a few volts. The amplification circuit yielded the linear response in the range of lower inputs, though the output shifted lower in the higher range. This shift can be removed by adjusting the gain of the amplifiers to use only the lower range.

The calibration of the beam monitor revealed the difference in the sensitivity of the detector to the antiproton and H^- ion.

The new beam monitors composed of the detector grid successfully worked enabling the estimation of the position and the shape of the beam with a error of a few millimeters. The main cause of the error is the saturation of the signal due to the high gain of the circuit. The optimized gain will improve the accuracy of the estimation. Also a denser grid will contribute to less error in the gaussian fitting for the profile estimation. The data from the calibration will enable the estimation of the intensity of the beam, not only the beam position and the shape.

4 Simulations of the degrader foil

The antiproton beams supplied from ELENA have 100 keV energy, and are transmitted to in front of the trap without losing the energy. Deceleration of antiprotons to the energy of a few keV is required to capture them by high-voltage electrodes placed inside the trap. Foils made of BoPET (Biaxially oriented polyethylene terephthalate), degrader foils, have been utilized for the deceleration of the particles in BASE. The detail of the simulations for the deceleration by degrader foils using FLUKA, a generic Monte Carlo simulator, is described in this section.

4.1 Deceleration of an antiproton beam using a degrader foil

A charged particle moving in a material undergoes deceleration due to elastic and inelastic scattering with electrons and nucleus of the material. Energy lost within unit length $\frac{dE}{dx}$ is called stopping power and is denoted as $S(E)$, where E is the energy of the projected particle. There are mainly two kinds of contributions to the stopping power [44]. One is the inelastic scattering of the projectile with electrons of the target material, which causes energy loss of the projectile. The other is the elastic scattering with the nucleus of target atoms, which leads to diversion of the projectile and less energy loss compared to the former factor. The stopping power can be decomposed as $S(E) = S_e(E) + S_n(E)$.

Although the stopping power for protons in various matters are measured and known, that for antiprotons are less known because of fewer measurements data and the difference in the stopping power between positively and negatively charged particles, which is known as Barkas effect [**?**]. According to the Bethe's theory, it is derived that the stopping power of ion in a matter is proportional to the square of the charge of the projectile Z_1^2[**?**]. However, a correction term proportional to Z_1^3 was added there to describe the difference of the stopping power of alpha particles from the theory. The Barkas effect causes a significant difference in the stopping powers for protons and antiprotons. There is a difference of a factor of 2 between proton and antiproton in the energy range below a few MeV. The difference comes from the polarisation of the material around the particle. The proton attracts electrons and experiences a slightly higher effective electron density, whereas it is the opposite for antiprotons. Thus the stopping power curve for antiprotons is needed to simulate the deceleration of them using degrader foils.

4.2 The principle of a Monte Carlo simulation.

FLUKA, which was used for the simulations for deceleration of antiprotons using degrader foils, is a generic Monte Carlo simulator [45, **?**, **?**]. A Monte Carlo simulation is a method to numerically simulate physical phenomena using random numbers [46].

To configure the Monte Carlo radiation transport simulation, the cross-section of each interaction is needed. In the case of the ion transport in a matter, the cross-sections of the elastic scattering $\sigma_{\mathrm{el}}(E)$ and the inelastic scattering $\sigma_{\mathrm{in}}(E)$ are required. Then mean free path λ, which is the average path length that the projected particle can travel without any interaction, can be determined as below [47].

$$\lambda = \frac{1}{N(\sigma_{\mathrm{el}} + \sigma_{\mathrm{in}})} \tag{4.1}$$

where N is the number density of the atoms of the target material.

As the first step of the ion transport, a primary ion particle is projected from the given initial position with the initial energy. When the particle reaches the surface of the target material, the sampling of the path length takes place. Assuming that the scattering during the travel of the particle follows the Poisson distribution, the probability distribution function of interaction at the path length s, $p(s)$ is expressed as

$$p(s)ds = \frac{1}{\lambda}\exp(-\frac{s}{\lambda})\, ds. \tag{4.2}$$

To determine the path length in this step, the integrated p.d.f is utilized.

$$P(s) = \int_0^s p(s')ds' \tag{4.3}$$

$$= \frac{1}{\lambda}\int_0^s \exp(-\frac{s'}{\lambda})\, ds' \tag{4.4}$$

$$= 1 - \exp(-\frac{s}{\lambda}) \tag{4.5}$$

Then, a random number generator produces μ that uniformly distributes in the interval $[0, 1)$, and $P(s)$ is put as equal to μ.

$$\mu = P(s) = 1 - \exp(-\frac{s}{\lambda}) \tag{4.6}$$

s that satisfies the equation above is taken as the path length of the particle in this step.

The step after determining the step length is to determine the type of interactions. The probability of the inelastic scattering is given as

$$p_{\text{in}} = \frac{\sigma_{\text{in}}}{\sigma_{\text{in}} + \sigma_{\text{el}}} \tag{4.7}$$

An interval $[0, 1)$ can be separated into $[0, p_{\text{in}})$ and $[p_{\text{in}}, 1)$ using p_{in} above. The second random number $\mu_2 \in [0, 1)$ is generated and the program checks which intervals μ_2 is in. The interaction is identified according to which interval contains μ_2.

As the next step, the scattered angle and energy loss due to the interaction are sampled. In the case of an inelastic scattering, the cross-section of the scattering of the ion with energy E with a energy loss W is

$$\sigma_{\text{in}}(E, W) = \frac{d\sigma_{\text{in}}(E)}{dW} \tag{4.8}$$

Then the integrated probability distribution function is derived as

$$P(E, W) = \frac{1}{\sigma_{\text{in}}(E)} \int_0^W dw \frac{d\sigma_{\text{in}}(E)}{dw} \tag{4.9}$$

$$\tag{4.10}$$

As well as the path length sampling described above, a new random number $\mu_3 \in [0, 1)$ is generated and the loss energy W which satisfies

$$\mu_3 = P(E, W) \tag{4.11}$$

is sampled.

Similarly, the cross-section and cumulative probability distribution function of the scattering with scattering angle Ω can be defined as

$$\sigma_{\text{in}}(E, W, \Omega) = \frac{d\sigma_{\text{in}}(E, W)}{d\Omega} \tag{4.12}$$

and

$$P(E, W, \Omega) = \frac{1}{\sigma_{\text{in}}(E, W)} \int_0^\Omega d\Omega' \sigma_{\text{in}}(E, W, \Omega') \tag{4.13}$$

The scattering angle Ω can be sampled by generating a random number μ_4 and putting $\mu_4 = P(E, W, \Omega)$. If the lost energy W is large enough to ionize an electron of the target atom, the program generate a secondary electron for the next step.

Also in the case of the elastic scattering, the scattering angle can be sampled by the same way as the inelastic scattering.

The processes above are repeated until all of primary and secondary particles lose their energy and get caught in the matter, or get out of the geometry.

To get lower statistical errors, the whole processes above is repeated usually 1,000 times or more.

4.3 The settings of the simulation in FLUKA

The simulations in FLUKA were configured using FLAIR3 [48], the graphical interface of FLUKA. Here the detailed configuration of the simulation is described.

Beam configuration

The profile of the input beam is configured in the first field. The antiproton was selected as the particle and the beam energy was set to 100 keV. Although the spread of the beam in the physical and momentum space can be configured, both of them were set to zero. The beam position was set to the point (0,0,-5). These settings mean that in each attempt one antiproton is projected with the kinetic energy of 100 keV from the point.

Electromagnetic field

Since the degrader foil is located inside the trap chamber, which is placed in the superconducting magnet, there is a magnetic field of 1 T when the catching of antiprotons is attempted. FLUKA is capable of applying an electromagnetic field and 1 T field was configured to be applied over the entire geometry. However, since the cyclotron frequency of antiproton under 1 T field is about 3×10^{10} Hz, and 100 keV antiprotons penetrate the degrader foil with $2\,\mu$m thickness in 5×10^{-13} s, the influence of the magnetic field on the trajectory of the antiprotons inside the foil is expected to be limited.

Geometry

In the geometry configuration, several domains are configured to represent some kinds of foils we have as options. The descriptions for the foils are below:

- Foil A (1760 nm): A Mylar foil with 1700 nm that is coated with 30 nm aluminum layer on both sides.
- Foil B (1800 nm): A stack of two Mylar foils with 900 nm thickness. This foil is used in the BASE main experiment.
- Foil C (1850 nm): A stack of two foils. One is 900 nm Mylar and the other is 900 nm Mylar with 25 nm Al coat on both sides.
- Foil D (1900 nm): A stack of foils same as foil C but with 50 nm Al.
- Foil E (1950 nm): A stack of foils same as foil C but with 75 nm Al.
- Foil F (1960 nm): One Mylar foil with 1900 nm thickness with 30 nm Al layer on both sides.

The 1 cm × 1 cm foil was built around the origin in each condition. Regarding the foils C, D, and E, the foils were placed facing the Al coated side to the initial point of the beam. A domain shaped as sphere with 100 cm diameter surrounding the whole geometry of the foil was placed, and two additional domains with the same cross section as the foil and 1 cm thickness were defined next to the upstream and downstream sides of the foil, respectively, to define the detectors to acquire the profile of the penetrating beam.

Material

Materials, aluminum and Mylar were assigned to each domain configured above. The domain, which is a sphere with 100 cm diameter surrounding the foil, was assigned as vacuum. The stopping power table is defined for each material in FLUKA, however the stopping power of Mylar is too high compared to the previous simulations and measurements and most of antiprotons did not penetrate the foil with this stopping power while the previous studies show that antiprotons penetrate with 5 keV average energy. The stopping power was compensated by changing its density from $1.3\,\mathrm{g/cm^3}$ to $0.8\,\mathrm{g/cm^3}$ to match the former study.

Detector

For the detector to acquire the profile of the penetrating particles, the USRBDX command, which acquires the energies and angles of particles going through a boundary between two defined domains, was used. The boundary of the detector was defined between the last layer of the foil on the downstream side and the adjacent vacuum domain of the layer.

Under these configurations, it was set that FLUKA runs simulations of 1 primary particle 100,000 times, and the set of runs is repeated 10 times. The 10 sets of runs were merged after the completion of the simulation to determine the means and statistical errors of the outcomes.

4.4 Results

Fig. 4.1 shows the single differential distributions of the particle current as functions of the energy $dI(E)/dE$. The foil B resulted in outgoing particles with 5.34 keV mean energy and $\sigma = 2.37$ keV deviation by gaussian fitting, which is consistent with the former studies. While the foil A produced the almost same energy distribution as that of foil B, the thicker foils, C, D, E and F, resulted in lower mean energy. In the distributions of foil A and F, there were uneven distributions in the range of 2 to 3 keV, and there were higher distributions in low energy regime of under 2 keV, which were not continuous with the distributions of higher energy in all conditions.

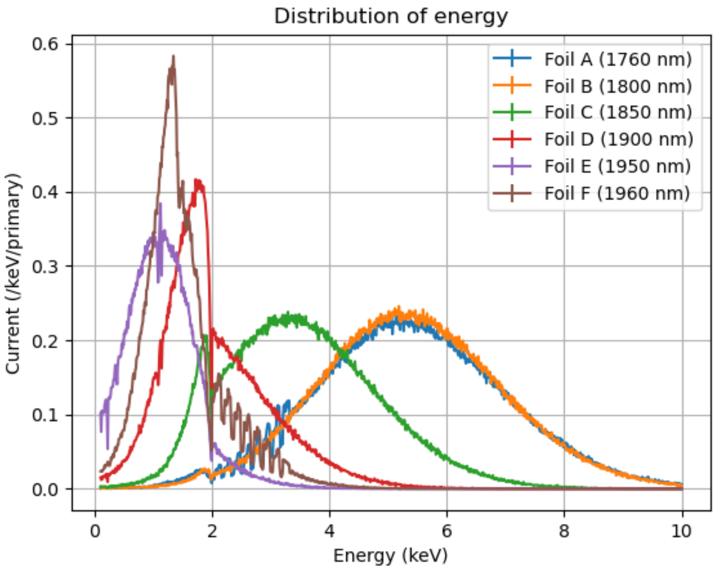

Figure 4.1: Single differential distribution of the particle current as a function of the energy in each foil condition with 10^6 primary particles.

fig. 4.2 shows the double differential distributions as functions of particle energy E and solid angles of the projection Ω. The particles distributed between 0 and 0.2 to 0.4 Sr in every case.

The distributions over the $E - \Omega$ space need to be converted into the distributions over the energy of the axial direction E_{axial} and the cyclotron radius r_{cyc}. If a particle penetrates the foil with a solid angle larger than 0, it travels along a helical trajectory with a cyclotron radius dependent on the energy in the direction perpendicular to the beam axis due to the magnetic field inside the trap chamber. The axial energy E_{axial} determines if the particle can be captured by the electric field produced by the electrodes in the trap. The double differential distributions can be converted to the distributions over energy along the beam axis and the cyclotron radius space by the following processes.

At first, the solid angle Ω needs to be converted to the angle between the beam axis and projected angle. Steradian (Sr), the unit of a solid angle is defined as

$$\Omega\,[\text{Sr}] = \frac{S}{r^2} \tag{4.14}$$

where S is the area of a surface on a sphere surrounded by a cone with the vertex angle Ω and r is the radius of the sphere. When θ is the angle between the axis and the slanted line, the integral on the

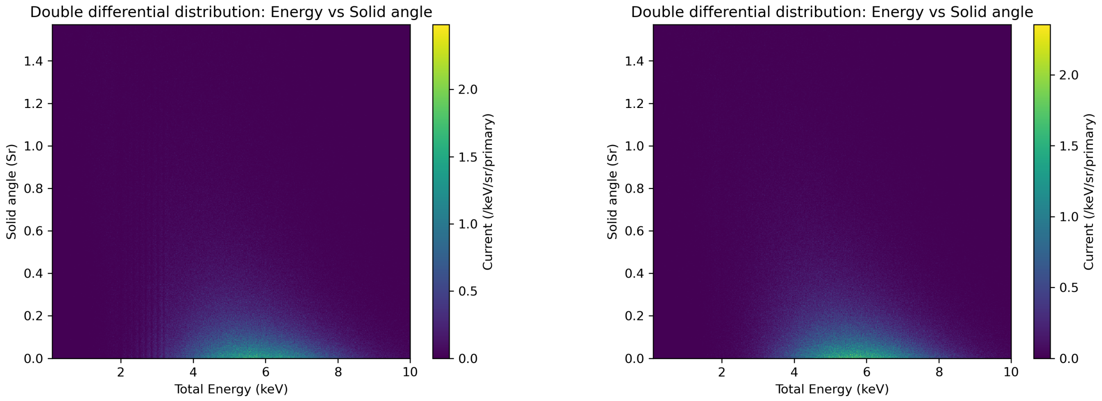

(a) Foil A (1760 nm)

(b) Foil B (1800 nm)

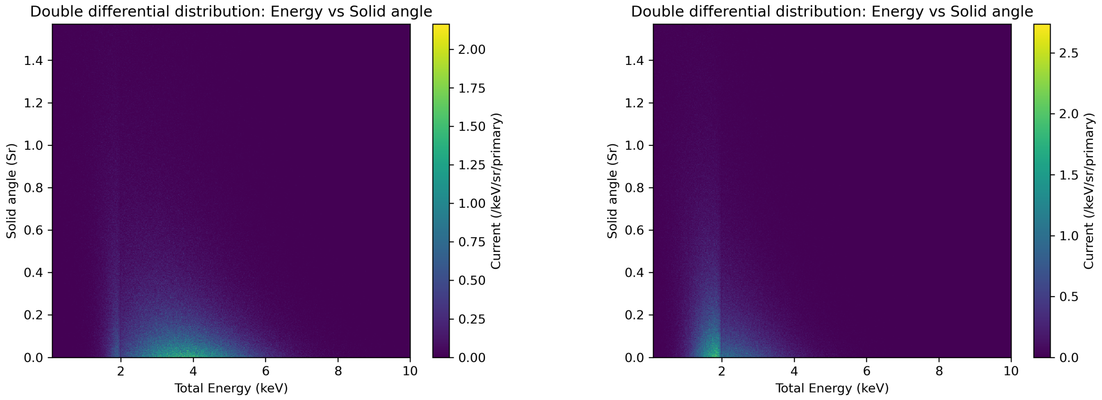

(c) Foil C (1850 nm)

(d) Foil D (1900 nm)

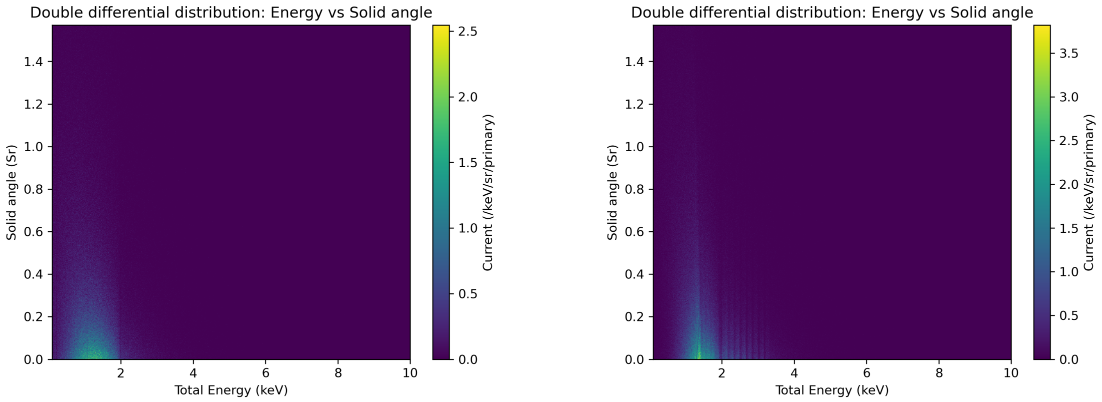

(e) Foil E (1950 nm)

(f) Foil F (1960 nm)

Figure 4.2: The double differential distribution of currents as functions of energy E and solid angle Ω

surface surrounded by the cone follows:

$$S(\theta) = \int_0^\theta 2\pi r^2 \sin\phi d\phi \tag{4.15}$$

$$= 2\pi r^2(1 - \cos\theta) \tag{4.16}$$

Therefore, the angle as a function of the solid angle is

$$\theta(\Omega) = \arccos\left[1 - \frac{\Omega}{2\pi}\right] \tag{4.17}$$

Using $\theta(\Omega)$, the cyclotron energy E_{cyc}, which is the kinetic energy in the direction perpendicular to the beam axis, can be expressed as

$$\begin{aligned} E_{\mathrm{cyc}} &= \frac{1}{2}m_p v_{\mathrm{cyc}}^2 && (4.18)\\ &= \frac{1}{2}m_p v^2 \sin^2\theta(\Omega) && (4.19)\\ &= E(1-\cos^2\theta(\Omega)) && (4.20)\\ &= E\left[1-(1-\frac{\Omega}{2\pi})\right] && (4.21)\\ &= E\left[\frac{\Omega}{\pi} - \left(\frac{\Omega}{2\pi}\right)^2\right] && (4.22) \end{aligned}$$

The cyclotron radius r_{cyc} is derived using the equation of motion including the Lorenz force

$$r_{\mathrm{cyc}} = \frac{2E}{e v_{\mathrm{cyc}} B} \tag{4.23}$$

where e is the elementary charge and B is the magnetic flux density in the trap chamber. Assuming $B = 1\,\mathrm{T}$ as the catching condition and substituting other constants, r_{cyc} can be expressed as a function of E_{cyc} as

$$r_{\mathrm{cyc}}\,[\mathrm{m}] = 1.44 \times 10^{-2} \times \sqrt{E_{\mathrm{cyc}}[\mathrm{keV}]} \tag{4.24}$$

The energy in the direction along the beam axis, E_{axial}, can be obtained by subtracting E_{cyc} from the total energy E.

Fig. 4.3 shows the number of penetrating particles integrated under the axial energies of 0.5, 1.0, 1.5, and 2.0 keV, $dN(r_{\mathrm{cyc}})$ In every case, the distributions had their peaks at higher r_{cyc} rather than around 0. Thicker foils resulted in the higher peaks at lower r_{cyc}.

The counts of particles integrated over both E_{axial} and r_{cyc}, $N(r_{\mathrm{cyc}})$ are also shown in fig. 4.4.

In the cold extraction, injected particles need to go through an electron cloud trapped around the center of the trap, which typically has a spread of 1 mm, to be cooled to further lower energy. Therefore, only particles that have $r_{\mathrm{cyc}} < 1\,\mathrm{mm}$ can be cooled by the electron cloud and captured.

According to the results, in the cases of foil A and B, the difference in the threshold of E_{axial} resulted in a difference in the amount of particles by up to two orders of magnitude. While with the catching voltage from 0.5 to 1.0 keV the order of 10 particles can be electron cooled since a bunch of the beam includes 10^7 antiprotons, with 2.0 keV, 10^3 antiprotons are expected to be cooled. Regarding foils C, D, and E, the increase in the thickness of the foil resulted in the increase of the particles at low r_{cyc} and also a decrease of the difference between the E_{axial} thresholds. In comparison between foils E and F, the result of the foil F showed lower yields of particles in lower E_{axial} threshold conditions.

4.5 Discussion

The results implied some problems in the simulations. The current distribution in energy of the foils A and F showed an uneven distribution in the range of 2 to 3 keV. The foils A and F have an aluminum layer on the downstream side. The scattering process in the Aluminum layer in a low energy range may have caused such an uneven distribution.

Moreover, all of the distributions commonly had higher current in the energy range below 2.0 keV. This is because of the transport limit, which is the lowest energy at which the transport processes can be done, set by FLUKA. The transport limit energy can be set as 2.0 keV at lowest for protons and antiprotons in FLUKA, which means the transport process does not take place for low energy particles below it. Therefore, particles which were scattered to low energy below 2 keV did not completely get

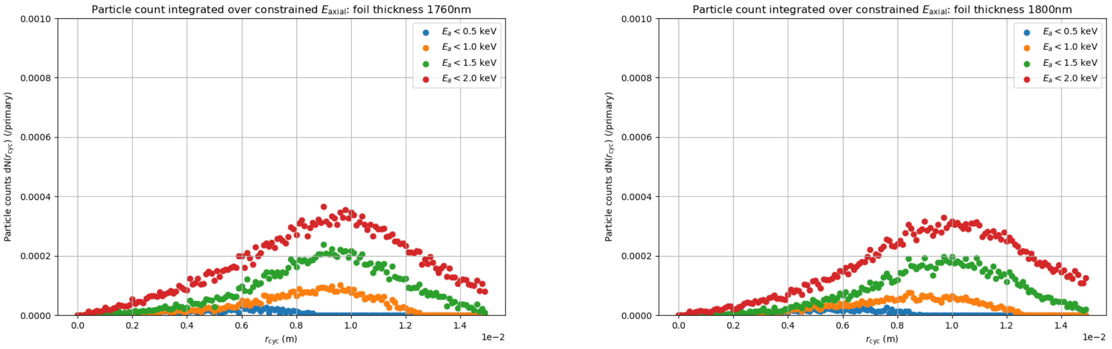

(a) Foil A (narrow y scale)

(b) Foil B (narrow y scale)

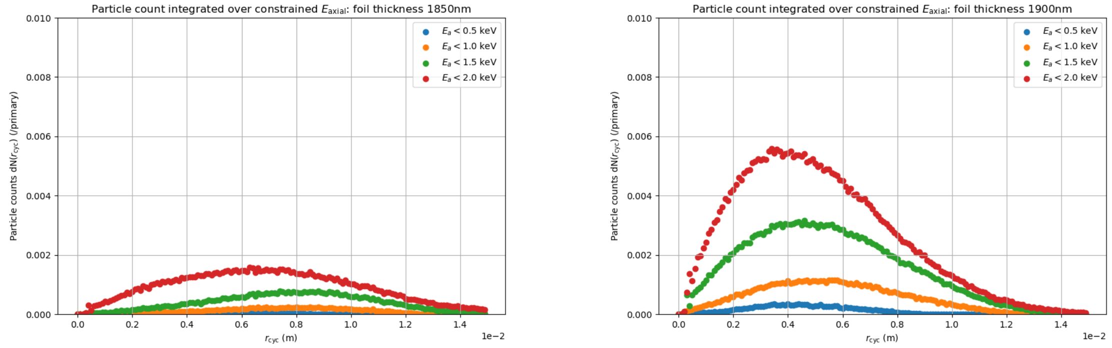

(c) Foil C

(d) Foil D

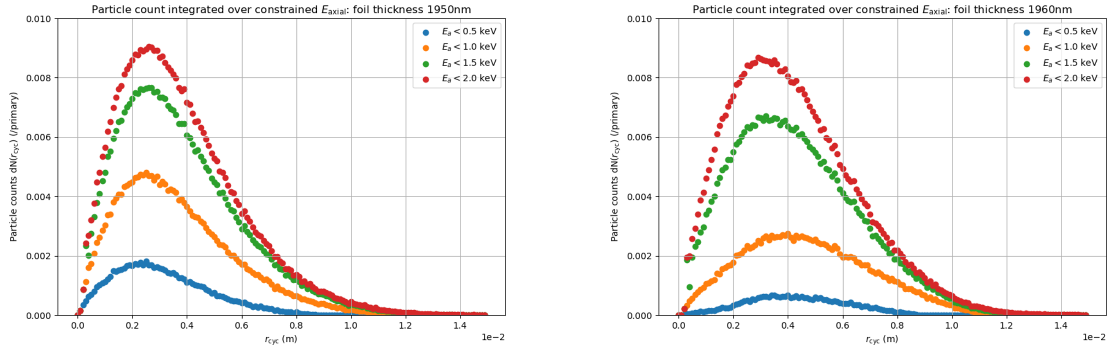

(e) Foil E

(f) Foil F

Figure 4.3: Number of particles per primary integrated under the axial energy of 0.5, 1.0, 1.5, and 2.0 keV as functions of r_{cyc}. Note that the scale of the vertical axis is 10-folds smaller for the plot of foil A and B.

stopped, accumulated within the energy range, and exhibited the higher yield than the higher energy range. Compared to the current at a higher energy over 2 keV, it is expected that the current in the energy range of 0 to 2 keV will be reduced by a factor of 2 to 3 in the case with the transport process in the lower energy range.

To obtain more precise results, another simulator specialized in the transport and scattering of low energy particles [49] will be required.

The integrated number of particles $N(r_{\text{cyc}})$ showed that also thinner foils resulted in enough yields of up to 1,000 at a higher catching voltage, and thicker foils resulted in higher yields with lower catching voltages.

In the simulations implemented here, the input beam was injected into the center of the foil. In

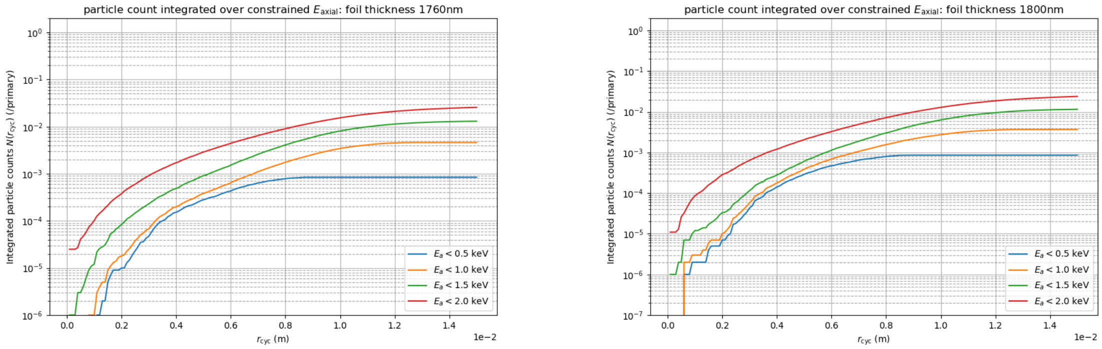

(a) Foil A (b) Foil B

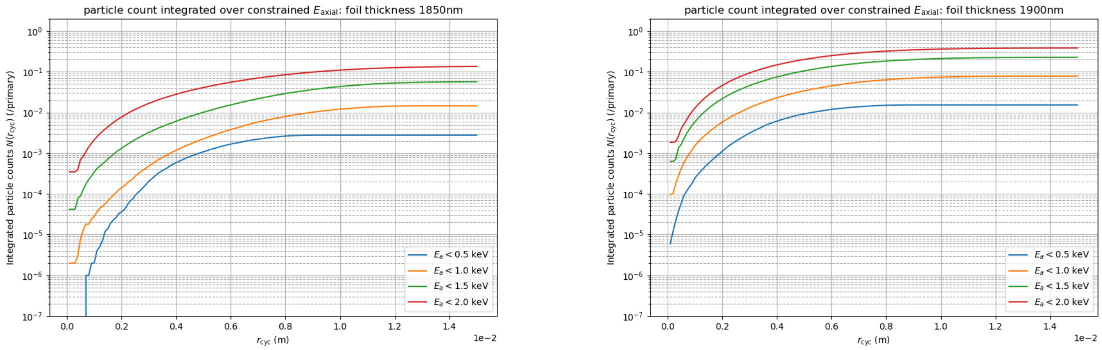

(c) Foil C (d) Foil D

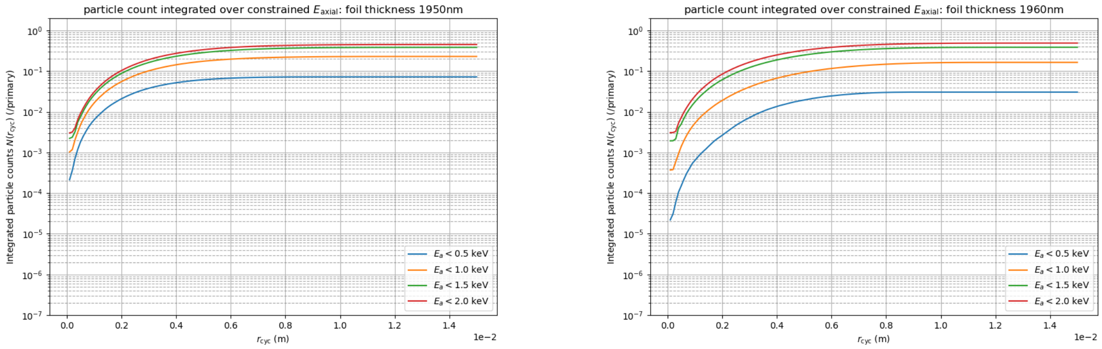

(e) Foil E (f) Foil F

Figure 4.4: The particle count of $E_{\mathrm{axial}} < 0.5, 1.0, 1.5, 2.0\,\mathrm{keV}$ integrated over r_{cyc}

an actual attempt the beam can be unfocused or shifted on the degrader foil depending on the beam steering conditions. The profile of the ejecting beam can be obtained by superimposing the results with an input at a point.

5 Injection of the antiproton beam into the BASE-STEP trap

Since the commissioning of the antiproton beam, the BASE-STEP team had been working on the beam steering to align the beam on the trap. The alignment of the beam was done using the beam monitors described in the section 3 and a scintillator placed in the experimental area. While the beam monitors measure the beam position, the scintillator detects high energy pions and photons produced by the annihilation of the antiprotons with the high time resolution, thus it indicates where the antiprotons hit the wall of the beamline.

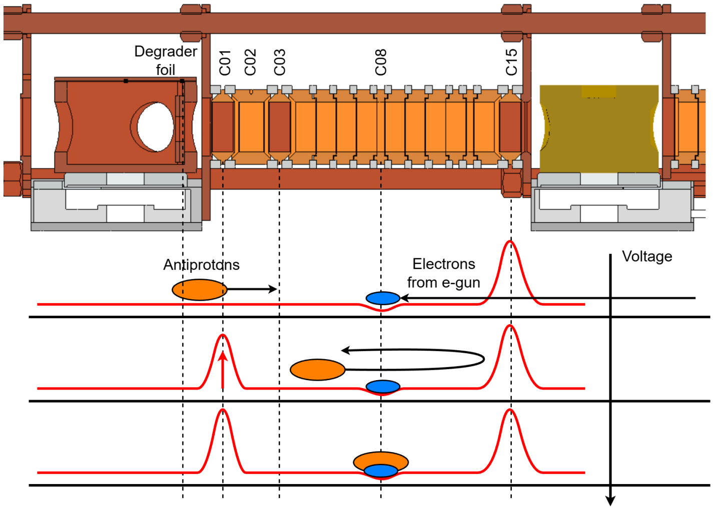

Figure 5.1: The scheme for antiproton catching.

Subsequently, the capture of the antiprotons was attempted. To confirm the successful injection of the antiprotons and to find the optimal catching condition, confinement in a short duration was attempted. The scheme for the particle confinement is shown in fig. 5.1. The electrode C15, which is located at the downstream end of the CT, is constantly biased at a negative high voltage to reflect the particles. The C01 electrode located at the upstream end is ramped from 0 V to the negative high voltage after the bunch passes C01. The high voltage applied at the electrodes at the both ends is held for a certain duration from 100 μs to 100 s. Afterwards, C01 is ramped back to 0 V to release the antiprotons. The annihilation of the released antiprotons is detected by the scintillator, and the intensity of the signal is observed. This procedure is called 'hot extraction'.

To test the cooling into the harmonic well around C08, a procedure called "cold extraction" applies the cooling to a few eV level during the confinement of antiprotons. The cooling of the antiprotons can be done using an electron cloud accumulated at C08 in advance. The cooled antiprotons settle at C08 and are ejected to the outside by manipulating voltages on the electrodes.

In this section, the optimization of the catching condition using the hot extraction, the attempts for cooling of antiprotons, the catching of them and the analysis of the antiproton dip are discussed.

5.1 Hot extraction

Fig. 5.2 shows the connections between the devices used for the catching of antiprotons. The HV pulse system, beam monitor system, and scintillator system, which are synchronized to the injection of the antiproton beam, are triggered by the delay generator, which receives trigger pulses from ELENA at the moment the beam is ejected from the ELENA ring, which is approximately 1 ms before the antiprotons arrive in the experimental zone. The delay generator sends triggers to each system with an independently set delay. The function generator was set to send two pulses of 100 μs width and apart for a certain time (storage time), which are triggered by the pulse from the delay generator. It was removed later and the delay generator directly controlled the HV pulse timing because the function generator made the burst with a random phase shift when changing the oscillation period of the burst signal. The voltage on the C01 is ramped up from a negative high voltage to 0 V by the high voltage switch as the output voltage from the function generator ramps up.

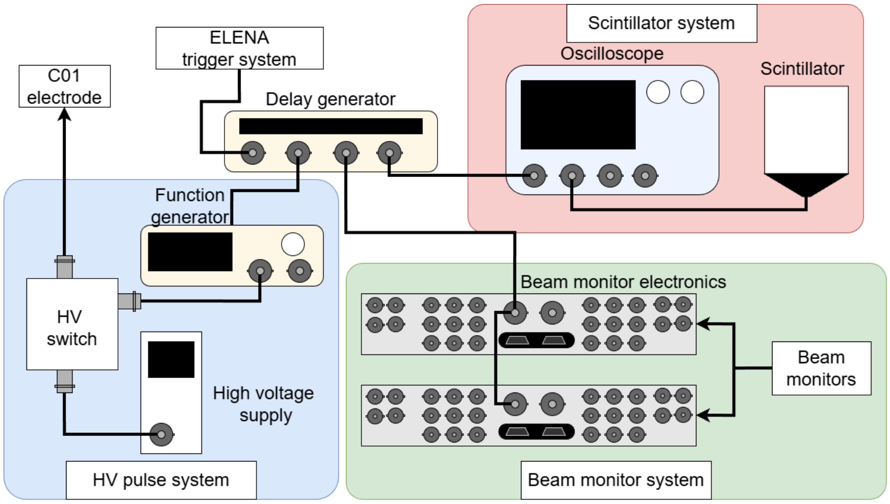

Figure 5.2: The connections between equipments used for the catching.

5.1.1 HV pulse timing scan

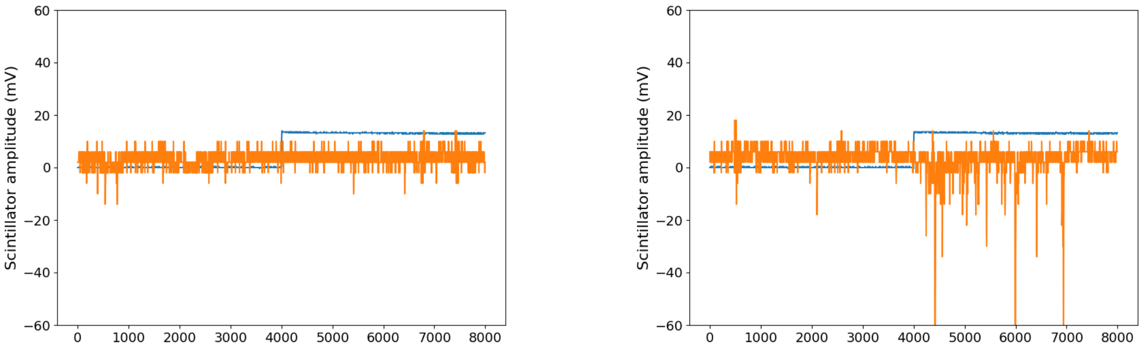

[t]

(a) 899 μs delay

(b) 900.93 μs delay

Figure 5.3: The waveforms of the scintillator (orange) with different HV pulse delay (899 μs and 900.93 μs). The trigger signals for the oscilloscope (blue) are also drawn with the waveforms. There are negative pulses in the waveform of 899 μs delay while there are only a few pulses in the other one.

At first, the delay of the high voltage pulse on C01 was scanned while observing the intensity of the scintillator signal. As shown in fig. 5.3, the difference in the delay by a few μs resulted in a significant difference in the number of the pulses. The amount of the trapped antiprotons during the hot extraction was numerically evaluated by integrating the amplitude of the scintillator signal. Fig. 5.4 shows the integrated amplitudes at several time delays in the range of 896 μs to 902 μs. Large amplitudes could be obtained at delay timings in a range of 2 μs. The delay timing for the HV pulse was set at the timing where the highest signal was obtained for further attempts. Due to the change of the setting of the triggering system and its instability, this scanning was implemented several times in a month.

5.1.2 Beam steering

Subsequently, the beam steering using hot extraction was attempted. The steering in the vertical direction was done using the ZQNA chamber and the deflector chamber placed in the STEP experimental zone. The two-dimensional steering using these devices enables manipulation of both angle and position of the beam, so that the optimal parameters where the beam goes straight into the trap

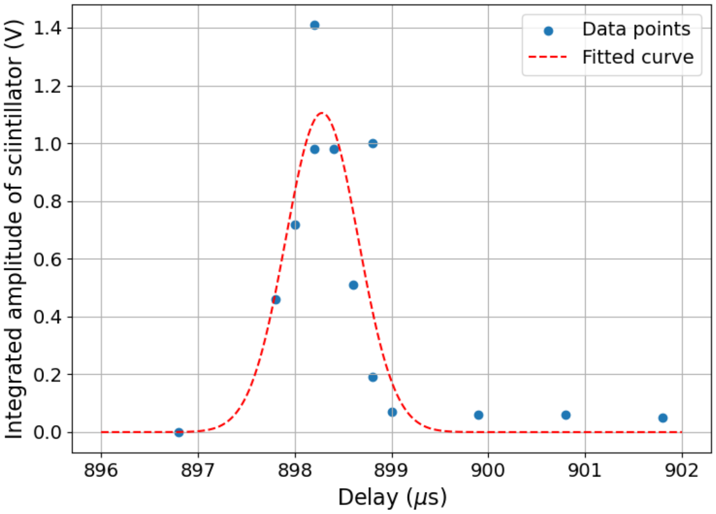

Figure 5.4: The results of the scanning of the delay of the HV pulse with a fitted gaussian line.

chamber can be found. The voltage of the ZQNA chamber was varied from −1850 V to −800 V by 150 V steps, while the voltage of the deflector was varied from 10000 V to 10090 V by 15 V steps.

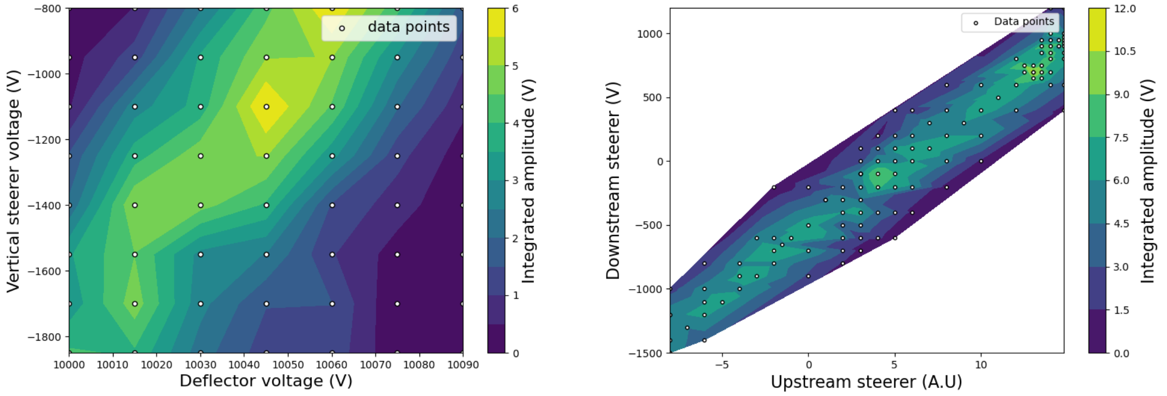

(a) The integrated amplitudes of vertical beam steering.

(b) The integrated amplitudes of horizontal beam steering. The arbitrary unit in the horizontal axis corresponds to approximately 100 V.

Figure 5.5: The contour plots of the vertical and horizontal beam steering. The white dots are the data points.

Fig. 5.5a shows a contour plot of the integrated amplitudes of the scintillator during the steering. High amplitudes are observed at parameters aligned along a line in the parameter space. The parameters $V_{\text{deflector}} = 10045\,\text{V}, V_{\text{ZQNA}} = -1100\,\text{V}$ yielded especially high signal. The line in the parameter space is considered as the optimized parameters for either position or angle to reach inside the trap chamber, and the dependency on the other factor can be seen along the line.

For the horizontal scanning, the voltages applied on the ZQNA chambers, one in the STEP zone and one placed in front of the handover valve, were varied. The parameters where the higher amplitudes were observed were selectively investigated.

The plot of the result is displayed in the Fig. 5.5b. Although the dependency indicating that a higher signal is yielded at the parameters along a line in the parameter space was confirmed, similarly to the vertical scan, but there was less dependency among the parameters along the line. From the simulations by the ELENA staff, we assume that the beam going to the trap is divergent, and it is larger at the degrader foil than the analysis discussed in the section 3. Therefore, we observe signals without a strong scaling over a large parameter range. The main limitation would be the small aperture of the BM1. If it has a larger aperture in the next run, we will be able to focus the beam on the degrader, allowing us to make the signal more sensitive to the steering parameters, and the clear maximum is expected.

5.1.3 DEG voltage scan

The degrader foil stage (DEG) can be biased at a certain voltage up to a few hundreds volts. The dependency of the signal amplitudes on the voltage on the degrader stage was investigated. DEG was biased at the voltages $V = -100$, 0, 100, 150 V and the storage time scan was done at each condition.

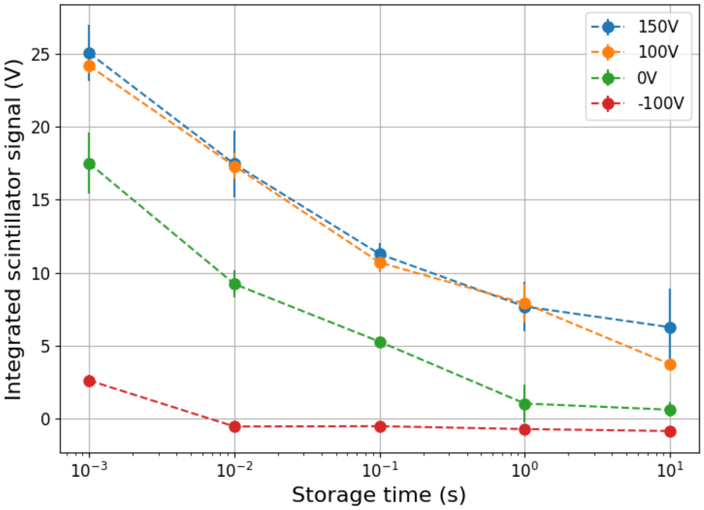

Figure 5.6: The storage time scan at the different DEG voltage settings.

Fig. 5.6 shows the results of the measurements.

Compared to the result at DEG = 0 V, both of DEG = 100, 150 V resulted in higher signals, while the condition −100 V yielded significantly lower signals. The change of the positive degrader voltage did not make differences in the amplitudes.

This effect can be explained that the biased electrode of the positively biased DEG pulls back the antiprotons and the energy distribution shifts to the lower direction, allowing more particles to be caught by the HV potential. A positively biased DEG also pull forward 100 keV antiprotons into the degrader, allowing more antiprotons to penetrate the degrader foil. The negatively biased DEG will cause the opposite effect of above. Since the material of the degrader foil (PET) has high resistivity, a local charge can be produced by the interaction with antiproton, and remain during the hot extraction. Such local charges will also cause the similar effects.

5.1.4 Storage time scan

The dependency of the amount of trapped particles on the storage time was investigated. To this end, hot extractions took place at different storage time settings from 1 ms to 100 s. In a few tests, longer storage times were also investigated and a hot extraction signal was successfully observed for storage times up to about one hour. The storage time scan over a longer range, up to almost 1 hour, was also achieved.

The results are shown in fig. 5.7. Each data was fitted by an exponential decay curve with an offset $f(t) = A\exp(-t/\tau) + b$. While the integrated amplitudes in the short and long storage time range declined linearly with the log x scale and did not fit well with the exponential decay, the peak counts were well fitted with the exponential decay. The fitted parameters are shown in tab. 5.1.

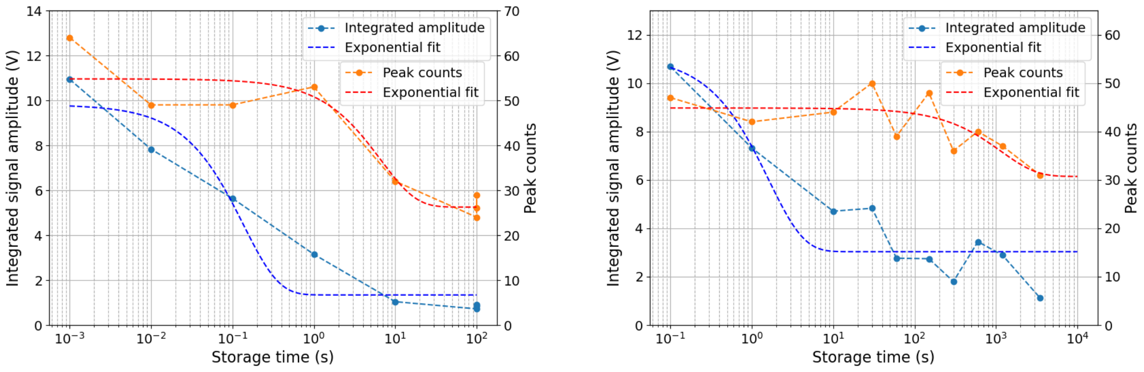

(a) Integrated amplitudes and peak counts at different storage times from 1 ms to 100 s. Exponential curves are fitted to each data points.

(b) Amplitudes and peak counts in longer storage time range (100 ms to 3480 s). The sensitivity of the scintillator is higher than fig. 5.7a due to higher bias voltage.

Figure 5.7: Integrated amplitudes and peak counts at different storage times.The results with shorter time range (1 ms to 100 s) and longer time range (up to about 1 hour) are shown. Exponential decay curves fitted to each data are also displayed.

	Amplitude (short)	Amplitude (long)	Peak count (short)	Peak count (short)
A	8.47	8.10	28.5	14.1
τ	0.137	1.61	6.65	1153.4
b	1.34	3.03	26.3	30.7

Table 5.1: Optimized parameters of exponential decay curves.

The time constant τ differed between the data in the short and long time ranges by 1 or more orders of magnitude. Therefore, the exponential decay model does not explain the data and the loss process cannot be explained by a single process with a single decay constant.

5.1.5 C15 voltage scan

When the antiprotons are reflected by the high voltage potential, they can be destabilized because of the radially pulling electric field formed by the high voltage electrodes. Since we have a lower magnetic field compared to BASE, our limit in HV is lower.

The voltage on the C15 electrode, which is at the downstream end of the CT, was scanned. In this measurement, the negative HV on the C01 electrode was fixed at −500 V, and the C15 voltage was varied from −2000 V to −500 V by 500 V steps. The integrated amplitudes at different storage times (1 ms, 10 ms, 100 ms, 1s, 10s) were measured at the different C15 voltage settings.

The results are shown in fig. 5.8. While the conditions −1000, −1500, −2000 V yielded almost the same dependencies on the storage time, the −500 V condition solely yielded higher amplitudes than other conditions.

5.2 Cold extraction

In a cold extraction attempt, antiprotons are cooled to a few eV level using a technique called sympathetic cooling. Sympathetic cooling uses self-cooling of trapped electrons due to synchrotron radiation. Electrons trapped inside a Penning trap have much higher oscillation frequencies compared to ions due to their light mass. In the case of electrons trapped in the BASE-STEP trap with 1 T magnetic field, the modified cyclotron frequency is about $\nu_+ \simeq 28\,\mathrm{GHz}$. The time constant of the self-cooling τ_e is given by [50]

$$\tau_e = \frac{3\epsilon_0 m_e c^3}{4\pi e^2 \nu_+^2}. \tag{5.1}$$

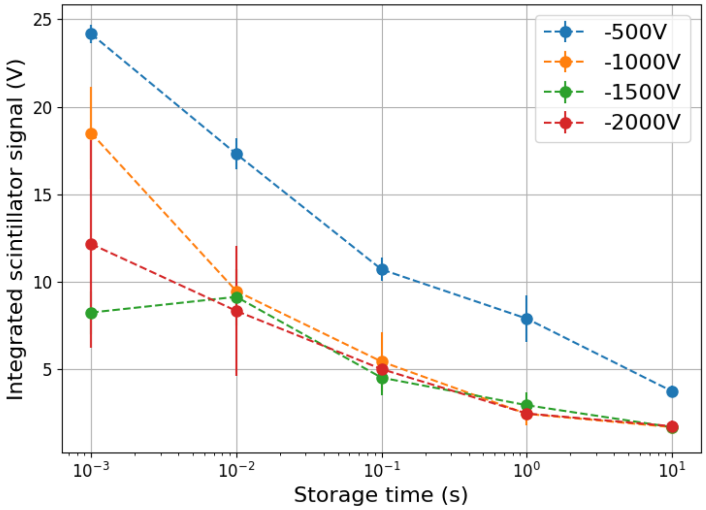

Figure 5.8: The integrated amplitude dependencies on the storage time at different C15 voltage.

Under 1 T field, $\tau_e \simeq 2.6$ s. When the hot antiprotons travel through the cold electrons, the antiprotons interact with electrons by the Coulomb interaction, and the energy of the antiprotons is transferred to the electrons and lost by the self-cooling. The time constant of the sympathetic cooling τ_c is given by [50][30]

$$\tau_c = (4\pi\epsilon_0)^2 \frac{m_{\bar{p}} m_e}{e^4} \frac{1}{n_e \ln\Lambda} \left(\frac{k_B T_{\bar{p}}}{m_{\bar{p}}} + \frac{k_b T_e}{m_e} \right)^{\frac{3}{2}} \tag{5.2}$$

where $\ln\Lambda$ accounts for the cutoff in the integration over impact parameters due to Debye shielding of the Coulomb interaction, n_e is the number density of electrons, and $T_{\bar{p}}$, T_e are the temperatures of the antiprotons and electrons. When the energy of the antiproton is 1 keV and 10^{12} electrons are cooled at $T_e = 10$ K, the time constant τ_c is 1×10^2 s.

5.2.1 Loading of electron cloud

Electrons used for the sympathetic cooling are injected from the electron gun (e-gun), which is placed at the downstream end of the trap chamber. The e-gun has a quite thin needle (field emission point, FEP) to supply electrons by the field emission and an electrode with an aperture in front of FEP to produce a strong electric field to induce the field emission by a positive high voltage (ACC). When electrons are loaded, FEP is biased at a voltage of -30 V to -60 V, and ACC is biased at a positive high voltage up to around 2 kV. After loading a current for a certain time on the FEP biasing line, an electron cloud is trapped around the electrode C08 and HV electrodes C01 and C15 are ramped from 0 V to the high voltage.

A trapped electron cloud causes a shift of the resonance frequency of the detector circuit. The evolution of the electron cloud was investigated at various voltage settings of electrodes by observing the shift of the resonator.

The dependencies of the evolution of the resonator shifts on the trap voltage (C08 voltage), FEP voltage and ACC voltage were investigated. The voltages of the FEP and ACC were set as $\mathrm{FEP} = -40\,\mathrm{V}, \mathrm{ACC} = 1950\,\mathrm{V}$. The voltage on the C03 and C15 electrodes was set to -200 V, -30 V, respectively, so that electrons are reflected at the C03 and electrons that lost their energy by scattering are trapped at the C08. The C15 voltage was slowly ramped up during the loading process until the electrons can no longer enter or leave the CT.

Fig. 5.9 shows the results of the scanning. Generally, the frequency shifts produced when electrons are loaded halve after about 100 s. The scanning of the C08 voltage resulted in that a deeper trap potential leads to more trapped electrons. The voltage of the FEP point was scanned subsequently. The scanning of the ACC voltage showed that it does not affect on the frequency shift.

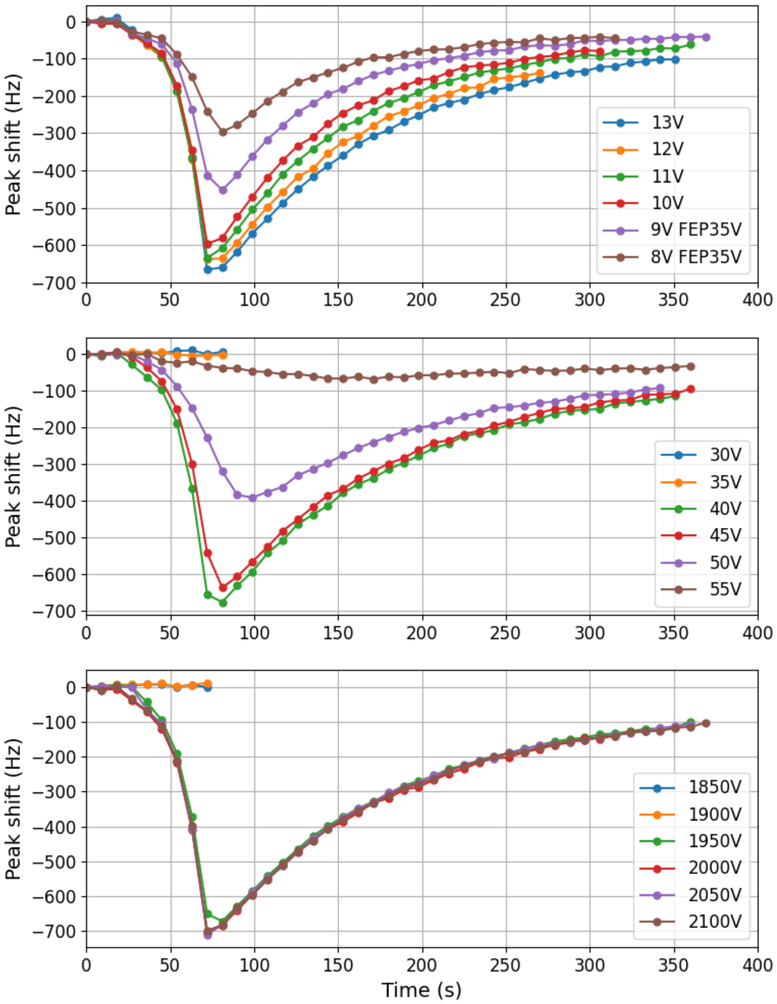

Figure 5.9: The evolution of the resonator shift in the scanning of each parameter. The scanning of C08 voltage, FEP voltage and ACC voltage are shown from the top.

5.2.2 Cold extraction

Subsequently, the extraction of trapped antiprotons was attempted. To this end, electrons were loaded on the trap while the triggering system was turned off, and, after turning the trigger system on, antiprotons were injected and caught by the HV pulse. After waiting the cooling of antiprotons for about 2 minutes, antiprotons were transported from C08 electrode to C02 electrode. Antiprotons trapped at C02 were then ejected from the trap into the degrader foil using electrodes C01 to C03, and the scintillator signal is measured to detect the annihilation.

As a consequence, despite considerable amount of attempts, we could not observe the annihilation signal after this cold extraction scheme.

Fig. 5.10 shows the evolution of the resonance frequency during a cold extraction attempt. When antiprotons were injected into the trap, the resonance frequency jumped to higher by about 250 Hz, which means most of trapped electrons were lost at the injection timing. After about 10 minutes from the injection, electrons were removed by rf radiation. It removed 10 Hz shift of the residual electrons. The result indicates that most of electrons are lost when antiprotons are injected, and thus it is unable to cool the antiprotons.

To see the decay of the antiproton signal while they are trapped with electrons, hot extractions with trapped electrons at different storage times were done. Fig. 5.11 shows integrated scintillator amplitudes at the storage times of 10 ms, 100 ms, 1 s, 10 s, normalized by the signal at 10 ms storage time. There was a significant decrease between the data of 100 ms and 1 s. Compared to the time

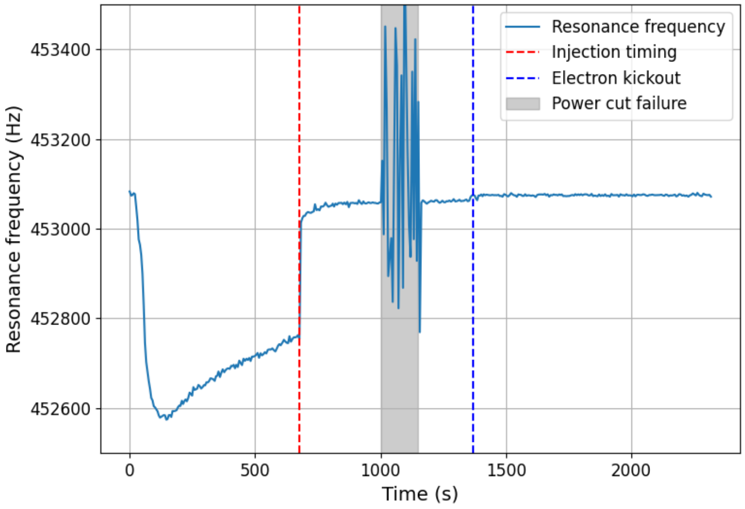

Figure 5.10: The evolution of The resonance frequency shift during a cold extraction. Red and blue dashed lines are respectively the timing of antiproton injection and electron kickout. The large fluctuation starting from $t = 1000\,\mathrm{s}$ is due to malfunction of the detector caused by a power cut.

constant of the sympathetic cooling by electrons estimated to be about 100 s, the time constant of the signal decay is quite short. It indicates that stored antiprotons are lost in the storage time of a few 100 ms for some reason.

These results shown above imply that there is a significant instability in the confinement of antiprotons with electrons and antiprotons are lost in a short time. The detailed mechanism of the antiproton loss is not understood well, and we concluded that it is difficult to capture antiprotons successfully in the current settings.

5.3 Alternative catching scheme for antiprotons

Since the catching of antiprotons using the HV electrodes C01 and C15 and electron cooling is difficult, an alternative catching procedure was attempted. The electrodes from C01 to C03 are mainly used in this procedure. At first, the trap potential is opened by setting the voltages of C01, C02 and C03 to 0 V, −120 V, −200 V, and the potential depicted by the blue line in fig. 5.12 is formed. When the antiprotons are injected, C01 voltage is quickly ramped to −200 V. At that moment, a potential well with the depth of a few 10 V is formed around the C02 electrode, and a fraction of antiprotons that match the energy range of the potential well is captured. Subsequently, the potential well is offset to 0 V level, and afterwards the captured antiprotons are transported to C08.

The hot extraction with scanning of the HV pulse delay and storage time took place before the catching trials.

Fig. 5.13 shows the results of the scanning measurements. High amplitudes could be obtained at delay timings in a range of several 100 ms, which is narrower by a factor of 7 compared to the case of the catching using C01 and C15. The result of the storage time scanning indicated no significant decay of the signal in the range of 1 ms to 10 s.

The delay timing was set to $998.475\,\mu\mathrm{s}$ based on the scanning measurements. After the transportation from C02 to C08, a resonator shift even though no electrons were loaded from the e-gun, which indicates the existence of an antiproton cloud Subsequently, the cleaning of the contaminant particles of the trapped particle cloud was applied. The main components of such contaminant particles are electrons and H^- ions. Electrons were removed by applying a rf-drive at 11 MHz, −10 dBm which excites the axial mode of the electrons while ramping the trap voltage down to 1.0 V. The excited electrons were expelled from the antiproton cloud and collected by adjacent potentials to eject them from the edge afterwards. After the particles including antiprotons and H^- ions were tuned on the resonance of the axial detector, H^- ions were selectively removed by a strong drive at their modi-

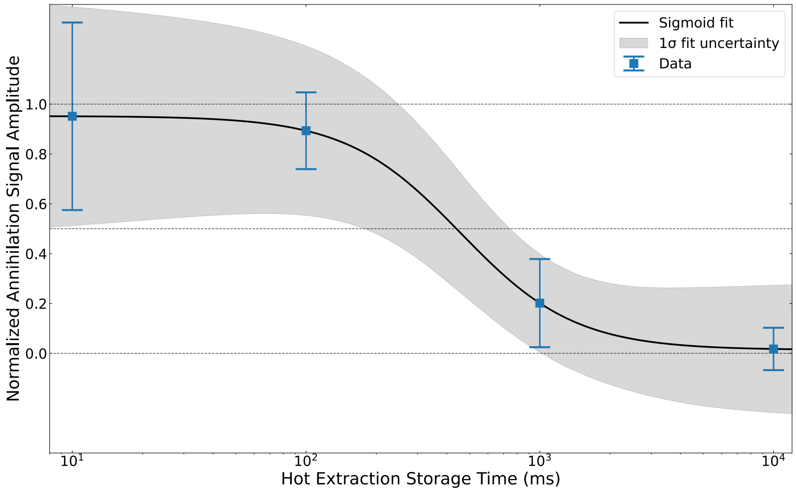

Figure 5.11: Caption

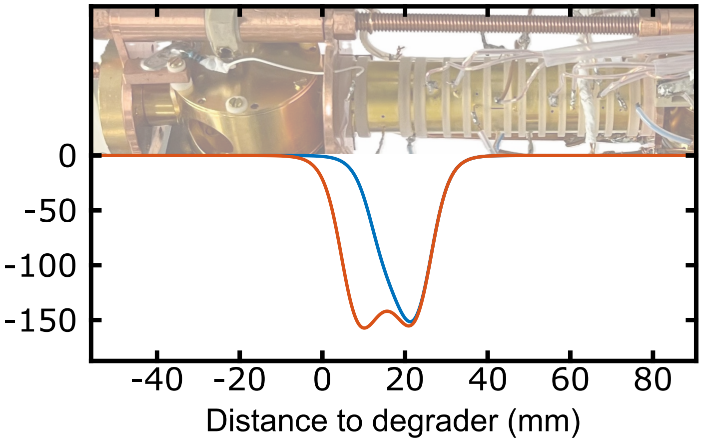

Figure 5.12: The potential during the alternative catching procedure. The blue line is the opened state, and the red line is the closed state. The image of trap electrodes is together placed on the graph.

fied cyclotron mode. After the multiple implementations of these cleaning procedures, the dip was stabilized with a 41.2 Hz dip width, which corresponds to 13 antiprotons.

The electron cleaning was occasionally repeated because electrons can be produced by beta decay on the trap surface and the degrader induced by the beam.

After the storage of antiprotons under 1 T field for about 24 hours without particle losses, the magnetic field was ramped to 136 mT to test the trap operation under the transport mode. The low magnetic field caused the increase of the dip width as shown in fig. 5.15 b, because of the Q-value shift of the axial detector[51]. The trap was operated by the control system of the on-board controller PC, and all core equipments were connected to the uninterrupted power supplies on the transportable frame. Subsequently, the cryostat was disconnected from the cryocooler and the superconducting magnet was maintained by liquid helium boiling off during the test [34]. The transport test was interrupted because of ice formed around the heat exchanger in the cryostat. After the interruption of the transport test, the antiproton cloud was lost due to an operational failure of the power supply. The antiprotons were stored for 31.7 hours in total.

The second antiproton catching was attempted after the loss of the first antiproton cloud. The second antiproton cloud was captured, and a dip with 67.2 Hz width corresponding to 26 antiprotons was observed after the cleaning procedures for electrons and H^- ions. For this time, SWIFT[9] cleaning at -15 dBm was additionally applied to excite oscillation mode of other contaminants in a

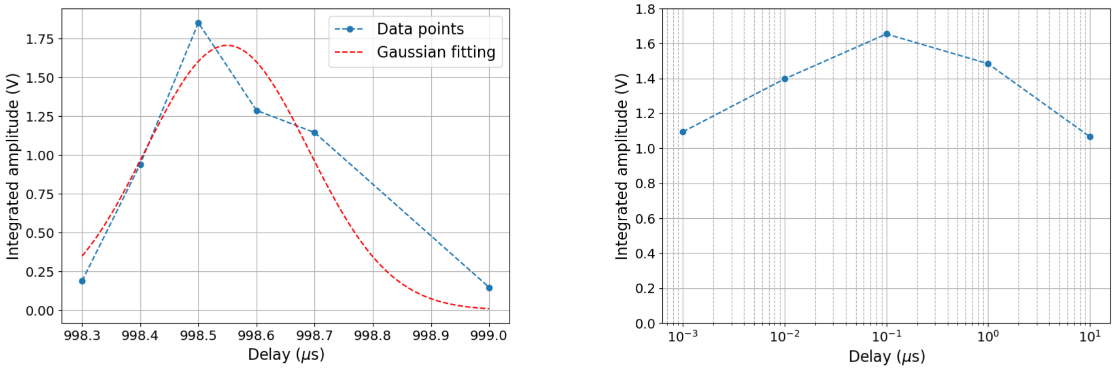

(a) Scanning of the delay timing. A fitted gaussian curve is drawn with data points.

(b) Scanning of the storage time.

Figure 5.13: The results of hot extraction with the new capturing scheme, with scanning of the delay timing and storage time. C2 voltage was 0 V during these measurements.

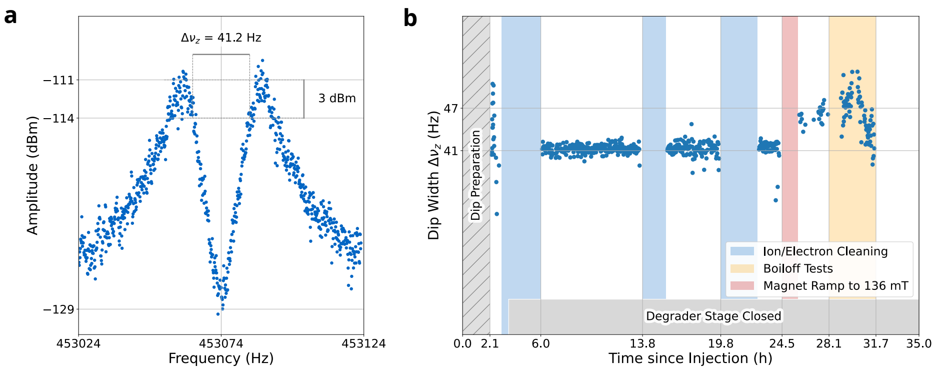

Figure 5.14: a. The FFT spectrum of the axial detector of CT. b. The dip width of the antiproton cloud as a function of time. Colored strips mean the timings of operations of the trap.

broad range of 20 kHz to 400 kHz. After the transport test took place as the first antiproton cloud, the trap was operated at the long-term storage mode, where the sideband cooling of the magnetron mode is periodically applied while recording the dip, with the occasional electron cleaning procedures. The antiproton cloud was stored under this mode for 22.7 hours until it was lost during an electron cleaning process, and the storage of 41.1 hours without loss was achieved.

The lifetime of the antiprotons trapped in the CT can be estimated using the achieved storage time. The lossless storage of the first and second antiproton cloud, 13 particles for 31.7 h and 26 antiprotons for 41.1 h, is equivalent to the storage of a single antiproton for the integrated time $T_{\text{int}} = \int N(t)dt = 1480\,\text{h}$. An antiproton loss happens due to the annihilation with residual gas molecules. Since the antiproton loss is a rare event, decay of an antiproton cloud follows the Poisson distribution $P(\lambda, k)$

$$P(\lambda, k) = \frac{\lambda^k e^{-\lambda}}{k!}, \quad \lambda = \frac{T_{\text{int}}}{\tau}. \tag{5.3}$$

where k is the number of annihilation events, and τ is the estimated lifetime of a single trapped antiproton. The lifetime τ can be estimated at a certain confidence level CL as

$$\tau = -\frac{T_{\text{int}}}{\ln(1 - CL)}. \tag{5.4}$$

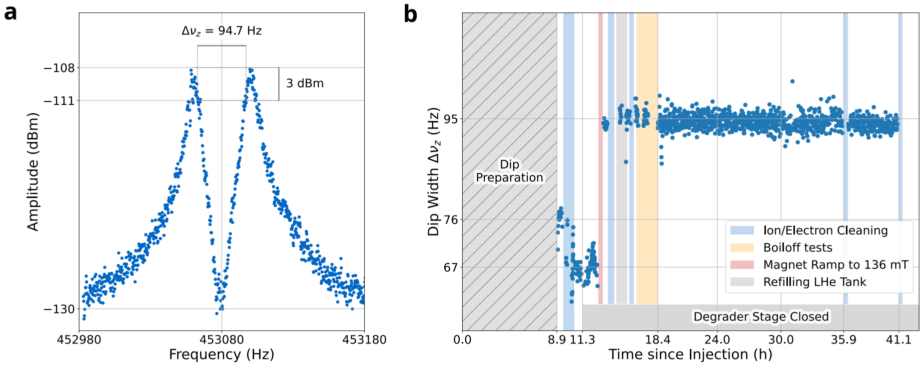

Figure 5.15: a. The FFT spectrum of the axial detector of CT with the dip of the second antiproton cloud. b. The dip width of the second antiproton cloud as a function of time. Colored strips mean the timings of operations of the trap.

The estimated lifetime of an antiproton trapped in the STEP apparatus is

$$\tau = \begin{cases} 1.30 \times 10^{3}\,\mathrm{h} & (CL = 68\,\%) \\ 4.94 \times 10^{2}\,\mathrm{h} & (CL = 95\%). \end{cases} \tag{5.5}$$

Also the vacuum inside the trap chamber can be estimated using the estimated lifetime of antiprotons. Following the approach discussed in [52], the partial pressures of hydrogen atoms, helium atoms, and hydrogen molecules at the temperature $T = 4.2\,\mathrm{K}$ are estimated as

$$P_{\mathrm{H}} = \begin{cases} 4.61 \times 10^{-16}\,\mathrm{mbar} & (CL = 68\,\%) \\ 1.21 \times 10^{-15}\,\mathrm{mbar} & (CL = 95\,\%) \end{cases} \tag{5.6}$$

$$P_{\mathrm{He}} = \begin{cases} 1.05 \times 10^{-15}\,\mathrm{mbar} & (CL = 68\,\%) \\ 2.76 \times 10^{-15}\,\mathrm{mbar} & (CL = 95\,\%) \end{cases} \tag{5.7}$$

$$P_{\mathrm{H_2}} = \begin{cases} 4.66 \times 10^{-16}\,\mathrm{mbar} & (CL = 68\,\%) \\ 1.27 \times 10^{-15}\,\mathrm{mbar} & (CL = 95\,\%) \end{cases} \tag{5.8}$$

6 Conclusion

Regarding the development of the beam monitor, the results indicated the successful functioning of the beam monitors and capability of the estimation of the beam position with an error of a few mm. Although this precision may not be sufficient to inject the antiproton beam into the narrow entry of the trap chamber, it is already enough to adjust the beam into the entry of the DPS. Since the emission rate of the secondary electrons by the collision of an antiproton with the detector surface was larger than the assumption by a factor of 2 to 3, the total output easily saturated. It can be solved by decreasing the gain of the signal amplifier circuit. With proper parameters, also it will be possible to obtain a linear response to the input in the entire range of the output. Avoiding the saturation will improve the shift of the beam position. Increasing the number of the wires composing the grid will be useful to adjust the beam into the trap chamber.

Regarding the degrader foil simulation, the distributions of the antiproton current as functions of the axial energy and the transverse energy could be obtained for several options of degrader foils. Translating the results, the distributions as functions of the axial energy and the cyclotron radius, which is useful to evaluate the survival rate of antiprotons from an injection, were also obtained. However, FLUKA was unable to calculate the transportation of antiprotons with the energy below 2 keV, therefore the results for the thicker foils were unreliable. More precise results that can be obtained by a simulation program specialized for the low energy transportation are required to understand the energy distribution of the decelerated antiprotons. Once the energy distribution of the decelerated antiprotons is obtained, the electrodynamical simulations of the trajectories of the particles inside the trap potential can be conducted. Such simulations will further help to optimize the conditions for the catching such as the timing of the high voltage pulse and the potential formed by electrodes.

Through the attempts of the hot extraction, we got a number of useful scanning data to efficiently optimize the catching. The instability of confinement of antiprotons that was seen during the cold extraction with normal configuration should be understood to implement more efficient catching in the future. The more detailed scanning data of the cold extraction will be essential to understand the mechanism of the antiproton loss, especially the detailed scanning of the storage time. Also the electrodynamical simulation of the particles inside the trap may help to understand this problem.

Even though there are still problems to deal with, the essential milestone, trapping antiprotons in a transportable trap for the first time, was achieved. The demonstration of the antiproton transport will be attempted as the next step by the end of the beam time in the summer of 2026.

A

References

[1] Don Colladay and V. Alan Kostelecký. CPT violation and the standard model. *Physical Review D*, 55(11):6760–6774, June 1997.

[2] Ralf Lehnert. CPT Symmetry and Its Violation. *Symmetry*, 8(11):114, November 2016. Number: 11.

[3] M. Aguilar, L. Ali Cavasonza, B. Alpat, G. Ambrosi, L. Arruda, N. Attig, S. Aupetit, P. Azzarello, A. Bachlechner, F. Barao, A. Barrau, L. Barrin, A. Bartoloni, L. Basara, S. Başeğmez-du Pree, M. Battarbee, R. Battiston, J. Bazo, U. Becker, M. Behlmann, B. Beischer, J. Berdugo, B. Bertucci, V. Bindi, G. Boella, W. De Boer, K. Bollweg, V. Bonnivard, B. Borgia, M.J. Boschini, M. Bourquin, E.F. Bueno, J. Burger, F. Cadoux, X.D. Cai, M. Capell, S. Caroff, J. Casaus, G. Castellini, I. Cernuda, F. Cervelli, M.J. Chae, Y.H. Chang, A.I. Chen, G.M. Chen, H.S. Chen, L. Cheng, H.Y. Chou, E. Choumilov, V. Choutko, C.H. Chung, C. Clark, R. Clavero, G. Coignet, C. Consolandi, A. Contin, C. Corti, B. Coste, W. Creus, M. Crispoltoni, Z. Cui, Y.M. Dai, C. Delgado, S. Della Torre, M.B. Demirköz, L. Derome, S. Di Falco, F. Dimiccoli, C. Díaz, P. Von Doetinchem, F. Dong, F. Donnini, M. Duranti, D. D ' Urso, A. Egorov, A. Eline, T. Eronen, J. Feng, E. Fiandrini, E. Finch, P. Fisher, V. Formato, Y. Galaktionov, G. Gallucci, B. García, R.J. García-López, C. Gargiulo, H. Gast, I. Gebauer, M. Gervasi, A. Ghelfi, F. Giovacchini, P. Goglov, D.M. Gómez-Coral, J. Gong, C. Goy, V. Grabski, D. Grandi, M. Graziani, I. Guerri, K.H. Guo, M. Habiby, S. Haino, K.C. Han, Z.H. He, M. Heil, J. Hoffman, T.H. Hsieh, H. Huang, Z.C. Huang, C. Huh, M. Incagli, M. Ionica, W.Y. Jang, H. Jinchi, S.C. Kang, K. Kanishev, G.N. Kim, K.S. Kim, Th. Kirn, C. Konak, O. Kounina, A. Kounine, V. Koutsenko, M.S. Krafczyk, G. La Vacca, E. Laudi, G. Laurenti, I. Lazzizzera, A. Lebedev, H.T. Lee, S.C. Lee, C. Leluc, H.S. Li, J.Q. Li, J.Q. Li, Q. Li, T.X. Li, W. Li, Z.H. Li, Z.Y. Li, S. Lim, C.H. Lin, P. Lipari, T. Lippert, D. Liu, Hu Liu, S.Q. Lu, Y.S. Lu, K. Luebelsmeyer, F. Luo, J.Z. Luo, S.S. Lv, R. Majka, C. Mañá, J. Marín, T. Martin, G. Martínez, N. Masi, D. Maurin, A. Menchaca-Rocha, Q. Meng, D.C. Mo, L. Morescalchi, P. Mott, T. Nelson, J.Q. Ni, N. Nikonov, F. Nozzoli, P. Nunes, A. Oliva, M. Orcinha, F. Palmonari, C. Palomares, M. Paniccia, M. Pauluzzi, S. Pensotti, R. Pereira, N. Picot-Clemente, F. Pilo, C. Pizzolotto, V. Plyaskin, M. Pohl, V. Poireau, A. Putze, L. Quadrani, X.M. Qi, X. Qin, Z.Y. Qu, T. Räihä, P.G. Rancoita, D. Rapin, J.S. Ricol, I. Rodríguez, S. Rosier-Lees, A. Rozhkov, D. Rozza, R. Sagdeev, J. Sandweiss, P. Saouter, S. Schael, S.M. Schmidt, A. Schulz Von Dratzig, G. Schwering, E.S. Seo, B.S. Shan, J.Y. Shi, T. Siedenburg, D. Son, J.W. Song, W.H. Sun, M. Tacconi, X.W. Tang, Z.C. Tang, L. Tao, D. Tescaro, Samuel C.C. Ting, S.M. Ting, N. Tomassetti, J. Torsti, C. Türkoğlu, T. Urban, V. Vagelli, E. Valente, C. Vannini, E. Valtonen, M. Vázquez Acosta, M. Vecchi, M. Velasco, J.P. Vialle, V. Vitale, S. Vitillo, L.Q. Wang, N.H. Wang, Q.L. Wang, X. Wang, X.Q. Wang, Z.X. Wang, C.C. Wei, Z.L. Weng, K. Whitman, J. Wienkenhöver, M. Willenbrock, H. Wu, X. Wu, X. Xia, R.Q. Xiong, W. Xu, Q. Yan, J. Yang, M. Yang, Y. Yang, H. Yi, Y.J. Yu, Z.Q. Yu, S. Zeissler, C. Zhang, J. Zhang, J.H. Zhang, S.D. Zhang, S.W. Zhang, Z. Zhang, Z.M. Zheng, Z.Q. Zhu, H.L. Zhuang, V. Zhukov, A. Zichichi, N. Zimmermann, P. Zuccon, and AMS Collaboration. Antiproton Flux, Antiproton-to-Proton Flux Ratio, and Properties of Elementary Particle Fluxes

in Primary Cosmic Rays Measured with the Alpha Magnetic Spectrometer on the International Space Station. *Physical Review Letters*, 117(9):091103, August 2016.

[4] C. S. Wu, E. Ambler, R. W. Hayward, D. D. Hoppes, and R. P. Hudson. Experimental Test of Parity Conservation in Beta Decay. *Physical Review*, 105(4):1413–1415, February 1957.

[5] T. D. Lee and C. N. Yang. Question of Parity Conservation in Weak Interactions. *Physical Review*, 104(1):254–258, October 1956.

[6] T. D. Lee, Reinhard Oehme, and C. N. Yang. Remarks on Possible Noninvariance under Time Reversal and Charge Conjugation. *Physical Review*, 106(2):340–345, April 1957.

[7] Christian G. Parthey, Arthur Matveev, Janis Alnis, Birgitta Bernhardt, Axel Beyer, Ronald Holzwarth, Aliaksei Maistrou, Randolf Pohl, Katharina Predehl, Thomas Udem, Tobias Wilken, Nikolai Kolachevsky, Michel Abgrall, Daniele Rovera, Christophe Salomon, Philippe Laurent, and Theodor W. Hänsch. Improved Measurement of the Hydrogen 1 S – 2 S Transition Frequency. *Physical Review Letters*, 107(20):203001, November 2011.

[8] M. Ahmadi, B. X. R. Alves, C. J. Baker, W. Bertsche, A. Capra, C. Carruth, C. L. Cesar, M. Charlton, S. Cohen, R. Collister, S. Eriksson, A. Evans, N. Evetts, J. Fajans, T. Friesen, M. C. Fujiwara, D. R. Gill, J. S. Hangst, W. N. Hardy, M. E. Hayden, C. A. Isaac, M. A. Johnson, J. M. Jones, S. A. Jones, S. Jonsell, A. Khramov, P. Knapp, L. Kurchaninov, N. Madsen, D. Maxwell, J. T. K. McKenna, S. Menary, T. Momose, J. J. Munich, K. Olchanski, A. Olin, P. Pusa, C. Ø Rasmussen, F. Robicheaux, R. L. Sacramento, M. Sameed, E. Sarid, D. M. Silveira, G. Stutter, C. So, T. D. Tharp, R. I. Thompson, D. P. van der Werf, and J. S. Wurtele. Characterization of the 1S–2S transition in antihydrogen. *Nature*, 557(7703):71–75, May 2018.

[9] C. Smorra, K. Blaum, L. Bojtar, M. Borchert, K.A. Franke, T. Higuchi, N. Leefer, H. Nagahama, Y. Matsuda, A. Mooser, M. Niemann, C. Ospelkaus, W. Quint, G. Schneider, S. Sellner, T. Tanaka, S. Van Gorp, J. Walz, Y. Yamazaki, and S. Ulmer. BASE – The Baryon Antibaryon Symmetry Experiment. *The European Physical Journal Special Topics*, 224(16):3055–3108, November 2015.

[10] C. Smorra, S. Sellner, M. J. Borchert, J. A. Harrington, T. Higuchi, H. Nagahama, T. Tanaka, A. Mooser, G. Schneider, M. Bohman, K. Blaum, Y. Matsuda, C. Ospelkaus, W. Quint, J. Walz, Y. Yamazaki, and S. Ulmer. A parts-per-billion measurement of the antiproton magnetic moment. *Nature*, 550(7676):371–374, October 2017.

[11] M. J. Borchert, J. A. Devlin, S. R. Erlewein, M. Fleck, J. A. Harrington, T. Higuchi, B. M. Latacz, F. Voelksen, E. J. Wursten, F. Abbass, M. A. Bohman, A. H. Mooser, D. Popper, M. Wiesinger, C. Will, K. Blaum, Y. Matsuda, C. Ospelkaus, W. Quint, J. Walz, Y. Yamazaki, C. Smorra, and S. Ulmer. A 16-parts-per-trillion measurement of the antiproton-to-proton charge–mass ratio. *Nature*, 601(7891):53–57, January 2022.

[12] C. Smorra, F. Abbass, D. Schweitzer, M. Bohman, J. D. Devine, Y. Dutheil, A. Hobl, B. Arndt, B. B. Bauer, J. A. Devlin, S. Erlewein, M. Fleck, J. I. Jäger, B. M. Latacz, P. Micke, M. Schiffelholz, G. Umbrazunas, M. Wiesinger, C. Will, E. Wursten, H. Yildiz, K. Blaum, Y. Matsuda, A. Mooser, C. Ospelkaus, W. Quint, A. Soter, J. Walz, Y. Yamazaki, and S. Ulmer. BASE-STEP: A transportable antiproton reservoir for fundamental interaction studies. *Review of Scientific Instruments*, 94(11):113201, November 2023.

[13] M. Leonhardt, D. Schweitzer, F. Abbass, K. K. Anjum, B. Arndt, S. Erlewein, S. Endoh, P. Geissler, T. Imamura, J. I. Jäger, B. M. Latacz, P. Micke, F. Voelksen, H. Yildiz, K. Blaum, J. A. Devlin, Y. Matsuda, C. Ospelkaus, W. Quint, A. Soter, J. Walz, Y. Yamazaki, S. Ulmer, and C. Smorra. Proton transport from the antimatter factory of CERN. *Nature*, 641(8064):871–875, May 2025.

[14] P. a. M. Dirac. The quantum theory of the electron. *Proceedings of the Royal Society of London Series a-Containing Papers of a Mathematical and Physical Character*, 117(778):610–624, February 1928. Num Pages: 15 Place: London Web of Science ID: WOS:000202787400007.

[15] Anthony Zee. *Quantum Field Theory in a Nutshell: Second Edition.* Princeton University Press, Princeton, UNITED STATES, 2010.

[16] Michael Charlton, Stefan Eriksson, and Graham M. Shore. *Antihydrogen and Fundamental Physics.* SpringerBriefs in Physics. Springer International Publishing, Cham, 2020.

[17] Carl D. Anderson. The Positive Electron. *Physical Review*, 43(6):491–494, March 1933.

[18] Gerhart Luders. On the Equivalence of Invariance under Time Reversal and under Particle-Antiparticle Conjugation for Relativistic Field Theories. *Kong. Dan. Vid. Sel. Mat. Fys. Med.*, 28N5(5):1–17, 1954.

[19] Donald H. Perkins. *Introduction to High Energy Physics.* Cambridge University Press, Cambridge, 4 edition, 2000.

[20] Richard H. Cyburt. Primordial nucleosynthesis for the new cosmology: Determining uncertainties and examining concordance. *Physical Review D*, 70(2):023505, July 2004.

[21] D. Larson, J. Dunkley, G. Hinshaw, E. Komatsu, M. R. Nolta, C. L. Bennett, B. Gold, M. Halpern, R. S. Hill, N. Jarosik, A. Kogut, M. Limon, S. S. Meyer, N. Odegard, L. Page, K. M. Smith, D. N. Spergel, G. S. Tucker, J. L. Weiland, E. Wollack, and E. L. Wright. Seven-Year Wilkinson Microwave Anisotropy Probe (WMAP) Observations: Power Spectra and WMAP-Derived Parameters. *The Astrophysical Journal Supplement Series*, 192(2):16, February 2011. arXiv:1001.4635 [astro-ph].

[22] Laurent Canetti, Marco Drewes, and Mikhail Shaposhnikov. Matter and antimatter in the universe. *New Journal of Physics*, 14(9):095012, September 2012.

[23] J. H. Christenson, J. W. Cronin, V. L. Fitch, and R. Turlay. Evidence for the $2\ensuremath{\pi}$ Decay of the K_{2}^{0} Meson. *Physical Review Letters*, 13(4):138–140, July 1964.

[24] Don Colladay and Alan Kostelecky. Lorentz-Violating Extension of the Standard Model. *Physical Review D*, 58(11):116002, October 1998. arXiv:hep-ph/9809521.

[25] Robert Bluhm, Alan Kostelecky, and Neil Russell. CPT and Lorentz Tests in Penning Traps. *Physical Review D*, 57(7):3932–3943, April 1998. arXiv:hep-ph/9809543.

[26] B. Schwingenheuer, R. A. Briere, A. R. Barker, E. Cheu, L. K. Gibbons, D. A. Harris, G. Makoff, K. S. McFarland, A. Roodman, Y. W. Wah, B. Winstein, R. Winston, E. C. Swallow, G. J. Bock, R. Coleman, M. Crisler, J. Enagonio, R. Ford, Y. B. Hsiung, D. A. Jensen, E. Ramberg, R. Tschirhart, T. Yamanaka, E. M. Collins, G. D. Gollin, P. Gu, P. Haas, W. P. Hogan, S. K. Kim, J. N. Matthews, S. S. Myung, S. Schnetzer, S. V. Somalwar, G. B. Thomson, and Y. Zou. CPT Tests in the Neutral Kaon System. *Physical Review Letters*, 74(22):4376–4379, May 1995.

[27] Robert S. Van Dyck, Paul B. Schwinberg, and Hans G. Dehmelt. New high-precision comparison of electron and positron g factors. *Physical Review Letters*, 59(1):26–29, July 1987.

[28] Nobel Prize in Physics 1989.

[29] DEHMELT H. G. Radiofrequency spectroscopy of stored ions I : Storage. *Advances in Atomic and Molecular Physics*, 3:53–72, 1967.

[30] Manuel Vogel. *Particle Confinement in Penning Traps: An Introduction*, volume 126 of *Springer Series on Atomic, Optical, and Plasma Physics.* Springer International Publishing, Cham, 2024.

[31] D. J. Wineland and H. G. Dehmelt. Principles of the stored ion calorimeter. *Journal of Applied Physics*, 46(2):919–930, February 1975.

[32] J. B. Johnson. Thermal Agitation of Electricity in Conductors. *Nature*, 119(2984):50–51, January 1927.

[33] H. Nyquist. Thermal Agitation of Electric Charge in Conductors. *Physical Review*, 32(1):110–113, July 1928.

[34] Stefan Ulmer, Christian Smorra, Amado Bautista-Salvador, Julia-Aileen Coenders, and Juan Manuel Cornejo. BASE - Annual Report 2024.

[35] B.M. Latacz, M. Fleck, J.I. Jäger, G. Umbrazunas, B.P. Arndt, S.R. Erlewein, E.J. Wursten, J.A. Devlin, P. Micke, F. Abbass, D. Schweitzer, M. Wiesinger, C. Will, H. Yildiz, K. Blaum, Y. Matsuda, A. Mooser, C. Ospelkaus, C. Smorra, A. Soter, W. Quint, J. Walz, Y. Yamazaki, S. Ulmer, and BASE Collaboration. Orders of Magnitude Improved Cyclotron-Mode Cooling for Nondestructive Spin Quantum Transition Spectroscopy with Single Trapped Antiprotons. *Physical Review Letters*, 133(5):053201, August 2024.

[36] S A Baird, D Berlin, J Boillot, Jacques Bosser, M Brouet, J Buttkus, Friedhelm Caspers, V Chohan, Daniel Dekkers, T Eriksson, R Garoby, R Giannini, Oswald Gröbner, J Gruber, J Y Hémery, Heribert Koziol, R MacCaferri, S Maury, C Metzger, K D Metzmacher, D Möhl, H Mulder, M Paoluzzi, F Pedersen, J P Riunaud, C Serre, Daniel Jean Simon, G Tranquille, Jan Willem Nicolaas Tuyn, and B Williams. Design study of the antiproton decelerator, 1996.

[37] Vinod Chohan, C. Alanzeau, M. E. Angoletta, J. Baillie, D. Barna, W. Bartmann, P. Belochitskii, J. Borburgh, H. Breuker, F. Butin, M. Buzio, O. Capatina, C. Carli, E. Carlier, M. Cattin, T. Dobers, P. Chiggiato, L. Ducimetiere, T. Eriksson, S. Fedemann, T. Fowler, R. Froeschl, R. Gebel, N. Gilbert, S. Hancock, J. Harasimowicz, M. Hori, L. V. Jorgensen, R. Kersevan, D. Kuchler, J. M. Lacroix, G. LeGodec, P. Lelong, L. Lopez-Hernandez, S. Maury, J. Molendijk, B. Morand, A. Newborough, D. Nisbet, A. Nosych, W. Oelert, M. Paoluzzi, S. Pasinelli, F. Pedersen, D. Perini, B. Puccio, J. Sanchez-Quesada, D. Schoerling, L. Sermeus, L. Soby, M. Timmins, D. Tommasini, G. Tranquille, G. Vanbavinckhove, A. Vorozhtsov, C. Welsch, and T. Zickler. Extra Low ENergy Antiproton (ELENA) ring and its Transfer Lines: Design Report. July 2014.

[38] John Marriner. Stochastic cooling overview. *Nuclear Instruments and Methods in Physics Research Section A: Accelerators, Spectrometers, Detectors and Associated Equipment*, 532(1):11–18, October 2004.

[39] Joseph Bisognano and S. Chattopadhyay. Stochastic Cooling of Bunched Beams. *Nuclear Science, IEEE Transactions on*, 28:2462–2464, July 1981.

[40] I. N. Meshkov. Electron cooling — the first 30 years and thereafter. *Nuclear Instruments and Methods in Physics Research Section A: Accelerators, Spectrometers, Detectors and Associated Equipment*, 391(1):1–11, May 1997.

[41] G. Gabrielse, X. Fei, L. A. Orozco, R. L. Tjoelker, J. Haas, H. Kalinowsky, T. A. Trainor, and W. Kells. Cooling and slowing of trapped antiprotons below 100 meV. *Physical Review Letters*, 63(13):1360–1363, September 1989.

[42] A. Mooser, S. Ulmer, K. Blaum, K. Franke, H. Kracke, C. Leiteritz, W. Quint, C. C. Rodegheri, C. Smorra, and J. Walz. Direct high-precision measurement of the magnetic moment of the proton. *Nature*, 509(7502):596–599, May 2014.

[43] C. Smorra, A. Mooser, K. Franke, H. Nagahama, G. Schneider, T. Higuchi, S. V. Gorp, K. Blaum, Y. Matsuda, W. Quint, J. Walz, Y. Yamazaki, and S. Ulmer. A reservoir trap for antiprotons. *International Journal of Mass Spectrometry*, 389:10–13, October 2015.

[44] K. Nordlund, M. Hori, and D. Sundholm. Large nuclear scattering effects in antiproton transmission through polymer and metal-coated foils. *Physical Review A*, 106(1):012803, July 2022.

[45] G. Battistoni, F. Cerutti, A. Fassò, A. Ferrari, S. Muraro, J. Ranft, S. Roesler, and P. R. Sala. The FLUKA code: description and benchmarking. *AIP Conference Proceedings*, 896(1):31–49, March 2007.

[46] Joao Seco and Frank Verhaegen, editors. *Monte Carlo Techniques in Radiation Therapy.* CRC Press, Boca Raton, April 2016.

[47] Maurizio Dapor. *Transport of Energetic Electrons in Solids: Computer Simulation with Applications to Materials Analysis and Characterization*, volume 290 of *Springer Tracts in Modern Physics*. Springer International Publishing, Cham, 2023.

[48] André Donadon, Gabrielle Hugo, Christian Theis, and Vasilis Vlachoudis. FLAIR3 – recasting simulation experiences with the Advanced Interface for FLUKA and other Monte Carlo codes. *EPJ Web of Conferences*, 302:11005, 2024.

[49] K. Nordlund. Molecular dynamics simulation of ion ranges in the 1–100 keV energy range. *Computational Materials Science*, 3(4):448–456, March 1995.

[50] Guo-Zhong Li, Shenheng Guan, and Alan G. Marshall. Sympathetic cooling of trapped negative ions by self-cooled electrons in a fourier transform ion cyclotron resonance mass spectrometer. *Journal of the American Society for Mass Spectrometry*, 8(8):793–800, August 1997.

[51] S. Ulmer, H. Kracke, K. Blaum, S. Kreim, A. Mooser, W. Quint, C. C. Rodegheri, and J. Walz. The quality factor of a superconducting rf resonator in a magnetic field. *Review of Scientific Instruments*, 80(12):123302, December 2009.

[52] Xiang Fei. *Trapping low-Energy anti-protons in an ion trap.* PhD Thesis, Harvard U., Phys. Dept., 1990.